A NOVEL MOVING BOUNDARY CONDITION BASED ON CHAPMAN-ENSKOG EXPANSION WITH THE LATTICE BOLTZMANN METHOD

by

Lina Xu

BS, Xi'an Jiaotong University, China, 2006

MS, Xi'an Jiaotong University, China, 2009

Submitted to the Graduate Faculty of

the Swanson School of Engineering in partial fulfillment

of the requirements for the degree of

Ph. D. in Mechanical Engineering

University of Pittsburgh

2014

UNIVERSITY OF PITTSBURGH

SWANSON SCHOOL OF ENGINEERING

This dissertation was presented

by

Lina Xu

It was defended on

September 22, 2014

and approved by

Anne M. Robertson, Ph. D., Professor, Department of Mechanical Engineering

and Materials Science

Minking K. Chyu, Ph. D., Professor and Department Chair, Department of Mechanical

Engineering and Materials Science

Zhi-Hong Mao, Ph. D., Associate Professor, Department of Electrical and Computer

Engineering and Department of Bioengineering

Dissertation Director: Laura A. Schaefer, Ph. D., Professor, Department in Mechanical

Engineering and Materials Science

A NOVEL MOVING BOUNDARY CONDITION BASED ON CHAPMAN-ENSKOG EXPANSION WITH THE LATTICE BOLTZMANN METHOD

Lina Xu, PhD

University of Pittsburgh, 2014

Particulate suspensions are common phenomena in industrial and biological fields. However, the fundamental understanding of the hydrodynamic interactions between the solid and fluid in the particulate suspensions needs to be further improved. The lattice Boltzmann method has been shown to be an effective numerical method to model various fluid flows, and exhibits good performance in dealing with boundary conditions, with straightforward and easy-to-implement methods for complex solid boundaries. However, most of the previous boundary conditions used for the moving complex surface are based on the half way bounce-back boundary condition, where the geometric integrity of the body cannot be maintained. In this dissertation, a new boundary condition based on the Chapman-Enskog expansion is proposed for the moving complex surface, where the precise shape of the body can be preserved during the calculation. Moreover, due to the second order accuracy of the Chapman-Enskog expansion when recovering the Navier-Stokes equation from the Boltzmann-BGK equation, the new boundary condition can maintain the same accuracy for the whole computational domain. Finally, this thesis provides the novel idea to construct a boundary condition without the limitation of being based on the information from the already existing lattice nodes.

TABLE OF CONTENTS

LIST OF TABLES

LIST OF FIGURES

ACKNOWLEDGMENTS

First and foremost, I want to express my deepest appreciation to Dr. Laura A. Schaefer, my PhD advisor, for supporting me, encouraging me, and guiding me throughout my research process and dissertation work. I want to appreciate all her contributions of time, ideas, and patience to help me get great idea to further my research. Without all your support, I could impossible fulfill my dream to obtain a PhD degree. It is hard to find words to describe how much I appreciate all you have done for me as a research supervisor and life mentor. Thank you.

My thanks are extended to the members of my thesis committee, Drs. Anne M. Robertson, Minking Chyu, and Zhi-hong Mao. Thank you for your precious time and valuable advice. I also thank Drs. Robertson, Chyu, and Mao for the amazing and wonderful classes they gave. I am also very thankful to all the faculty and staff members in the Department of Mechanical Engineering, who have made my studies and research here valuable and enjoyable.

My time at Pitt was made enjoyable due to the lab group members and friends that became a part of my life. I am grateful for valuable discussion and pleasant time spent with group members: Leitao Chen, Parthib Rao, Michael Winston, and Tourkov Konstantin. Special thanks go to Michael Winston for all the kind assistance and useful suggestions. My time at Pitt was also enriched by my dear friends: Xiaojun Liang, Xiahan Sang, Zhongfan Zhang, Yihong Kang, Hua Li, Shuang Wang, Qiuyan Li, Can He, and Tieyuan Zhang.

Lastly, I would like to thank my family for all their love and encouragement. I am deeply indebted to my father: Zewei Xu, my mother Pingying Tian, and my brother Keming Xu for their never ending love, encouragement and support through my long journey of study and research. There are no words that can express my gratitude and appreciation for all you've done and been for me. I am also thankful for all the love and encouragements from my husband's parents and my brother-in-law.

Finally, I would like to thank my husband Rongxin Zhang for his endless love and absolute faith in me. He has faith in me and encourage me when I had hard times for research and life and also gives me all the support to help me overcome the difficulties. These past several years have not been an easy ride, both academically and personally. I truly thank you for sticking by my side, even when I was irritable and depressed. Thank you with all my heart and soul. I love you and am forever indebted to you for giving me life, your love, and your heart. Thank you.

1.0   INTRODUCTION

1.1   MOTIVATION

Particle-fluid systems belong to the category of 'soft condensed matter' [1], which generally refers to materials which possess additional 'mesoscopic' length scales between the atomic length scales $(3 \times 10^{-10}\,\text{m})$ and macroscopic length scales $(> 10^{-6}$ m). At the same time, particle-fluid systems can be also viewed as multi-phase flow systems, where the fluid can be in a phase of gas, liquid, and even multi-phase flow, and the particles are of a different phase. Numerous particle-fluid flow systems exist in industrial processes, such as in the fields of oil and gas, printing, pharmaceuticals, and so on; however, many of the transition phenomena and interaction mechanisms of such systems on the microscopic level are still unclear. Thus, investigation of such multi-phase systems from the mesoscopic level needs to be furthered to cope with the demand of various academic research needs and intensive industrial applications.

Particle-fluid systems are increasingly important in the field of microfluidics [2]. One promising application is in nanofluids, where heat transfer characteristics can be highly improved with nanoparticles dispersed evenly in the liquid [3-7]. This is shown for experimental results; however, the microscopic mechanism of this improvement is still uncertain. Several kinds of mechanisms [8], such as Brownian motion of the nanoparticles, molecular-level layering of the liquid at the liquid/particle interface, the nature of heat transport in the nanoparticles, and

1

the effects of nanoparticle clustering, are proposed to explain the phenomenon, but no consensus has been reached. Thus, more theoretical studies for these kinds of soft matter systems are still needed.

Considering the interactions between the liquid and solid and multi-scale length characteristics of a particulate suspension system, the complexity of the interfacial dynamics and strong non-linear properties will exhibit great challenges for any investigation. Experimental and computational approaches are the two common techniques to construct the theoretical foundation for research. When dealing with the particle-fluid system, experimental investigation cannot always give desirable results due to the huge cost of experimental equipment, the difficulties in satisfying the proscribed research conditions and the inevitable errors from varying and uncontrollable environmental conditions and human factors. Computational analysis, on the other hand, can provide ideal conditions for this research by isolating each of the impact factors and probing into the influence that each impact factor exerts on the particulate suspension systems, which cannot always be reproduced via experimental methods. Furthermore, more precise and theoretical insights to further the investigation can be obtained based on the computational analysis results. Thus, this thesis will focus on a computational analysis approach for studying particle-fluid systems.

1.2   FLUID MODELING TECHNIQUES

Computational fluid dynamics (CFD) is an effective tool that has been applied successfully to investigate the detailed mechanisms of various complex fluid systems, such as particulate suspension systems, high Reynolds number flow, hypersonic flow, etc. Among all of the

numerical methods, the most popular conventional CFD techniques such as finite difference (FD), finite volume (FV), and finite element (FE) methods are based on discretization of the Euler equations or Navier-Stokes equations, both of which are the governing equations of the macroscopic variables in the computational domain, such as the density, velocity, pressure and energy. Thus, the underlying physics on a macroscopic system on a microscopic level are unclear.

Based on the constituents of the particle-fluid systems, which are atoms or molecules, researchers have developed microscopic particle-based methodologies like molecular dynamics (MD) [1], direct simulation Monte Carlo (DSMC) [9], and dissipative particle dynamics (DPD) [10, 11]. However, numerical techniques like MD, as introduced in [12], involve tracing every molecule's location and velocity at every time step from the previous location and velocity via classical mechanics from a microscopic point of view. It is well known that the number of molecules comprising a fluid system is huge (and can be obtained from Avogadro's constant $6.022 \times 10^{23}/mol$), which means huge time and computational resources will be consumed due to the large amount of the molecules in the system.

As opposed to the microscopic MD approach to solve the dynamics of each individual molecule in a system, the lattice Boltzmann method (LBM) approaches a fluid system as being composed of groups of molecules, where the groups of molecules can be represented by the probability function that a given group exists at a certain location and time [13], with a particular momentum in the phase space. The evolution of the probability functions can be mathematically expressed by the Boltzmann transport equation. The LBM has been proven to be an alternative and efficient CFD tool which is initiated from microscopic models and mesoscopic kinetic equations, and has made recent rapid progress in solving various complex fluid flows.

3

One origin of the LBM is from lattice gas automata (LGA). LGA is constructed as a simplified, fictitious molecular dynamics framework in which space, time and particle velocities are all discrete [14]. A set of Boolean variables $n_i(x,t)$ is defined to describe whether the particle is occupied at location x and time t.

The evolution of the LGA is as follows [15]:

$$n_i(x + e_i, t + 1) = n_i(x,t) + \Omega_i\big(n(x,t)\big) \quad (n_i(x,t) = 0, or\ 1, i = 0,1, \dots M), \qquad 1.1$$

where n_i is the Boolean variable, Ω_i is the collision term, e_i is the set of local particle velocities, and M is the number of the velocity directions of the particle. To complete the evolution of the above equation, two sub-steps need to be finished in one time step [16]: (1) free-streaming, where a particle shifts to neighboring sites according to the direction of e_i, and (2) collision, where particles arriving at the same site interact and change their velocity directions according to the collision term $\Omega_i\big(n(x,t)\big)$.

Due to the statistical fluctuations of the LGA, as in any other particle method [17, 18], the LBM was first proposed [19] with the purpose of eliminating the statistical noise. The main feature of the LBM over the LGA is to substitute the particle Boolean variable n_i with an ensemble averaged probability function $f_i = \langle n_i \rangle$, which is a single-particle distribution function (PDF) where the brackets represent the ensemble average. In addition to eliminating the statistical noise, the evolution equation of the LBM is the same as the LGA, where the locality from the kinetic equation is kept, and thus the property of parallelism of the LBM can be maintained [15].

1.3   GOALS OF THE RESEARCH

The LBM has been successfully applied in particulate suspensions [20-25] as an alternative technique to traditional computational fluid dynamics (CFD). The particle-fluid system is distinct from many other complex fluid systems, in that it is fluid-like on long time scales while particles distributed in the fluid responded on short time scales [1]. Thus, to solve such a fluid-particle system, the fluid can be treated as a continuum, which can be solved with the LBM, while the suspended particles' movement, on the other hand, can be treated as solid and solved by Newton's equation of motion. When dealing with a particulate suspension system via the LBM, a main concern is how to accurately couple the fluid and solid domains, which essentially is the treatment for the boundary condition at the fluid-solid interfaces. In traditional CFD algorithms, the most common Neumann boundary condition and Dirichlet boundary condition can be fulfilled through the macroscopic variables. One simple example is the non-slip boundary condition, which imposes the velocity of the fluid immediately adjacent to the boundary wall as equal to the velocity of the wall.

However, unlike imposing the non-slip boundary conditions through macroscopic variables, there is no analogous physical-meaning-based boundary condition at the mesoscopic level. Therefore, the boundary conditions of the LBM need to convert macroscopic information to the applicable mesoscopic PDFs. The bounce-back boundary condition, which possesses first order accuracy, played an important role in the first implementations of the LBM algorithm [26, 27]. However, due to the slip velocity caused by the first order accuracy of the bounce-back boundary condition, bounce-back-on-the-link (BBL) boundary conditions with second order accuracy were proposed [28-30]. Later, boundary conditions for an at-rest body with complex geometries have been proposed to locate the boundary nodes more accurately at the real body

surface [31-33]. When a solid body begins to move in a fluid, Ladd first proposed a moving boundary condition by adding an exchanged momentum term based on the BBL boundary condition [29, 30], which is obtained by obeying mass and momentum conservation. Aidun et al. [34, 35] then made corrections for Ladd's boundary condition by considering the scenario that the PDFs inside the solid moving body will transfer to the outside and the outside PDFs will transfer to the inside of the body surface.

Due to the virtual boundary nodes located at the middle of the link connecting the fluid nodes and solid nodes in Ladd's moving boundary condition, it is difficult to conserve the geometric integrity of a particle, which is essential for the particle's dynamics. Boundary conditions which can capture the geometries more accurately are mainly applied for surfaces at rest. Therefore, a moving boundary condition which can maintain geometric integrity is important for particle suspension systems. The research in this thesis will mainly focus on developing the model of the particle suspension systems and proposing a more accurate moving boundary condition scheme. Based on comprehensive investigation on the boundary conditions for the moving boundaries and in-depth theoretical study, a novel moving boundary condition based on the Chapman-Enskog expansion will be proposed, which exhibits great numerical accuracy and stability in comparison to previous boundary conditions.

1.4 ORGANIZATION OF THE THESIS

The rest of the content in this thesis will be organized as follows.

In Chapter 2, the numerical realization of the LBM and units transformation between the LBM system and the real physical system will be introduced.

In Chapter 3, a comprehensive investigation on the boundary conditions for the particle suspension flows is presented. Different kinds of boundary conditions based on the previous mathematical derivation imposed on the particle-fluid interface are investigated in detail, such as boundary conditions for a flat wall, a cylindrical surface at rest, and a moving cylindrical surface.

In Chapter 4, benchmark simulations for classical fluid flows are tested with the lattice Boltzmann method with these various boundary conditions.

In Chapter 5, a novel moving boundary condition based on the Chapman-Enskog expansion for the lattice Boltzmann method will be introduced in detail. Computational experiments with the new boundary condition for classical fluid flows were carried out. Great numerical accuracy and stability of the new boundary condition are validated through comparison with the analytical solutions and existing boundary conditions. The Galilean invariance characteristic of the new boundary condition is also demonstrated by simulating a cylinder's movement in a channel under two different frames of reference.

Finally, in Chapter 6, conclusions will be made from the results of the previous chapters and directions for future work will be explored.

2.0   LATTICE BOLTZMANN METHOD

The lattice Boltzmann method (LBM) can be derived from the Boltzmann transport equation, describing the evolution of the particle distribution function (PDF) $f(x, \xi, t)$ in phase space. The essential theoretical foundation of the LBM is the recovery from the mesoscopic Boltzmann equation to the macroscopic Navier-Stokes (N-S) equations.

Two approaches are successfully applied in proving the recovery of the N-S equations from the Boltzmann equation. One is Grad's 13-moments method [36, 37], where particle distribution functions are projected on Hermite polynomials, while the other one is the Chapman-Enskog expansion, which can be also viewed as a multi-scale expansion method [38], where the particle distribution functions are expanded based on different orders of the Knudsen number (Kn). More details about the Chapman-Enskog approach can be found in references [12, 15, 39, 40].

2.1   THE LATTICE BOLTZMANN-BGK EQUATION

The Boltzmann transport equation (BTE), which describes the statistical behavior of a thermodynamic system not in thermodynamic equilibrium was devised by Ludwig Boltzmann in 1872. The primary parameter in the BTE is introduced as the phase-space

distribution function $f(x, \xi, t)$, which has a physical meaning: the probability of finding a particle at the location x with the momentum ξ at time t. Under the approximation of a dilute gas, which includes uncorrelated velocities for two particles, local collisions, and no external forces exerted on particles, the Boltzmann equation derived from the Liouville equation can be written as:

$$(\partial_t + \xi \cdot \nabla_x + g \cdot \nabla_\xi) f(x, \xi, t) = Q(f, f) \qquad \text{2.1}$$

where g is the acceleration and $Q(f, f)$ is the collision integral, and has the form of:

$$Q(f, f) = (\partial_t f)_{collision} = \int d\xi_1 \int |\xi - \xi_1| (f(\xi')f(\xi_1') - f(\xi)f(\xi_1)) d\Omega \, \sigma(\Omega). \qquad \text{2.2}$$

In equation 2.2, $\sigma(\Omega)$ is the differential collision cross section for the two-particle collision which transforms the momentums from (ξ, ξ_1) into (ξ', ξ_1'), where (ξ, ξ_1) are the moments of the two-particles before collision, and (ξ', ξ_1') are the moments after collision.

The local equilibrium state can be established from the Boltzmann transport equation by introducing the Boltzmann H-theorem. The Boltzmann's H-function [41, 42] is defined as:

$$H(t) = H(f(x, \xi, t)) = \int f(x, \xi, t) \log f(x, \xi, t) d\xi, \qquad \text{2.3}$$

where,

$$\frac{dH}{dt} = \int d\xi \frac{\partial}{\partial t} [f(x, \xi, t) \log f(x, \xi, t)] = \int d\xi \frac{\partial f(x, \xi, t)}{\partial t} [1 + \log f(x, \xi, t)]. \qquad \text{2.4}$$

Based on the mathematical manipulation introduced in [42], the Boltzmann H-theorem can be proved to be:

$$\frac{dH}{dt} \leq 0, \qquad \text{2.5}$$

if $f(x, \xi, t)$ satisfies the Boltzmann transport equation. It should be noted that $\frac{dH}{dt} = 0$ if and only if $\frac{\partial f}{\partial t} = 0$, based on which the thermal equilibrium state can be established.

The H-function is related to the thermodynamic entropy S through $S(f) = -k_B H(f)$ [43]. Based on the H-theorem, where the H is a non-increasing quantity, the entropy never decreases in time, regardless of the details of the collision operator, which is the foundation of the second law of thermodynamics.

For the system under the thermal equilibrium state, which means $\frac{\partial f}{\partial t} = 0$, the solution of the Boltzmann equation will lead to the Maxwell-Boltzmann distribution :

$$f^{eq}(x, \xi, t) = \frac{\rho(x, t)}{\left(2\pi\theta(x, t)\right)^{D/2}} exp\left(-\frac{(\xi - u)^2}{2\theta(x, t)}\right),$$ 2.6

where $\rho(x, t)$ and $u(x, t)$ are the density and velocity of the fluid at location x and time t, θ is defined as $\frac{k_B T}{m}$, k_B is the Boltzmann constant, m is the molecular mass of the gas particles, T is the absolute temperature, and D is the dimension of the system.

Because of the complexity of the collision term in the Boltzmann equation, simplifying the collision term is essential to solving the Boltzmann equation. To simplify the collision term, two rules need to be satisfied: the first is that the collision term conserves all macroscopic variables, while the other is that the collision term should bear the tendency of the distribution to the Maxwell-Boltzmann distribution function by the H-theorem. Several simplified collision operator schemes were proposed by Higuera and Jimenez [44] and Higuera et al [45]. Among all of these schemes, Bhatnagar, Gross and Krook [46] developed the most widely used model to fulfill both of the rules for the collision term. The Boltzmann-BGK equation has the form of:

$$\left(\partial_t + \xi \cdot \nabla_x + g \cdot \nabla_\xi\right)f(x, \xi, t) = -\frac{1}{\tau}(f - f^{eq})$$ 2.7

where τ is the relaxation time and f^{eq} is the Maxwell-Boltzmann distribution function in the equilibrium state, as defined in equation 2.6.

2.2 NUMERICAL REALIZATION OF THE LATTICE BOLTZMANN METHOD

In this section, the implementation of the LBM needs to be numerically realized to solve fluid problems. In order to apply the LBM to simulate fluid flows numerically, the equation must be discretized. At the same time, for distinct lattice structures, velocities with different magnitudes in different directions, as well as the weights for different velocities, need to be obtained.

For simplicity, assuming there is no external force, which means $g = 0$, the Boltzmann-BGK equation discretized in time and space has the following form:

$$\frac{f_i(x, t + \Delta t) - f_i(x, t)}{\Delta t} + \frac{1}{\Delta x_i} \xi_i [f_i(x + \Delta x, t + \Delta t) - f_i(x, t + \Delta t)]$$

$$= -\frac{1}{\lambda} [f_i(x, t) - f_i^{eq}] \qquad \qquad 2.8$$

where $f_i = f(x, \xi_i, t)$ is the PDF of the ith velocity, ξ_i is the ith velocity vector, and f_i^{eq} is the equilibrium PDF. Under the assumption $\Delta x_i = \xi_i \Delta t$, the discretized lattice-BGK model for simulation can be expressed as:

$$f_i(x + \xi_i \Delta t, t + \Delta t) = f_i(x, t) - \frac{1}{\tau} [f_i(x, t) - f_i^{eq}(x, t)], \qquad i = 0, \dots, n \qquad 2.9$$

where $f_i(t + \Delta t)$ is the PDF after collision and streaming, $f_i(t)$ is the PDF before collision, and $\tau = \lambda / \Delta t$ is the non-dimensional relaxation time.

Two common lattice structures that are widely used in 2-D space and 3-D space are shown in Figure 2-1 and Figure 2-2, respectively. These models are known as the D2Q9 and D3Q19 lattices, which are characterized as nine velocities in two-dimensional space and nineteen velocities in three-dimensional space.
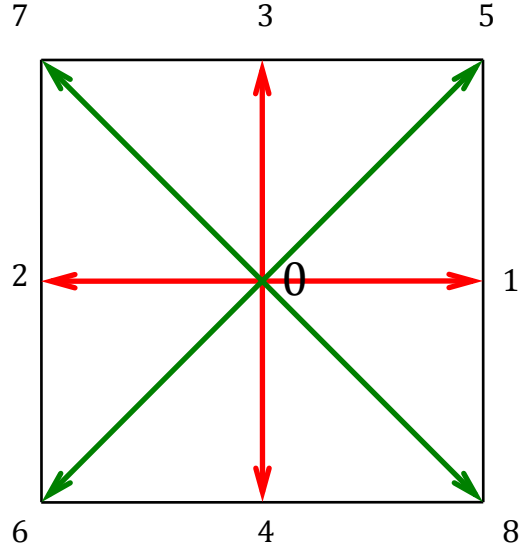
Figure 2-1: The D2Q9 lattice model.
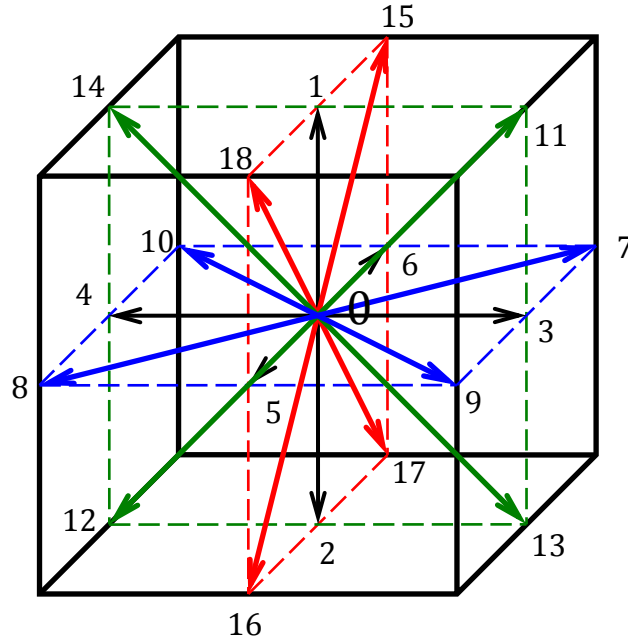
Figure 2-2: The D3Q19 lattice model.

As introduced in [47], the discretized EDF has the form of:

$$f_i^{eq} = \rho \omega_i \left[1 + \frac{3}{c_s^2} (\xi_i \cdot u) + \frac{9}{2c_s^4} (\xi_i \cdot u)^2 - \frac{3}{2c_s^2} u \cdot u \right] \qquad 2.10$$

and the discrete velocity set $\{\xi_i\}$ can be obtained explicitly from [47-49]. For the D2Q9 structure, it is known that:

$$\xi_0 = (0,0), for\ i = 0,$$

$$\xi_i = (1,0), (-1,0), (0,1), (0,-1), for\ i = 1,2,3,4, \qquad 2.11$$

$$\xi_i = \sqrt{2}((1,1), (-1,-1), (-1,1), (1,-1)), for\ i = 5,6,7,8.$$

and the weighting coefficients ω_i have the following values:

$$\omega_i = \begin{cases} \dfrac{4}{9}, & i = 0, \\ \dfrac{1}{9}, & i = 1,2,3,4, \\ \dfrac{1}{36}, & i = 5,6,7,8. \end{cases} \qquad 2.12$$

With the discretized velocity space, the hydrodynamic moments can be obtained as:

$$\rho = \sum_{i=0}^{8} f_i = \sum_{i=0}^{8} f_i^{eq} \qquad 2.13$$

$$\rho u = \sum_{i=0}^{8} e_i f_i = \sum_{i=0}^{8} e_i f_i^{eq} \qquad 2.14$$

The speed of sound of the D2Q9 model is $c_s^2 = \dfrac{c^2}{3}$, where $c = \dfrac{\Delta x}{\Delta t}$, so then the state equation of an ideal gas is $p = \rho c_s^2$. To recover the Navier-Stokes equation in the incompressible limit ($Ma = u/c \ll 1$)[50], up to the leading order truncation error, the kinetic viscosity can be obtained as [51]:

$$v = \left(\tau - \frac{1}{2}\right) c_s^2 \Delta t \qquad 2.15$$

For the above expression 2.15, τ must be greater than 0.5, so that the kinetic viscosity is positive.

To complete the discretized lattice-BGK equation 2.9, two sub-steps need to be finished in one time step:

13

$$\text{Collision: } f_i^+(x,t) = f_i(x,t) - \frac{1}{\tau}\left[f_i(x,t) - f_i^{eq}(x,t)\right], \text{ and} \qquad 2.16$$

$$\text{Streaming: } f_i(x + e_i \Delta t, t + \Delta t) = f_i^+(x,t), \qquad 2.17$$

where f_i and f_i^+ denote the particle distribution function's state before and after the collision step, respectively. From equation 2.16, we know that the collision process is purely local. As can be seen from equation 2.17, during the streaming step, the PDFs shift to the nearest neighboring nodes according to the discrete velocity direction ξ_i. The way in which this PDF shifting is altered by boundaries is then discussed in the following chapter.

Due to the kinetic nature of the LBM, there are several distinct features of the LBM compared with the traditional N-S solver CFD techniques:

1. In the LBM, the convection terms (streaming process) are linear; the N-S solver must deal with nonlinear convective terms. The combination of the streaming process and collision process can recover the mesoscopic BTE to the macroscopic N-S equations.

2. For incompressible flow, the pressure can be obtained easily with the LBM by the equation of state $p = \rho c_s^2$. On the other hand, the Poisson equation needs to be solved for the pressure field in the N-S solver.

3. For an explicit numerical scheme, the Courant-Friedrichs-Lewy (CFL) condition ($CFL = u\frac{\Delta t}{\Delta x} < 1$) [16] is a basic stability criterion, which implies that the physical speed u can not travel faster than the highest speed can be supported by the discrete lattice grid $c = \frac{\Delta x}{\Delta t}$. In the LBM, the CFL number can be obtained as $CFL = u\frac{\Delta t}{\Delta x} = \frac{u}{c} = Ma \ll 1$ (incompressible limit), so that the LBM satisfies the CFL condition all of the time.

4. For implementing boundary conditions (BCs), which are essential for modeling complex fluid flows, in the LBE model there is no counterpart of the BCs found in a N-S solver, thus the BCs in the LBM need to be transformed into quantities that can be related to the PDFs.

2.3   UNIT TRANSFORMATION BETWEEN THE PHYSICAL SYSTEM AND THE LATTICE BOLTZMANN SYSTEM

To simulate a physically realistic system, developing a technique to rigorously transform the measurable, physical units to lattice units is crucial. A summation of our unit transformation methodology is given in Table 2-1. In that table, "lu" are lattice length units, and "ts" are lattice time units. All of the computational tests discussed in this thesis are strictly based on the unit transformations table as listed below. Details of the units transformation for the numerical tests are given in each of the tests, respectively.

As an example, in order to simulate a real physical fluid flow with a velocity u_p, the procedure will be shown as to how to convert u_p into the lattice Boltzmann velocity u_{lb} based on Table 2-1. First, the mesh resolution Δx needs to be chosen. Second, a value is chosen for the relaxation time parameter τ ($\tau > 0.5$). When that is known, the kinetic viscosity in the lattice Boltzmann system $\nu_{lb} = c_s^2 \left(\frac{\tau-1}{2}\right)\Delta t = \frac{2\tau-1}{6}$ can be determined. Based on the relationship between the kinetic viscosity of these two systems, $\nu_{lb} = \nu_p \times \frac{\Delta t}{(\Delta x)^2}$, the time step Δt can be determined. Finally, with it known that $u_{lb} = u_p \times \frac{\Delta t}{\Delta x}$, the velocity in the lattice Boltzmann system is successfully converted.

Table 2-1: Unit transformations.

Physical system	Lattice Boltzmann system
Length: $L(m)$, Width: $W(m)$, Time: $t(s)$,	Length: $X(lu) = \frac{L(m)}{\Delta x}$, Width: $Y(lu) = \frac{W(m)}{\Delta y}$, Time: $T(ts) = \frac{t(s)}{\Delta t}$, where $\Delta x = \Delta y = 1(lu) = \frac{L}{X}(m)$, $\Delta t = 1(ts) = \frac{t}{T}(s)$.
Density: $\rho_p(kg/m^3)$,	Density: $\rho_{lb} = \rho_p \times \frac{(\Delta x)^3}{\Delta m}$, in most cases, ρ_{lb} is set to be 1.0, so the lattice mass Δm can be chosen to satisfy that.
Velocity: $u_p \ (m/s)$,	Velocity: $u_{lb} = u_p \times \frac{\Delta t}{\Delta x}$.
Kinetic viscosity: $\nu_p = \frac{\mu}{\rho}(m^2/s)$,	Kinetic viscosity: $\nu_{lb} = c_s^2\left(\frac{\tau-1}{2}\right)\Delta t = \frac{2\tau-1}{6}$, where τ is the relaxation time parameter, $c_s = \frac{1}{\sqrt{3}}$ is the speed of sound, and $c = \frac{\Delta x}{\Delta t} = 1(\frac{lu}{ts})$ is the propagation speed, so $\nu_{lb} = \nu_p \times \frac{\Delta t}{(\Delta x)^2}$.
Reynolds number: $Re = \frac{\rho_p u_p D_p}{\mu_p} = \frac{u_p D_p}{\nu_p}$, where D_p is the characteristic length.	Reynolds number: $Re = \frac{\rho_{lb} u_{lb} D_{lb}}{\mu_{lb}} = \frac{u_{lb} D_{lb}}{\nu_{lb}}$.
Pressure: $P_p \ (kg/m^2 \cdot s^2)$,	Pressure: $P_{lb} = c_s^2 \rho_{lb} = c_s^2 \rho_p \times \frac{(\Delta x)^3}{\Delta m}$.

Table 2-1 (continued).

Gravity: g_p,	Gravity: $g_{lb} = g_p \times \frac{(\Delta t)^2}{\Delta x}$.

3.0   BOUNDARY CONDITIONS

Of course, in implementing the lattice-BGK method, consideration must be given to a fluid's interaction with open and solid boundaries. Moreover, in a particulate suspension system, a profound understanding of the hydrodynamic interaction between the particle and fluid at the mesoscopic level is required, and thus researching the interface between the fluid and solid surface is of the most interest in this dissertation. In traditional CFD algorithms, the non-slip boundary conditions can be fulfilled by bounding the macroscopic variables; i.e., setting velocities at the body surface equal to the velocities of the fluid adjacent to the body. However, unlike imposing non-slip boundary conditions through the macroscopic variables, there is no physically analogous boundary condition at the mesoscopic level. Hence, methodologies for non-slip boundary conditions need to be transferred to mesoscopic PDFs in the lattice Boltzmann method.

Before delving into the investigation on the solid-fluid interfaces, the periodic boundary condition must be introduced first, where the realistic boundary of a computational domain can be defined to give any meaningful numerical results. The basic order to execute the LBM is listed in Figure 3-1. For a computational domain that is $M \times N$ in length and width, as shown in Figure 3-2, after execution of both of the collision and streaming processes in one time step, the PDFs located at $(1, y = 1, ..., N)$ with directions 1, 5, and 8 are unknown while the PDFs located

18

at $(M, 1, \dots, N)$ with directions 2, 7, and 6 are unknown. Then the x-direction periodic boundary conditions are specified as follows to give the unknown PDFs:

$$f_i(1, y) = f_i(M + 1, y), \text{ and } f_i(M, y) = f_i(0, y).$$

3.1

$$f_{-i}(x_f = x_b + e_{-i}\Delta t, t + \Delta t) = f_{-i}(x_b, t^+)$$

3.2
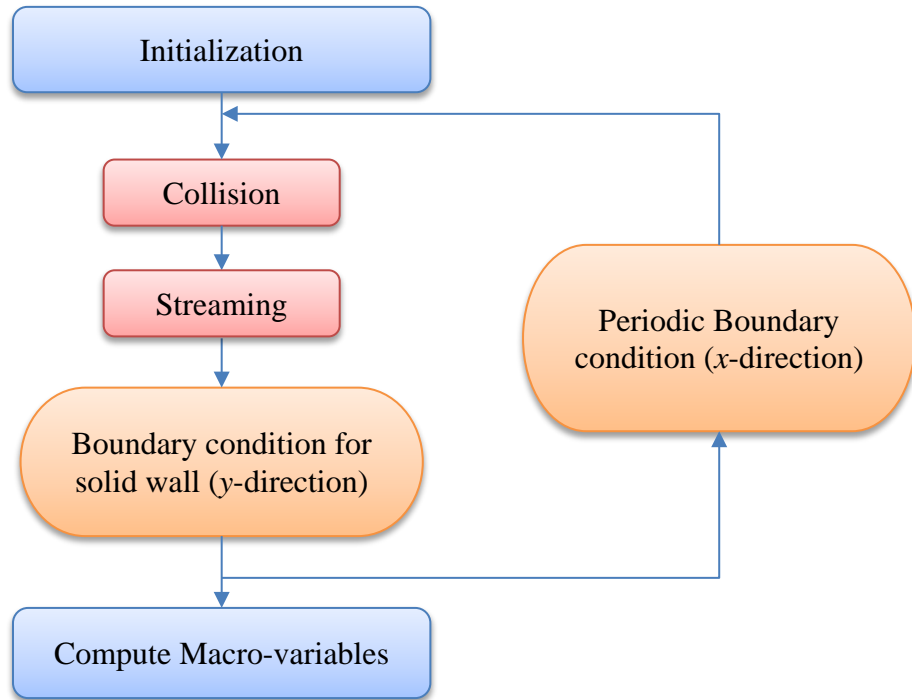
Figure 3-1: The flowchart of the basic order of the LBM algorithm.
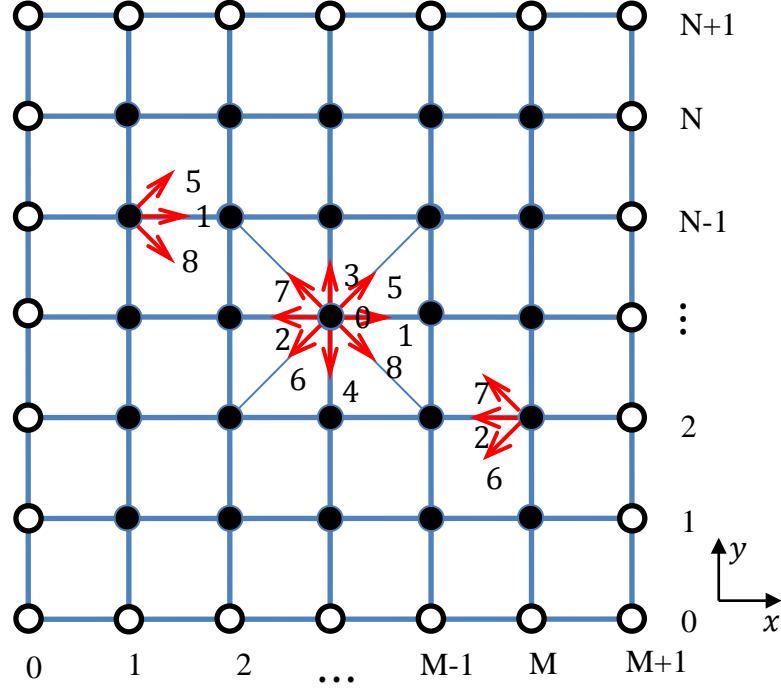
Figure 3-2: The periodic boundary. The solid circles are the lattice nodes while the open circles are the buffer layer nodes.

Next, the treatment of PDFs for the boundary condition for the solid-fluid boundary will be explained more explicitly based on Figure 3-3 . As introduced in equations 2.16 and 2.17, the PDF at each fluid node needs to experience collision and streaming processes to implement the LBM algorithm in one time step Δt. For example, there is a PDF $f_i(x, t)$ (where $f_i(x, t) = f(x, e_i, t)$, x is the location, e_i is the velocity vector, and t is the time) located at x_f. After the local collision process, this PDF will shift to the neighbor node located at x_b based on the direction vector e_i. However, due to the impermeability of the boundary wall, the PDF will bounce-back with direction e_{-i} (reversed direction of e_i, and $e_{-i} = -e_i$), which is $f_{-i}(x_f, t + \Delta t)$.
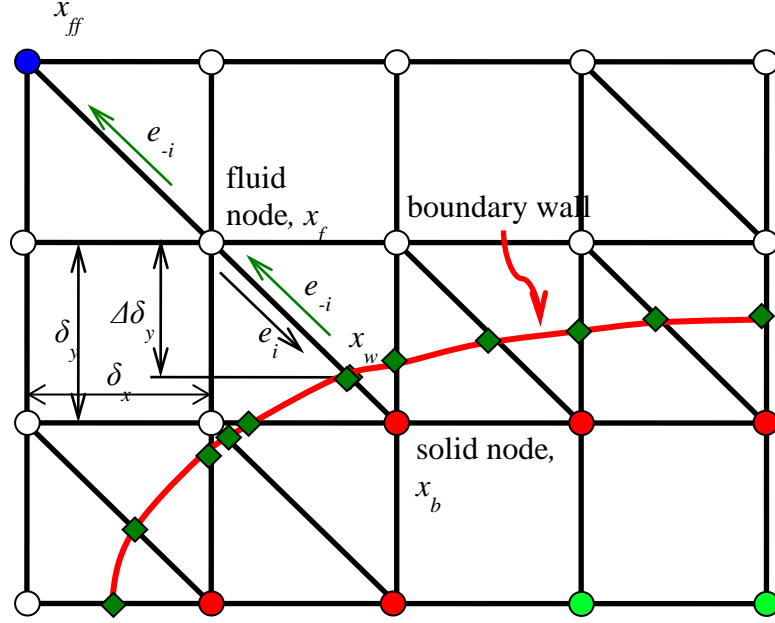
Figure 3-3: Layout of the curved surface mapped on the regular lattices in 2-D space. The red curved line denotes the body surface. The open circles denote the fluid nodes. The red solid circles denote the solid nodes with connections to the fluid nodes. The green solid circles denote the solid nodes without connections to fluid nodes.

From the description, we know that the information of f_{-i}^+ at location x_b is necessary to finish the streaming process:

$$f_{-i}(x_f = x_b + e_{-i}\Delta t, t + \Delta t) = f_{-i}(x_b, t^+).$$ 3.3

However, the PDFs in the solid area are unknown, and thus the main focus is to obtain the $f_{-i}(x_b, t^+)$ with the direction of e_{-i} to finish the streaming process in one time step Δt.

In order to quantify different techniques for balancing these PDFs, a variety of boundary conditions are investigated comprehensively and applied to the LBM algorithm in this chapter.

3.1 FULL WAY BOUNCE-BACK AND HALF WAY BOUNCE-BACK BOUNDARY CONDITIONS

In order to simulate a non-slip boundary condition, much of the previous work on the boundary conditions of the LBM on a mesoscopic level [27, 29, 52-60] has focused on the full way bounce-back boundary condition [27, 52, 53] and half way bounce-back boundary condition [29].

In order to approximate the non-slip boundary condition, the full way bounce-back boundary condition, also known as the on node bounce-back boundary condition, assumes that the PDFs of the fluid nodes collide with the solid boundary and simply reflect back in the opposite direction of the incoming velocity with the same magnitude. Taking Figure 3-4 as an example, the explicit numerical expression for a D2Q9 model by applying this boundary condition is $f_6 = f_5$, $f_4 = f_3$, and $f_8 = f_7$, and the general numerical expression is:

$$f_{-i}(x, t + 1) = f_i(x, t), \qquad\qquad 3.4$$

However, due to the poor first order numerical accuracy in space, a finite slip velocity will always exist on the boundary wall [52, 57].
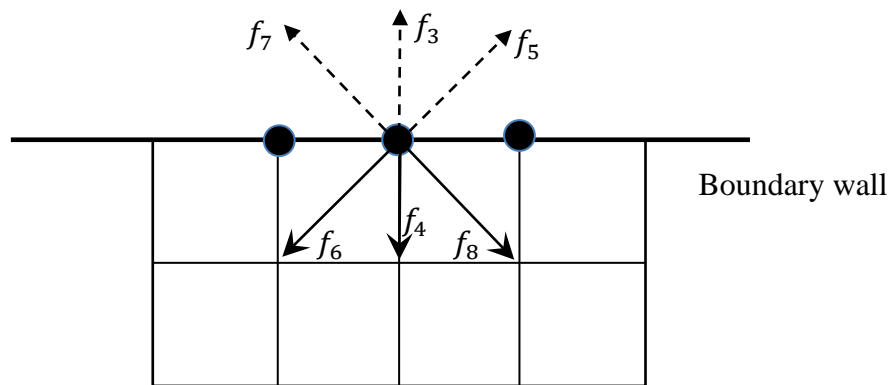
Figure 3-4: Full way bounce-back boundary condition, where the boundary wall is located on the lattice nodes.

In order to improve the numerical accuracy and reduce the slip velocity at the boundary, the half way bounce-back boundary condition was developed, where the wall boundary is simply placed in the middle of the lattice nodes, as shown in Figure 3-5. The half way bounce-back boundary condition is also known as bounce-back on the link (BBL) [23], and has been proven to give second order numerical accuracy [16, 52, 54]. The half way bounce-back boundary condition has been shown to provide a good level of performance when dealing with boundaries parallel to the lattice grid, such as flat walls and channel surfaces. The explicit scheme of the BBL as illustrated in Figure 3-5 is $f_6 = f_5$, $f_4 = f_3$, and $f_8 = f_7$, and the general form of the BBL is:
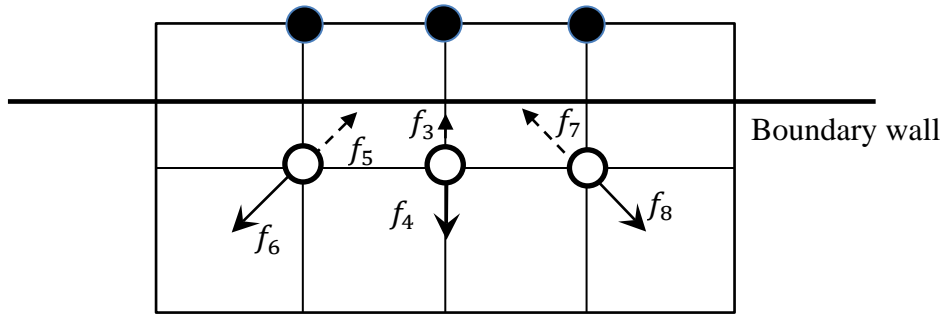
Figure 3-5: The BBL boundary condition, where the boundary wall is located in the middle of the links connecting the buffer layer (solid circles) and fluid nodes (open circles).

$$f_{-i}(x, t+1) = f_i(x, t^+),\qquad\qquad 3.5$$

However, when dealing with curved boundaries, simply placing the boundary wall in the middle of two lattice nodes to simulate the non-slip boundary condition will degrade the shape resolution of the body immersed in the flow field, and the force exerted on the body at finite and high Reynolds numbers cannot be obtained correctly. Due to the "stair-step" approximated boundary, the geometric integrity of the body cannot be preserved, which is important for

vorticity generation and stress distributions. Both of these are sensitive to the geometric resolution of the half way bounce-back boundary condition when the Reynolds number is high [32]. For high Reynolds number flows, boundary conditions based on interpolation in curvilinear coordinates were proposed [61, 62] to overcome the geometry issues.

3.2   THE BOUNDARY CONDITION BASED ON INTERPOLATION

A boundary scheme based on the linear and quadratic interpolation was proposed by Bouzidi et al. [56], which can capture the exact locations of the boundary wall for both still and moving boundaries. The details of the derivation of this momentum transfer based boundary scheme is reviewed in the following section.

An intersection fraction is defined as: $q = \frac{|CW|}{|CD|}$ ($0 \leq q \leq 1$), which denotes the distance between the lattice node in the fluid domain and the boundary wall. This scheme takes into consideration two circumstances, $0 \leq q \leq 1/2$ (Figure 3-6) and $1/2 \leq q \leq 1$ (Figure 3-7), and boundary schemes for the two different circumstances are illustrated in the next sub-sections, respectively.

1. When $0 \leq q \leq 1/2$, the boundary condition for a static wall can be obtained as follows. After the collision process, the PDF at C is $f_i(x_C, t^+)$, and to implement the streaming process, this PDF will travel $\Delta x = 1$ in one time step $\Delta t = 1$ from C to the wall W and bounce-back until it reaches E (because $0 \leq q \leq 1/2$, and the location of E will be between B and C). The PDF will then become $f_{-i}(x_c, t + 1)$. From the standard LBM scheme, as described in equation 2.17, we know that $f_{-i}(x_C, t + 1) = f_i^+(x_D, t)$. However, the $f_i^+(x_D, t)$ is unknown to

us due to the impermeability of the boundary wall located at W. We make the assumption that

$f_{-i}(x_C, t + 1) = f_i^+(x_E, t)$, where $f_i^+(x_E)$ is a fictitious PDF at E after the collision. This PDF

will implement the streaming process by starting at E and will travel through C and arrive at the

wall W, and then bounce-back until it arrives at C (the dotted line in Figure 3-6) in one time step

$\Delta t = 1$. Thus, the boundary condition can construct the PDF at C with the direction of $-i$

$(f_{-i}(x_c, t + 1))$.
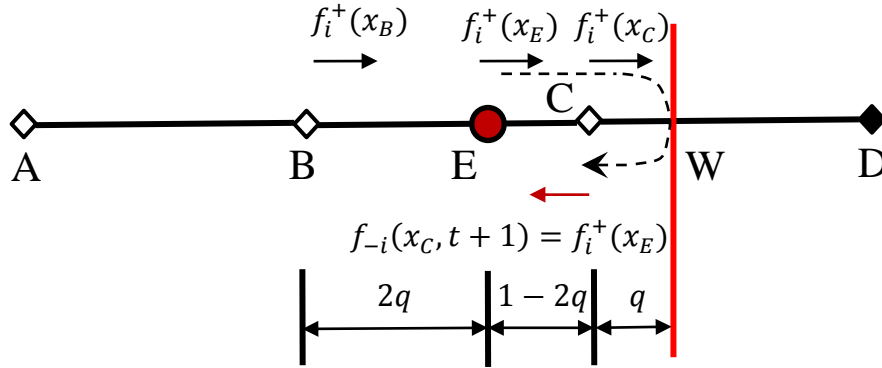
Figure 3-6: Sketch of the interpolation boundary scheme for $0 \leq q \leq 1/2$, where the open diamonds represent the lattice nodes at the fluid domain, the solid diamond represents the lattice node in the solid domain, the boundary wall is located at W, and E denotes the starting point of the PDF arriving at C after a time step.

From Figure 3-6, we know that after collision, $f_i^+(x_E, t)$ will stream $\Delta x = 1$ and arrive at

C, and then become $f_{-i}(x_c, t + 1)$. From the definition of q, we know that $|CW| = q$; thus, the

distance of $|EC|$ is $|EC| = 1 - 2q$, and $|BE| = |BC| - |EC| = 1 - (1 - 2q) = 2q$. Based on

the assumption that $f_{-i}(x_C, t + 1) = f_i^+(x_E, t)$, we can state the linear interpolation scheme for

$f_i^+(x_E, t)$ as:

$$\frac{f_i^+(x_C, t) - f_i^+(x_E, t)}{|CE|} = \frac{f_i^+(x_E, t) - f_i^+(x_B, t)}{|BE|} \tag{3.6}$$

With $|CE|$ and $|BE|$ known, the PDF at the fictitious node E is:

$$f_i^+(x_E, t) = 2qf_i^+(x_C, t) + (1 - 2q)f_i^+(x_B, t) \tag{3.7}$$

This PDF will stream to the wall and bounce-back and arrive at C after a whole streaming process; thus, the PDF at C after streaming is:

$$f_{-i}(x_c, t + 1) = f_i^+(x_E, t) = 2qf_i^+(x_C, t) + (1 - 2q)f_i^+(x_B, t) \tag{3.8}$$

For the quadratic interpolation scheme, the Lagrange polynomial is applied to obtain the unknown PDF. The Lagrange polynomial has the general form of:

$$y(x) = L_0(x)y_0 + L_1(x)y_1 + L_2(x)y_2, \tag{3.9}$$

where $L_0(x) = \frac{(x-x_1)(x-x_2)}{(x_0-x_1)(x_0-x_2)}$, $L_1(x) = \frac{(x-x_0)(x-x_2)}{(x_1-x_0)(x_1-x_2)}$, and $L_2(x) = \frac{(x-x_1)(x-x_0)}{(x_2-x_1)(x_2-x_0)}$.

Setting the origin of the coordinate at $x_0 = x_A = 0$, $x_1 = x_B = 1$, $x_2 = x_C = 2$, and $x = x_E = 1 + 2q$, we then have:

$$L_0(x) = \frac{(x-1)(x-2)}{(x_0 - x_1)(x_0 - x_2)} = \frac{(x-1)(x-2)}{2} = \frac{2q(2q-1)}{2}, \tag{3.10}$$

$$L_1(x) = -x(x-2) = -(1 + 2q)(1 + 2q - 2), \text{ and} \tag{3.11}$$

$$L_2(x) = \frac{x(x-1)}{2} = \frac{(1+2q)(1+2q-1)}{2}, \tag{3.12}$$

with it known that $y_0 = f_i^+(x_A, t)$, $y_1 = f_i^+(x_B, t)$, and $y_2 = f_i^+(x_C, t)$. Remembering the assumption that $f_{-i}(x_c, t + 1) = f_i^+(x_E, t)$, then the quadratic scheme for the unknown PDF can be obtained by substituting $L_0(x)$, $L_1(x)$, and $L_2(x)$ with y_0, y_1, and y_2 into equation 3.9 as :

$$f_{-i}(x_c, t + 1) = q(2q - 1)f_i^+(x_A, t) + (1 + 2q)(1 - 2q)f_i^+(x_B, t)$$
$$+ (1 + 2q)qf_i^+(x_C, t). \tag{3.13}$$

2. When $1/2 \leq q \leq 1$, the streaming destination of the PDF starting from C will be E, which will be located between C and D rather than between B and C. After the collision process, the PDF $f_i^+(x_C, t)$ will travel from C to W and then bounce-back at the wall until arriving at E after one time step Δt (the dotted line in Figure 3-7). We make the assumption that $f_{-i}(x_E, t + 1) = f_i^+(x_C, t)$, where C will be located between B and E, and thus the interpolation scheme can be applied. With it known that $|CW| = q$, $|CB| = 1$, and $|CE| = 2q - 1$, the unknown $f_{-i}(x_C, t + 1)$ can be obtained by applying the linear interpolation scheme as:
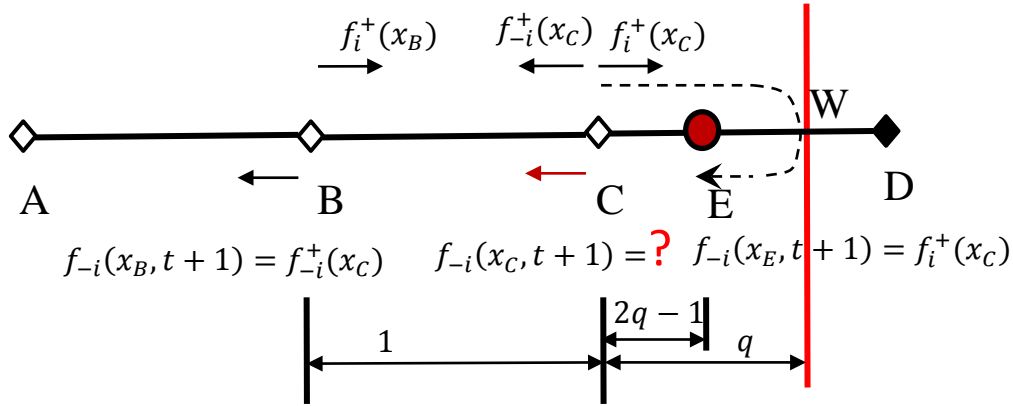
Figure 3-7: Sketch of the interpolation boundary scheme for $1/2 \leq q \leq 1$, where the open diamonds represents the lattice nodes at the fluid domain, the solid diamond represents the lattice node in the solid domain, the boundary wall is located at W, and E denotes the destination of the PDF after one time step trip.

$$\frac{f_{-i}(x_C,\ t + 1) - f_{-i}(x_B,\ t + 1)}{|CB|} = \frac{f_{-i}(x_E,\ t + 1) - f_{-i}(x_C,\ t + 1)}{|EC|},$$ 3.14

and then the unknown $f_{-i}(x_C, t + 1)$ is:

$$f_{-i}(x_C, t+1) = \frac{1}{2q} f_{-i}(x_E, t+1) + \frac{2q-1}{2q} f_{-i}(x_B, t+1)$$

$$= \frac{1}{2q} f_i^+(x_C, t) + \frac{2q-1}{2q} f_{-i}^+(x_C, t)$$

3.15

For the quadratic interpolation scheme, the Lagrange polynomial is applied to obtain the unknown PDF, just as introduced for $0 \leq q \leq 1/2$.

Setting the origin of the coordinate $x_1 = x_B = 0$, thus, $x_0 = x_A = -1$, , $x_2 = x_E = 2q$, and $x = x_c = 1$, and we have:

$$L_0(x) = \frac{x(x-2q)}{(x_0-x_1)(x_0-x_2)} = \frac{1(1-2q)}{2q+1},$$

3.16

$$L_1(x) = \frac{(x+1)(x-2q)}{-2q} = \frac{2q-1}{2q}, \text{ and}$$

3.17

$$L_2(x) = \frac{x(x+1)}{2q(2q+1)} = \frac{1}{q(2q+1)},$$

3.18

with it known that $y_0 = f_{-i}(x_A, t+1)$, $y_1 = f_{-i}(x_B, t+1)$, and $y_2 = f_{-i}(x_E, t+1)$. Keeping in mind the streaming process defined in equation 2.17, we know that $f_{-i}(x_A, t+1) = f_{-i}^+(x_B, t)$, $f_{-i}(x_B, t+1) = f_{-i}^+(x_C, t)$, and $f_{-i}(x_E, t+1) = f_i^+(x_C, t)$. Substituting equations 3.16-3.18 and y_0, y_1 and y_2 into equation 3.9, the quadratic interpolation scheme of $f_{-i}(x_c, t+1)$ can be obtained as:

$$f_{-i}(x_c, t+1) = \frac{1-2q}{1+2q} f_{-i}^+(x_B, t) + \frac{2q-1}{2q} f_{-i}^+(x_C, t) + \frac{1}{q(2q+1)} f_i^+(x_C, t).$$

3.19

For boundaries with velocities, more detailed information about Bouzidi's boundary scheme can be found in [56].

3.3   CURVED BOUNDARY CONDITIONS

To overcome the degraded accuracy when dealing with a curved geometry, Filippova and Hänel

(FH) [31, 63] proposed a boundary condition at the interaction surface when a curved geometry

is placed in a flow, with simulation tests of an unsymmetrical cylinder in the channel

investigated in detail [31]. The FH boundary condition scheme can be illustrated as follows.

First, we introduce a fraction of an intersected link $\Delta = \frac{|x_f - x_w|}{|x_f - x_b|}$, where the locations of

x_f, x_w, and x_b are shown in Figure 3-3. Obviously, $0 \leq \Delta \leq 1$, and the horizontal distance

between x_f and x_w is $\Delta \cdot \delta_x$. Since $\delta_x = \delta_y$, the horizontal and vertical distances between x_f and

x_w are the same. As mentioned before, for PDFs after the collision step at time t^+, the

information of $f_{-i}(x_b, t^+)$ is needed to implement the streaming process, where $f_{-i}(x_f = x_b +$

$e_{-i}\Delta t, t + \Delta t) = f_{-i}(x_b, t^+)$. However, $f_{-i}(x_b, t^+)$ is unknown to us, so Filippova and Hänel

proposed a construction scheme for $f_{-i}(x_b, t^+)$ as:

$$f_{-i}(x_b, t^+) = (1 - \chi)f_i(x_f, t^+) + \chi f_i^*(x_f, t) + 2\omega_i \rho \frac{3}{c^2} e_i \cdot u_w \qquad 3.20$$

where u_w is the boundary wall's velocity, and χ is the weighting factor (which is unknown and

needs to be calculated) which controls the linear interpolation between $f_i(x_f, t^+)$ and $f_i^*(x_f, t)$.

To solve the FH boundary scheme in equation 3.20, the first step is to construct the

fictitious equilibrium distribution function f_i^* by the following expression:

$$f_i^*(x_f, t) = \omega_i \rho(x_f, t)\left[1 + \frac{3}{c^2} e_i \cdot u_{bf} + \frac{9}{2c^4}(e_i \cdot u_f)^2 - \frac{3}{2c^2} u_f \cdot u_f\right] \qquad 3.21$$

where u_f is the velocity of the fluid adjacent to the boundary wall and u_{bf} needs to be

determined based on the fraction parameter Δ, fluid velocity u_f and wall velocity u_w:

$$u_{bf} = (\Delta - 1)\frac{u_f}{\Delta} + \frac{u_w}{\Delta}, \text{ and } \chi = \frac{(2\Delta-1)}{\tau}, \text{ when } \Delta \geq \frac{1}{2} \qquad\qquad 3.22$$

$$u_{bf} = u_f, \text{ and } \chi = \frac{(2\Delta-1)}{\tau-1}, \text{ when } \Delta < \frac{1}{2}. \qquad\qquad 3.23$$

From the above expressions, we know that when the choice of the τ value is close to 1, χ will be infinite when $\Delta < \frac{1}{2}$. Thus, the stability behavior of this boundary scheme can be problematic when applying the original FH scheme. The stability region figures for classic fluid flows can be found in [32]. Due to the flexibility of the construction for the u_{bf} in the fictitious equilibrium distribution function given in equation 3.21, Mei et al. [32, 33, 64] modified the u_{bf} in the original FH scheme when $\Delta < \frac{1}{2}$ to avoid the numerical instability caused by infinite χ:

$$u_{bf} = u_{ff} = u_f\left(x_f + e_{-i}\Delta t, t\right), \text{ and } \chi = \frac{2\Delta-1}{\tau-2}, \text{ when } \Delta < \frac{1}{2}. \qquad\qquad 3.24$$

After the modification of χ and u_{bf} for $\Delta < \frac{1}{2}$, the stability region can be highly expanded for different Δ and τ [32].

It should be noted that, for the original FH boundary scheme and the modified FH boundary scheme, neither considered specified treatments for the nodes inside the body (the green solid circles in Figure 3-3), which have no adjacent connections to the fluid nodes. However, to model the particle's dynamics in the fluid, the lattice nodes inside the solid body also need to be treated to keep the whole computational region consistent. Thus, a moving boundary scheme is needed to be able to model the particle's dynamics in the fluid.

3.4   BOUNDARY CONDITION FOR A CURVED BOUNDARY WITH A VELOCITY

To simulate the dynamics of a solid body immersed in a fluid with the LBM, there are two types of approaches to describe the moving boundary condition: one is a momentum-exchange algorithm [65-67], first proposed by Ladd [28], and the other is an immersed boundary algorithm [68-70], first introduced by Peskin [71].

The scheme Ladd proposed is based on the momentum conservation between the particle nodes and fluid nodes during the process of collision. Thus, mass and momentum are conserved for the whole region. As shown in Figure 3-8, the map of the boundary nodes for a circular body is marked. In Ladd's method, the boundary nodes are located at the center of the links connecting the fluid nodes and solid nodes. Thus, the computational geometry of the body is denoted as the red dashed lines. In this boundary treatment, both the nodes inside and outside of the body surface are treated as a fluid, where all of the nodes experience collision and streaming. Therefore, all of the nodes can be calculated to keep the whole computational domain consistent.
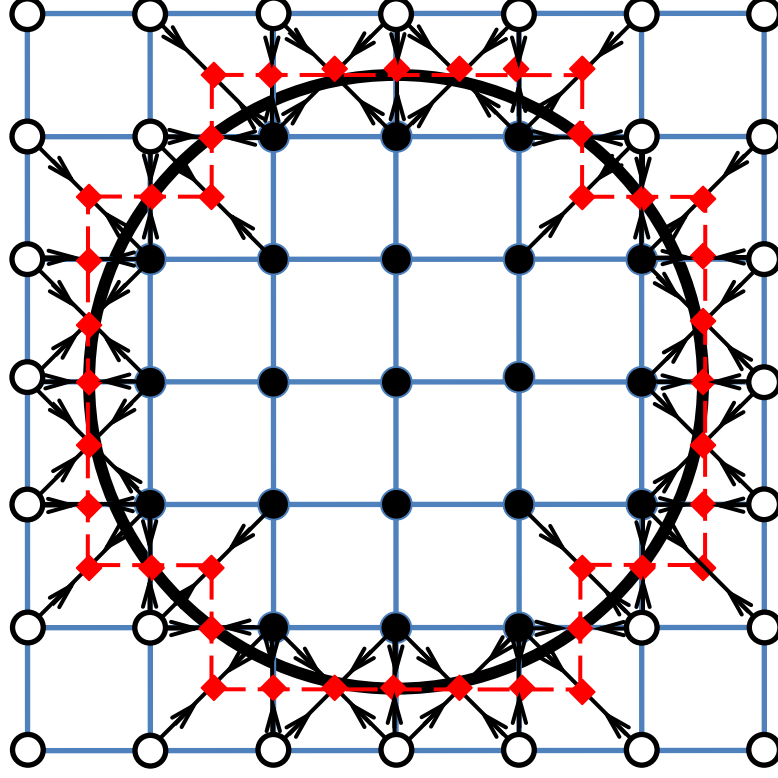
Figure 3-8: Layout of the boundary nodes for a circular body with a diameter of 5 lattice lengths. The PDF's directions are shown with the arrows. The position of the boundary nodes are marked as ◆, the solid nodes are marked as ●, and the fluid nodes marked as ○. The surface of the body used in the calculation is marked as the red dashed line ----.

When the PDFs of a fluid node with $f_i(x_f, t^+)$ and a solid node with $f_{-i}(x_w, t^+)$ come from opposite directions into a static boundary node located at x_b, neither of the two PDFs can stream to the next lattice nodes due to the impermeability of the solid surface, as shown in Figure 3-9, and will therefore bounce-back after the streaming process with $f_{-i}(x_f, t + \delta t)$ and $f_i(x_w, t + \delta t)$, respectively, which can be expressed as:

$$f_{-i}(x_f, t + \Delta t) = f_i(x_f, t^+) \qquad 3.25$$

$$f_i(x_w, t + \Delta t) = f_{-i}(x_w, t^+) \qquad 3.26$$

Before streaming, at time t

After streaming, at time $t + \Delta t$
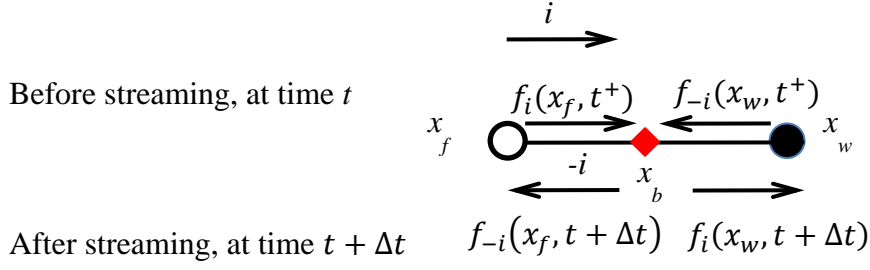
Figure 3-9: Particle distribution function (PDF) before and after streaming at the boundary node ◆.

For a scenario with boundary nodes with a velocity u_b, the PDFs after streaming can be calculated based on the momentum exchange with the following scheme [1, 28]:

$$f_{-i}(x_f, t + \Delta t) = f_i(x_f, t^+) + \frac{2}{c_s^2} \omega_i \rho u_b \cdot e_i \qquad 3.27$$

$$f_i(x_w, t + \Delta t) = f_{-i}(x_w, t^+) - \frac{2}{c_s^2} \omega_i \rho u_b \cdot e_i \qquad 3.28$$

where u_b is the velocity of the boundary node. It can be calculated through the following expression:

$$u_b = U + \Omega \times (x_b - R) \qquad 3.29$$

where U is the translational velocity of the body, Ω is the rotational velocity of the body, $x_b = x_f + \frac{1}{2} \Delta t \cdot e_i$ is the location of the boundary node, and R is the center location of the body.

3.5   PARTICLE SUSPENSION MODEL

In order to investigate the particle suspension system, there are two important aspects that need to be taken into consideration besides the boundary condition.

The first aspect is the particle suspension model. Ladd's shell model [28, 29] and Aidun, Lu, and Ding's (ALD's) model [34] are two common models for the numerical investigation. The main feature of Ladd's shell model is the lattice nodes both inside the solid surface and outside the solid surface are treated as fluid nodes, where the fluid nodes will experience both streaming and collision processes. ALD's model, on the other hand, excludes the interior fluid nodes and identifies fluid nodes covered or uncovered at each time step. An impulse force (IMP) will be introduced when the solid particle moves to cover or uncover the fluid nodes; however, no detailed physical meaning interpretation of the IMP and the use of IMP is clarified [72].

The second aspect is the force evaluation. Momentum exchange (ME) [29, 72] and stress integration (SI) [24] are two common methods applied to calculate the force exerted on the solid surfaces. In this dissertation, the ME proposed by Ladd is studied in detail, and more information about the method of SI can be found in [62, 73].

For a boundary node interaction occurring at the surface, the force exerted at the boundary nodes x_b, as shown in Figure 3-9, can be expressed as:

$$F\left(x_b = x_f + \frac{1}{2}e_i, t + \frac{1}{2}\Delta t\right) = -(f_i(x_w, t + \Delta t) - f_{-i}(x_f, t + \Delta t)$$

$$-f_i(x_f, t^+) + f_{-i}(x_w, t^+)) \qquad\qquad 3.30$$

$$= 2\left[f_i(x_f, t^+) - f_{-i}(x_w, t^+) - 2\frac{\omega_i}{c_s^2}\rho u_b \cdot e_i\right]e_i.$$

Based on the above expression, the force and torque exerted on the whole solid body, F_s and T_s, can be obtained by summing the forces and torques at each boundary node over the entire surface:

$$F_s = \sum_{BN} F(x_b) \qquad 3.31$$

$$T_s = \sum_{BN} (x_b - R) \times F(x_b) \qquad 3.32$$

With the forces and torques exerted on the particle known, updating the particle velocities can be solved by Newton's equations of motion:

$$M \frac{dU(t)}{dt} = F_s(t) \qquad 3.33$$

$$I \frac{d\Omega(t)}{dt} = T_s(t) \qquad 3.34$$

For a 2-D simulation, the particle's mass and moment of inertia are $M = \rho_s \pi r^2$ and $I = \frac{M}{2} r^2$, respectively.

In Ladd's boundary scheme, both the lattice nodes inside and outside of the solid body are treated as a fluid, where instabilities exist in the particle update process [50]. Aidun et al. [50, 74] subsequently modified Ladd's scheme by taking into account the momentum exchange between the solid nodes flowing to the outside of the surface and the fluid nodes flowing to the inside of the surface. However, Aidun's scheme can result in a violation of the global mass conservation when two surfaces become too close [30]. Later, Ladd et al. [30] pointed out that instabilities can be eliminated with an appropriate choice of the density ratio between the solid and fluid.

Based on the previous introduction in this chapter, the interpolation based boundary condition, the original FH boundary scheme, and the modified FH scheme can be applied for fluid flow with complex surfaces but not for moving solid surfaces due to a lack of treatment of the inside lattice nodes, while Ladd's scheme can be applied for moving boundaries with some geometric integrity compensation; thus, to overcome the shortcomings in both of these approaches, the research in this dissertation will mainly focus on proposing a more sophisticated boundary condition which can be applied for moving boundaries without geometric integrity compensation for the particle-fluid system.

4.0 DEVELOPMENT OF THE NUMERICAL MODEL

In the previous chapter, it was shown that the modified FH boundary condition proposed by Mei et al. [32] demonstrates strong performance for simulation of complex surfaces. Thus, for the development of our model, the modified FH boundary condition will be applied for static boundaries, such as a static flat wall boundary and a static curved geometry. Next, building on that, Ladd's boundary condition will be used for modeling the moving curved geometry.

In this chapter, the rigorous unit transformations between the physical system and lattice Boltzmann system that were previously established in this thesis are applied, and the parameters in all of our simulation tests are based strictly on this unit transformation. Simulation tests based on the modified FH scheme are carried out step by step to develop the particle-fluid system model in this dissertation.

4.1 COUETTE FLOW

Couette flow, which is one of the most common and simple flow models in fluid mechanics, will be used as an example case, as an effective way to help us to validate the development of our model. Couette flow is characterized by one stationary boundary wall and one boundary wall moving at a constant velocity, as shown in Figure 4-1.

The parameters for the simulation test were chosen such that the wall velocity is $u_{top\_wall} = 0.05$, and $u_{bottom\_wall} = 0.00$, and the channel width is $L = 11\ (lu)$.
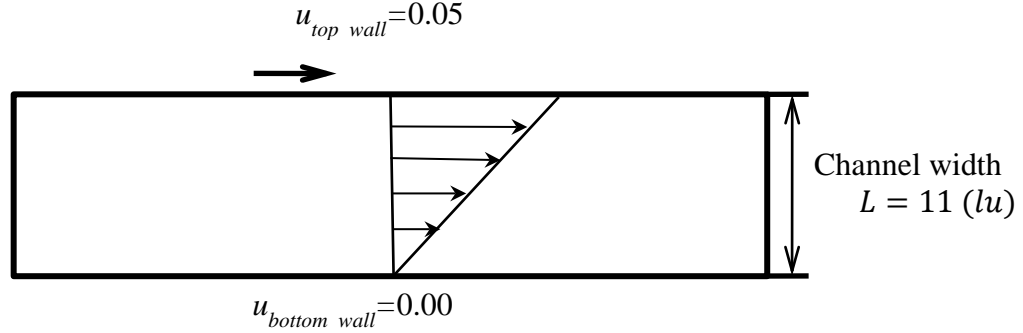
Figure 4-1: Sketch for the Couette flow.

Based on the analytical solution of the Couette flow, when there is no pressure gradient, the x-velocity along the y-direction has the analytical form [75]: $u(y) = \left(u_{top\_wall} - u_{bottom\_wall}\right)\frac{y}{L}$, which means that the x-direction velocity has a linear relationship with the location along the y-direction and is independent with location in the x-direction.
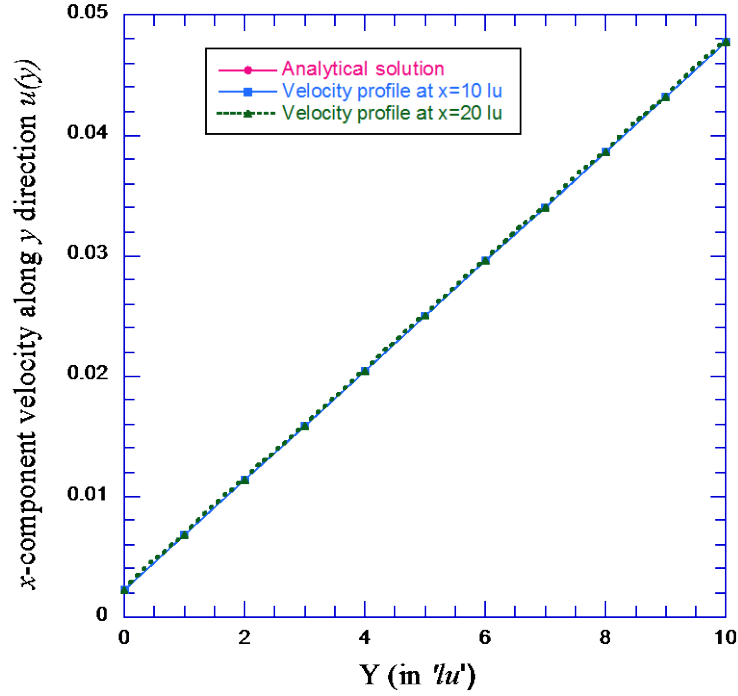
Figure 4-2: Different locations' *x*-direction velocity along the *y*-axis.

The Couette flow is modeled to check the FH boundary condition when the boundary is a flat wall. From Figure 4-2, it can be seen that the velocities obtained by the LBM agree well with the analytical solution at different locations along the *x*-axis even when there are only eleven lattice units along the *y*-direction.

4.2 FLOW OVER A STATIC 2D CYLINDER

After validating the modified FH boundary condition for the flat wall boundary, we need to demonstrate the accuracy of this boundary scheme for handling complex geometries. A uniform flow with velocity U_0 flowing over a column cylinder of radius a as shown in Figure 4-3, at a

39

finite Reynolds number, which is defined by $Re = \frac{\rho U_0 (2a)}{\mu} = \frac{U_0 (2a)}{\nu}$, is investigated in this

subsection.
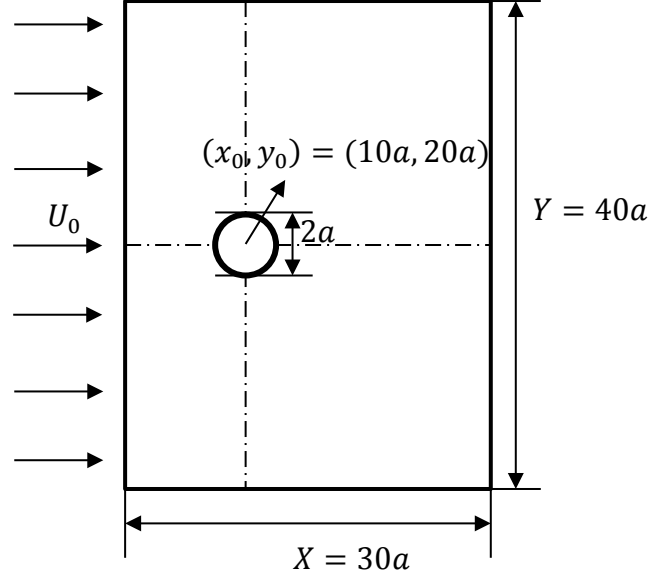
Figure 4-3: Sketch of the flow over a static 2D cylinder.

The center of the cylinder is located at $(10a, \ 20a)$, and the whole computational domain size is $0a \leq y \leq 40a, 0 \leq x \leq 30a$. For the case of $Re = 10$, the unit transformations are listed in Table Table 4-1 and the simulation results are displayed in Figure 4-4 and Figure 4-5.

Table 4-1: Unit transformations for curved geometry test.

Physical system	Lattice Boltzmann system
Length: $L = 1.05\ (cm)$, Width: $W = 1.4\ (cm)$, Radius of the cylinder: $R = 0.035\ (cm)$.	$X = 30a = 105\ lu$, $Y = 40a = 140\ lu$, $a = 3.5\ lu$, $\Delta x = \Delta y = 1(lu) = \dfrac{L}{X}(m) = 10^{-4}(m)$, $\Delta t = 6.67 \times 10^{-4}\ (s)$
Kinetic viscosity: $\nu_p = 10^{-6}(m^2/s)$,	$\nu_{lb} = \dfrac{2\tau-1}{6} = \dfrac{2\times0.7-1}{6} = \nu_p \times \dfrac{\Delta t}{(\Delta x)^2}$, since Δx is known, we can calculate $\Delta t = 6.67 \times 10^{-4}s$.
Reynolds number: $Re = 10$,	$Re = \dfrac{UD_{lb}}{\nu_{lb}} = \dfrac{U\times7}{\frac{2\times0.7-1}{6}} = 10$,
Velocity: $U_p = u_{lb} \times \dfrac{\Delta x}{\Delta t} = 0.0142\ (\dfrac{m}{s})$.	With the above expression for Reynolds number, the velocity can be obtained as: $U = 0.095$.

In Figure 4-4, the centerline $(y = 20a)$ velocity profiles for both the upstream and downstream velocities are shown for the case of $Re = 10$. In Figure 4-5, the velocity profile $u(x = 10a, y = 20a)/U$ for the same case is presented. All of the results are shown in lattice Boltzmann system units. The results shown in Figure 4-4 are the x-direction upstream and downstream centerline velocities of the cylinder when the Reynolds number is 10. From Figure 4-5, the variance of the normalized velocity profile at $x = 10a$ with the increase of the y/a is shown for the whole computational domain, and the maximum value of u/U falls into the region

41

of 1.2-1.3, which matches the results of [32], where half of these computational domain results are presented.
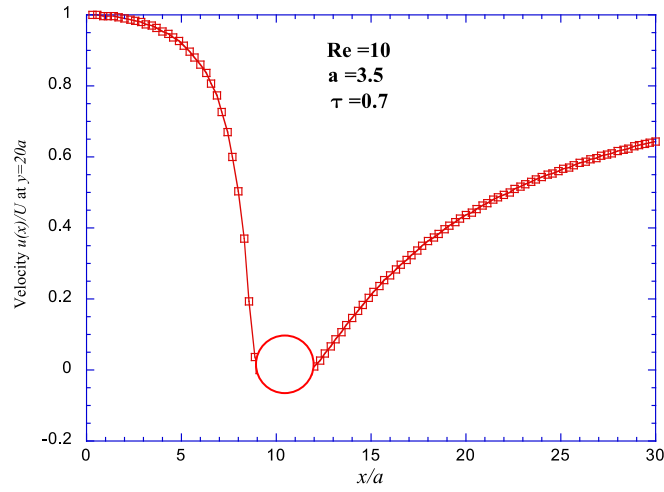
Figure 4-4: The upstream and downstream centerline $(y = 20a)$ velocity profiles.
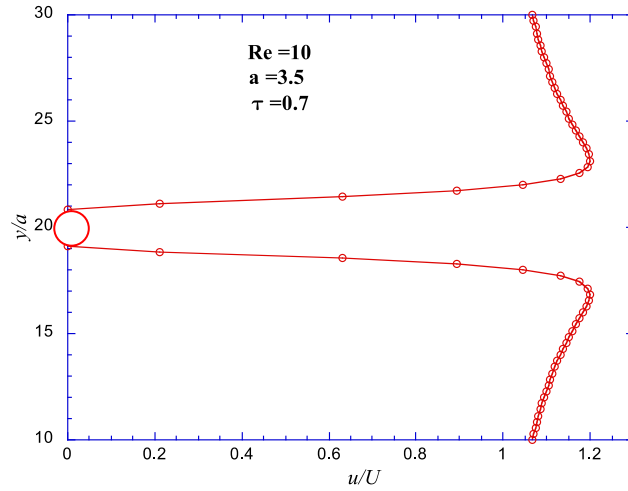
Figure 4-5: The normalized velocity profile (u/U) at $x = 10a$, as a function of y/a for $Re = 10$. The presented distance is $H = 20a = 70\ lu$.

To further validate the modified FH scheme's ability to preserve geometric integrity, a series of computational tests are carried out for a cylinder's radius $R = 3.0, 3.4, 3.5, 3.6, 3.8$, and 4.0. For the cases of $R = 3.4, 3.6$, and 3.8, the parameters $\Delta = \frac{|x_f - x_w|}{|x_f - x_b|}$, as introduced and defined in Section 3.3, are different for these three cases. Thus, to validate this scheme's capability to capture the exact locations of the boundaries, the flow fields for the same Reynolds number should be the same when the coordinates are normalized to the cylinder radius R. The simulation results are shown in Figure 4-6, Figure 4-7, and Figure 4-8. As shown in Figure 4-6 and Figure 4-7, the centerline velocities for all six tests are in excellent agreement with each other for both the upstream and downstream regions, and the same results can be found in [32]. Moreover, the normalized velocity profile u/U as a function of y/R at the center location $x = 10a$ is compared for all six cases. Agreement between the simulations for different radii can be seen from Figure 4-8, where the same results can be observed in [32].
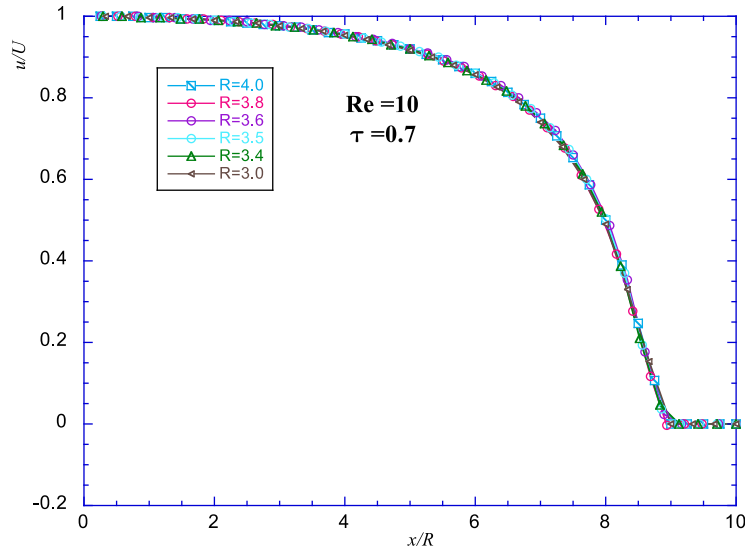
Figure 4-6: Upstream centerline velocity for $R = 3.0, 3.4, 3.5, 3.6, 3.8$, and 4.0 for $Re = 10$.
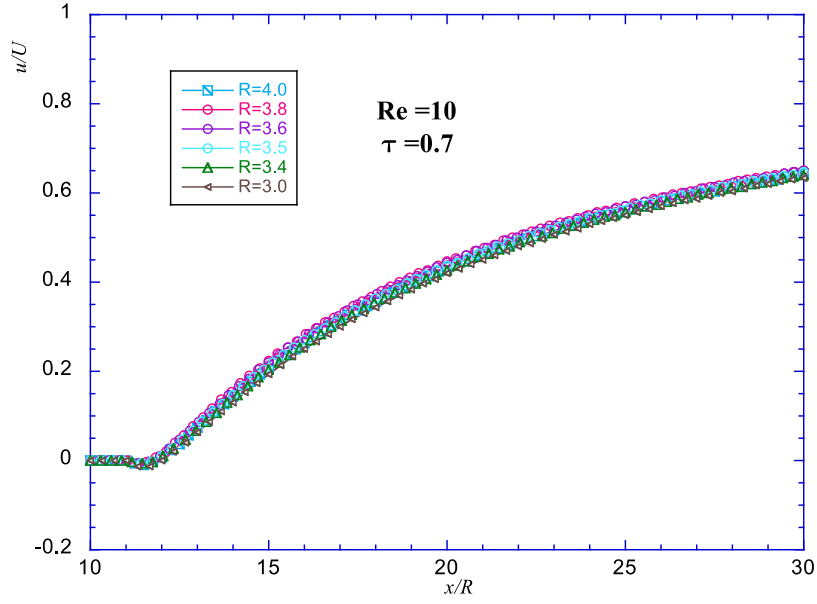
Figure 4-7: Downstream centerline velocity for $R = 3.0, 3.4, 3.5, 3.6, 3.8,$ and 4.0 for $Re = 10$.
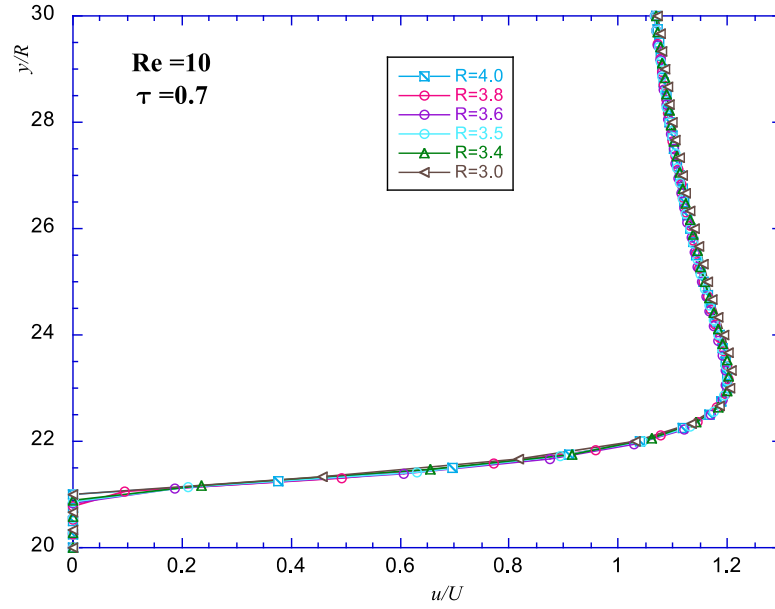
Figure 4-8: Normalized velocity profile at $x = 10a$, as a function of y/R for $Re = 10$ for $R = 3.0, 3.4, 3.5, 3.6, 3.8,$ and 4.0. The presented y-direction distance is $H = 10R$.

For all of the results shown in this subsection, the modified FH boundary scheme can give good results for the whole computational domain and preserve the geometric integrity of a complex surface accurately.

4.3   FORCE EVALUATION FOR THE CYLINDER

The force exerted on a body immersed in a fluid is of great importance when investigating the dynamics of the body. In this section, a force evaluation on an asymmetrically placed cylinder is inspected before simulating the dynamics of the solid particle.

The sketch of the benchmark test is shown in Figure 4-9.
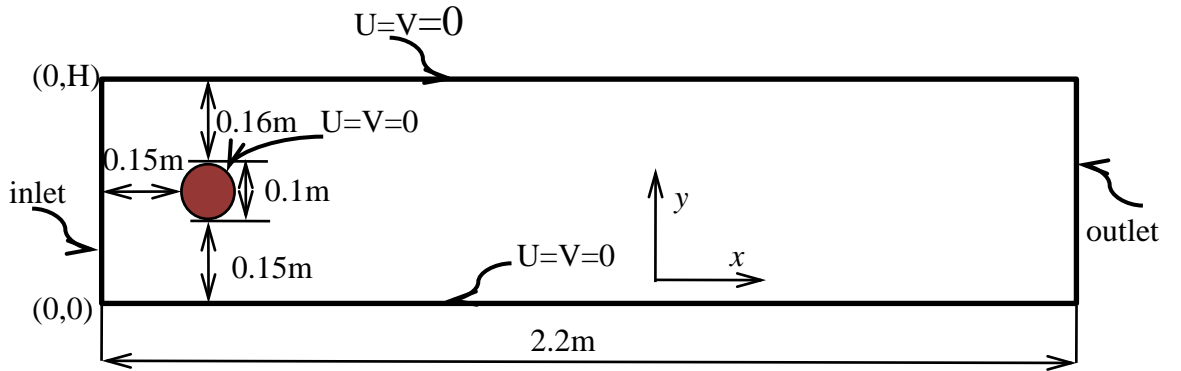
Figure 4-9: Configuration of flow over an asymmetrically placed cylinder in a channel.

The simulation test parameters are chosen following [76], where all of the parameters are in the units of the physical system. Choosing the relaxation time of $\tau = 0.525$, the parameters for our numerical simulation are transformed to the lattice Boltzmann system in Table 4-2.

Table 4-2: Unit transformations for force validation.

Physical system	Lattice Boltzmann system
Length: $L = 2.2\ (m)$, Width: $H = 0.41\ (m)$, Radius of the cylinder: $R = 0.05\ (m)$.	$X = 440\ lu,$ $Y = 82\ lu,$ $a = 10\ lu,$ $\Delta x = \Delta y = 1(lu) = \dfrac{L}{X}(m) = 5 \times 10^{-3}(m),$ $\Delta t = 2.083 \times 10^{-4}\ (s),$
Kinetic viscosity: $\nu_p = 10^{-3}(m^2/s)$,	$\nu_{lb} = \dfrac{2\tau - 1}{6} = \dfrac{2 \times 0.525 - 1}{6} = \nu_p \times \dfrac{\Delta t}{(\Delta x)^2}$, since Δx is known, we can calculate $\Delta t = 2.083 \times 10^{-4} s,$
Reynolds number: $Re = 100$,	$Re = \dfrac{\bar{U} D_{lb}}{\nu_{lb}} = \dfrac{\bar{U} \times 20}{\frac{2 \times 0.525 - 1}{6}} = 100,$
Velocity: $U_{max} = 1.5\ (\frac{m}{s})$, $U_{average} = \bar{U} = \dfrac{2}{3} \times U_{max} = 1.0\ (\frac{m}{s})$.	With the above expression for Reynolds number, the velocity can be obtained as: $\bar{U} = 0.0417.$

Simulation results for the unsteady flow at $Re = 100$ are presented from Figure 4-10 to Figure 4-14. In Figure 4-10, the lift coefficient ($C_L = \frac{F_y}{\rho \bar{U}^2 a}$) and drag coefficient ($C_D = \frac{|F_x|}{\rho \bar{U}^2 a}$) are presented. When $Re = 100$, the flow becomes unsteady and periodic vortex shedding is observed. From Figure 4-10, periodic fluctuations can be found for the lift coefficients and drag coefficients with the evolution of time. Moreover, from Figure 4-11, the period of the lift

coefficient curve is $T \approx 1620\ ts$. Thus, the Strouhal number $St = \frac{2a}{\overline{U}T} \approx 0.296$, which agrees well with the St range of $(0.2950 - 0.3050)$ presented in [76]. Also, the maximum lift coefficient $(C_{L\ max})$ and drag coefficient $(C_{D\ max})$ shown in Figure 4-11 and Figure 4-12 fall into the range given in [76], where the ranges of $C_{L\ max}$ and $C_{D\ max}$ are (3.22-3.24) and (0.99-1.01), respectively. Based on the correct simulation results of $C_{L\ max}$ and $C_{D\ max}$, the x-velocity and y-direction isolines are shown in Figure 4-13 and Figure 4-14.
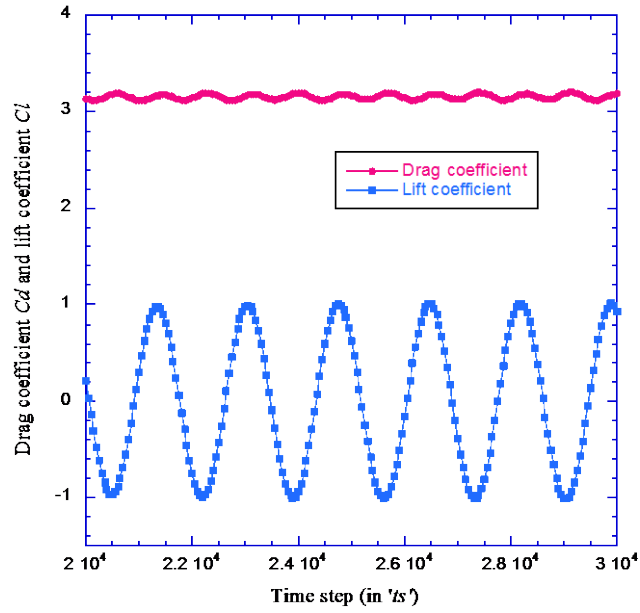
Figure 4-10: The variation of the drag and lift coefficients for $Re = 100$.
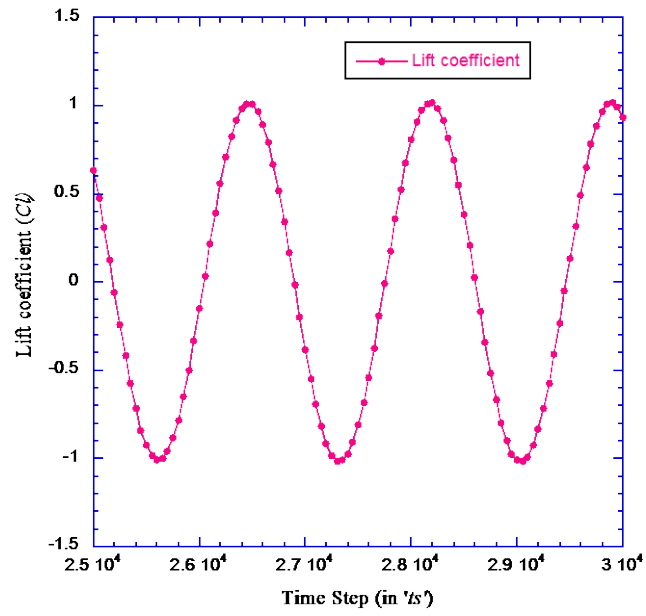
Figure 4-11: The variation of the lift coefficients when Reynolds number is 100.
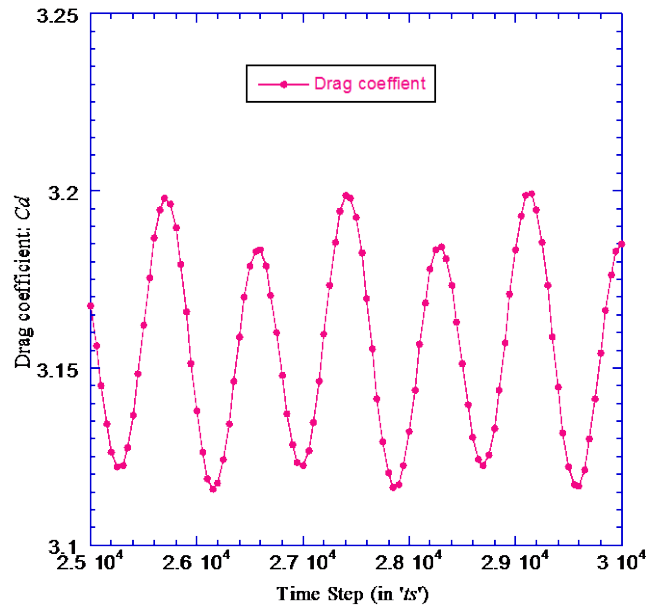
Figure 4-12: The variation of the drag coefficients when Reynolds number is 100.

48
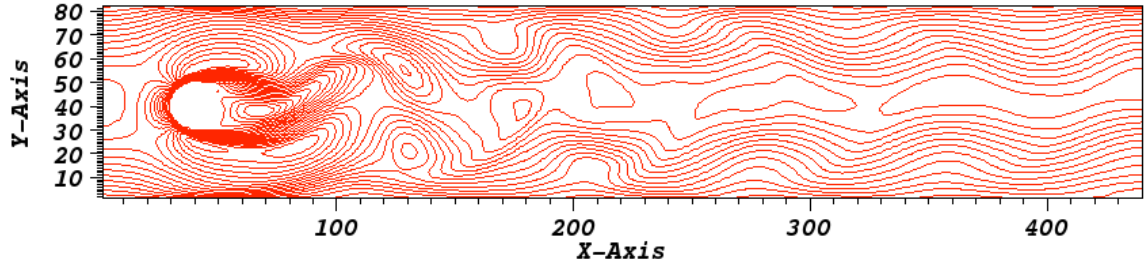
Figure 4-13: Unsteady flow around a cylinder at $Re = 100$. Instantaneous isolines of x-velocity.
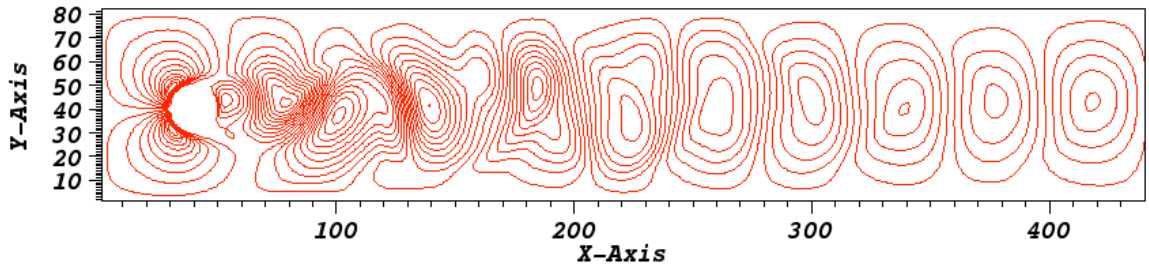
Figure 4-14: Unsteady flow around a cylinder at $Re = 100$. Instantaneous isolines of y-velocity.

Therefore, from the benchmark investigation to validate the force exerted on the asymmetrically placed cylinder, the modified FH boundary condition can be applied to simulate various fluid flows involving static complex surfaces, and exhibits good agreement with other simulation methods for these simple cases.

However, due to the consistency issues over the whole computational domain caused by the lack of treatments for PDFs inside a solid body, boundary conditions involving inside PDFs are in demand for further modeling. Ladd's boundary condition, which involves a treatment for PDFs inside the body and is based on the momentum exchange algorithm, is next applied for numerical tests for the particle's movement when immersed in a fluid.

49

4.4   INVESTIGATION OF A NEUTRALLY BUOYANT CYLINDERIN THE SHEAR

FLOW

In order to study the dynamics of a body immersed in a fluid, the trajectories of the body's movement are the primary results of interest, which can be used to validate the results of the simulation tests. When solving this problem with the LBM, both the lattice nodes inside and outside of the body surface need to be considered to maintain the consistency of the entire computational domain. Because the modified FH boundary condition doesn't update the PDFs inside the body surface, Ladd's boundary condition involving treatment for all the nodes in the computational domain is applied for the simulation tests in this chapter. Both the cylinder's movement in a Couette flow and a Poiseuille flow are investigated.

The motion of a neutrally buoyant particle in a 2D viscous shear flow (which can be viewed as a cylinder in a Couette flow) has been studied in references [20, 68, 77, 78]. Therefore, the simulation parameters of the particle's velocity profiles and trajectories can be chosen to compare with those reference papers. The geometry of the simulation test is shown in Figure 4-15.
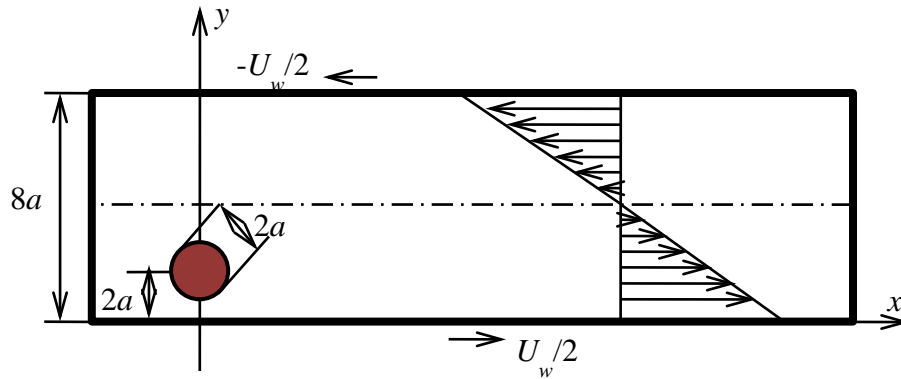
Figure 4-15: Sketch of the simulation model: a neutrally buoyant particle in a 2-D shear flow, Reynolds number $Re = 40$.

Choosing the relaxation time of $\tau = 0.8$ and locating the initial position of the cylinder at $Y_0 = 0.25\,Y = 20\ lu$, all of the other parameters used in the simulation test can be obtained by following the unit transformations listed in Table 4-3.

Table 4-3: Unit transformations for a neutrally buoyant particle.

Physical system	Lattice Boltzmann system
Length: $L = 0.2\ (m)$, Width: $H = 0.008\ (m)$, Radius of the cylinder: $R = 0.001\ (m)$.	$X = 2000\ lu$, $Y = 80\ lu$, $a = 10\ lu$, $\Delta x = \Delta y = 1(lu) = \dfrac{L}{X}(m) = 1 \times 10^{-4}(m)$, $\Delta t = 1 \times 10^{-3}\ (s)$
Kinetic viscosity: $v_p = 10^{-6}(m^2/s)$,	$v_{lb} = \dfrac{2\tau-1}{6} = \dfrac{2\times0.8-1}{6} = v_p \times \dfrac{\Delta t}{(\Delta x)^2}$, since Δx is known, we can calculate $\Delta t = 1 \times 10^{-3}s$,
Reynolds number: $Re = \dfrac{U_w H}{v_p} = 40$,	$Re = \dfrac{U_w Y}{v_{lb}} = \dfrac{\bar{U}\times20}{0.1} = 40$,
Velocity: $U_w = 5 \times 10^{-3}\ (\frac{m}{s})$.	With the above expression for Reynolds number, the velocity can be obtained as: $U_w = \dfrac{1}{20} = 0.05$.
Density: $\rho_f = 1 \times 10^3(kg/m^3)$,	Density: $\rho_{lb} = \rho_p \times \dfrac{(\Delta x)^3}{\Delta m}$, in most cases, ρ_{lb} is set to be 1.0, so the lattice mass Δm is chosen to satisfy that. In this case, choose $\rho_s = \rho_f = 1.0$, where ρ_s is the body's density and ρ_f is the fluid's density.

The simulation results of the particle's movement in Couette flow are shown in Figure 4-16, Figure 4-17, and Figure 4-18. In Figure 4-16, the normalized x-component velocity of the cylinder is presented, while Figure 4-17 is the normalized y-component velocity of the cylinder. From the velocity profiles displayed in Figure 4-16, the maximum value of the normalized x-component translational velocity is 0.25, and after a period of $100\ s$ (which is $10^5\ ts$ based on the unit transformations) it will go to zero; the same results are found in [69, 77]. In Figure 4-17, the peak

of the normalized y-component translational velocity is around 0.005 and goes to zero with very small fluctuations after the same period, which agrees well with the results displayed in [68] . Moreover, the lateral migration of a neutrally buoyant particle, as displayed in Figure 4-18, shows that the particle will move to the centerline of the channel, which means that the centerline of the channel is the stable equilibrium position, as is also stated in [78]. From Figure 4-17, small stable fluctuations of the y-component velocity can be found, where the same small fluctuations can be found in [68]. From the numerical results by applying Ladd's moving boundary scheme, we can tell that even though somewhat good results can be obtained when the x-component velocity dominates the dynamics of the particle, a more accurate moving boundary condition is still needed.
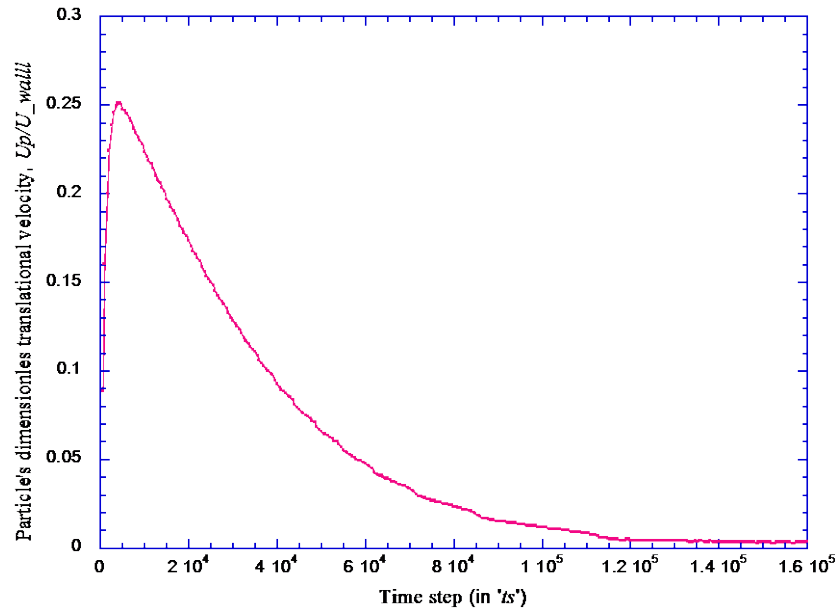
Figure 4-16: The *x*-component dimensionless translational velocity of the particle.
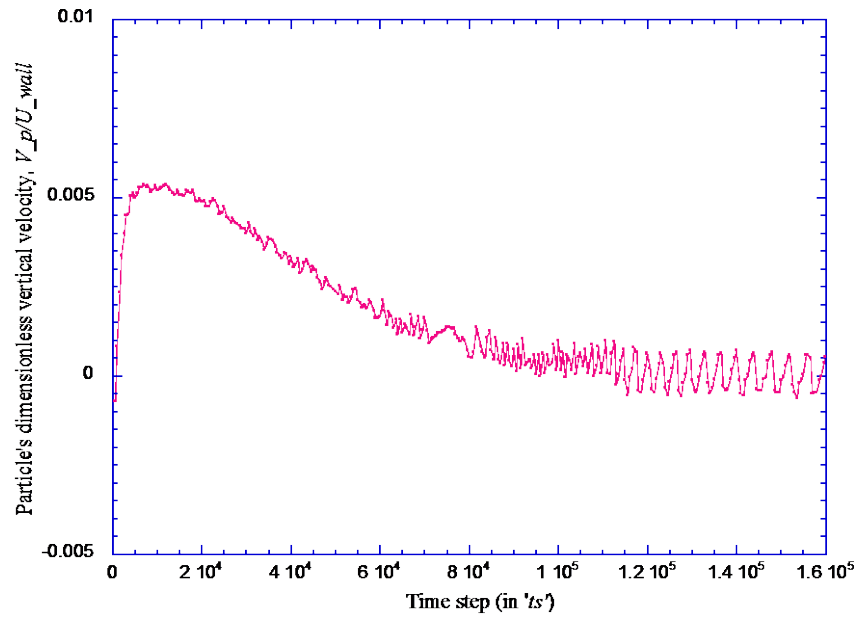
Figure 4-17: The *y*-component dimensionless velocity of the particle.
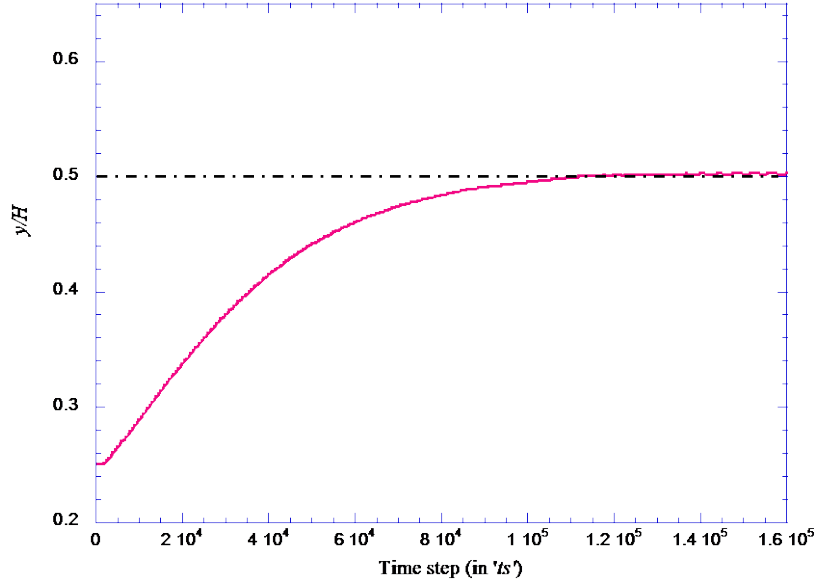
Figure 4-18: Lateral migration of the particle in the channel.

4.5   SETTLING OF THE PARTICLE IN A 2D CHANNEL UNDER GRAVITY

For further investigation of the dynamics of a particle-fluid system, the settling trajectories of a particle under gravity [79-81] at different Reynolds numbers are developed to validate the extension of the application of Ladd's boundary condition and force evaluation method. Figure 4-19 shows the parameters of the simulation test.

Locating the initial position of the cylinder at $Y_0 = 1.6a$, all of the simulation parameters can be chosen following the unit transformations in Table 4-3. The Reynolds number used in the simulation tests is defined as: $Re = \frac{U_p d}{\nu}$ [81], where U_p is the final velocity of the cylinder and $d = 2a$ is the diameter of the cylinder. Different relaxation time parameters τ are chosen to simulate different kinematic viscosities ν for different Reynolds numbers.

54
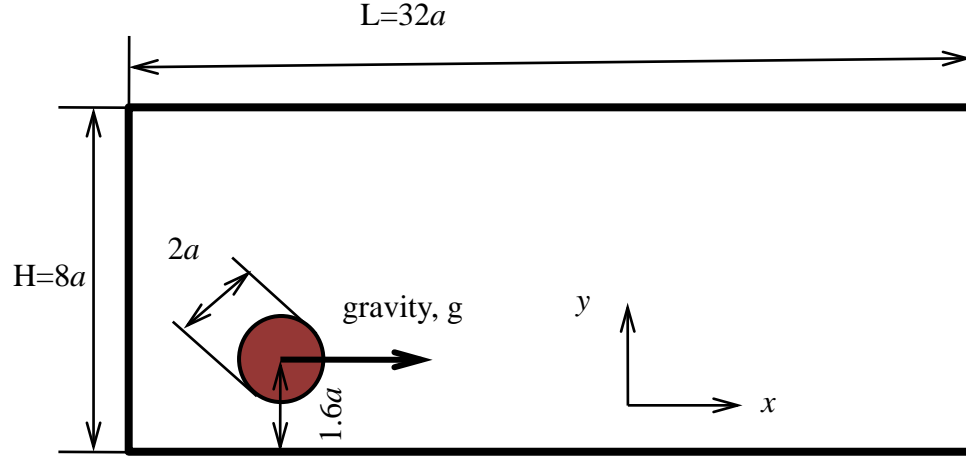
Figure 4-19: Sketch of the particle settling in a channel under gravity.

Six cases are investigated for the channel width $H = 8a$, and trajectories of the cylinder are presented in Figure 4-20. From the cylinder's trajectories presented in Figure 4-20, we can conclude that the centerline is the equilibrium state of the cylinder moving in the Poiseuille flow when the Reynolds numbers are moderate. For small Reynolds number flows ($0.1 < Re < 2$), the cylinder will move to the centerline of the channel in a monotonic trend due to the inertia. At larger Reynolds numbers ($3 < Re < 10$), the centerline is still an equilibrium position, but the cylinder experiences a damped oscillation before moving to the equilibrium position. Moreover, with an increasing Reynolds number, the cylinder needs a shorter x-direction distance to reach the equilibrium position [79].
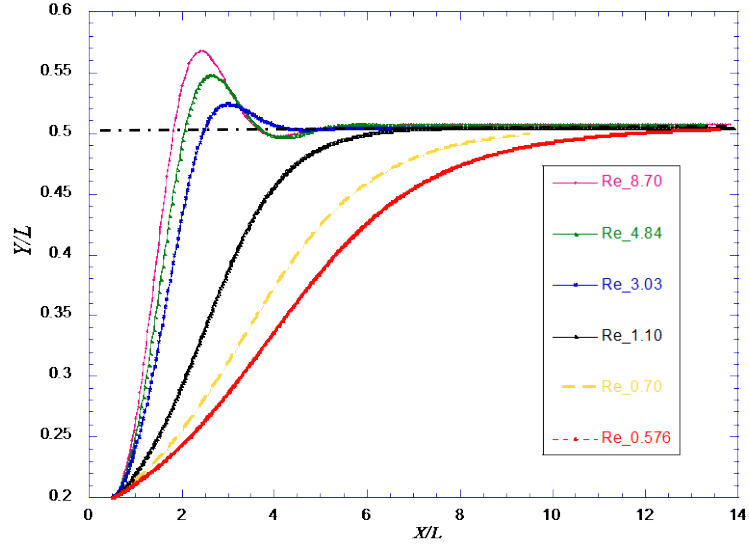
Figure 4-20: Trajectories of particles settling in the channel width $H = 8a$ at various Reynolds numbers.

Three cases are also investigated for the channel width $H = 3a$, and trajectories of the cylinder are presented in Figure 4-21. From Figure 4-21, we can conclude that the centerline of the channel is still the equilibrium position for the cylinder moving in a Poiseuille flow. With a decrease in the channel width, stronger oscillations can be observed compared to a wider channel width when the Reynolds numbers are the same due to the wall effects [79]. However, from Figure 4-21 and Figure 4-22 [79], we know that in the $H = 3a$ channel case, the cylinder needs to travel a longer distance to reach the equilibrium position with applying Ladd's boundary condition. Therefore, it appears that the geometric integrity cannot be preserved precisely by applying Ladd's boundary condition. Since this geometric integrity is of great importance for the microscopic investigation of the particle-fluid system, it is clear that further refinements are needed.
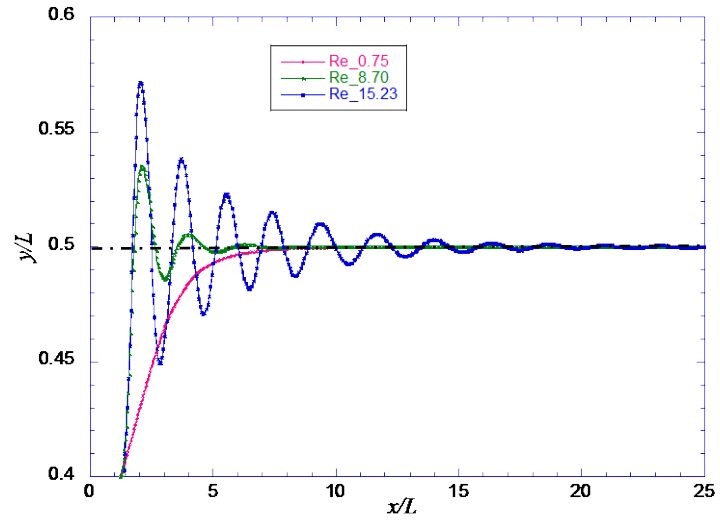
Figure 4-21: Trajectories of particles settling in the channel width $H = 3a$ at various Reynolds numbers (LBM with Ladd's boundary condition).
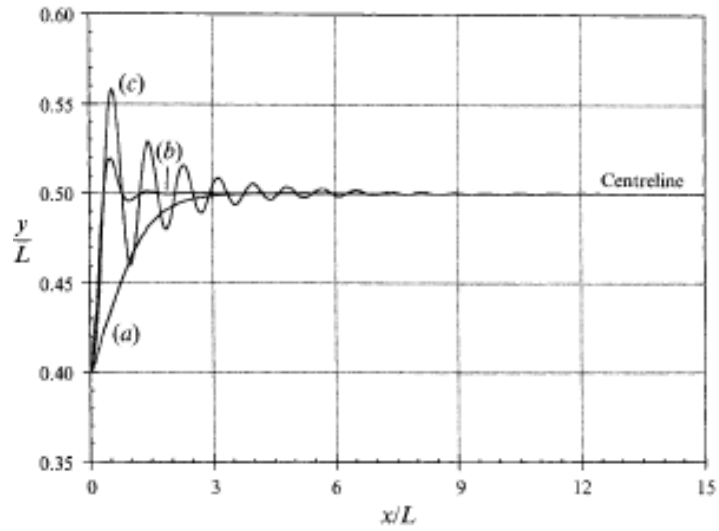
Figure 4-22: Trajectories of particles settling in the channel width $H = 3a$ at various Reynolds numbers, as presented in [79]: (a) $Re = 0.65$, (b) $Re = 3.23$, (c) $Re = 6.28$.

5.0   A NOVEL MOVING BOUNDARY CONDITION

Based on previous numerical experiments on the development of the fluid-particle model, the FH boundary condition can accurately capture the location of the actual boundary of the complex surface, while Ladd's boundary condition can give good results for the moving boundary with some compromising of the geometric integrity. Thus, a more accurate boundary condition is still needed to preserve the geometrical integrity of a complex surface for fluid-particle flow.

5.1   THE THEORETICAL FOUNDATION AND MATHEMATICAL DERIVATION OF THE NEW MOVING BOUNDARY CONDITION

A novel boundary condition, which can capture the actual surface of the moving boundary precisely, is constructed based on the Chapman-Enskog expansion [51]. For the sake of simplicity, the map of the boundary wall and lattice nodes is illustrated in Figure 5-1 for a two dimensional flat surface located in the Cartesian lattice space. In the lattice space, $\delta x = \delta y = 1$. The moving surface is located at x_{wall}, which is between the solid nodes x_s and the fluid nodes x_f, with a velocity u_{wall}.

The parameter $\Delta = \frac{x_f - x_{wall}}{x_f - x_s}$ is defined [32] to describe the fraction of an intersected link in the fluid region, where $0 \leq \Delta \leq 1$. Suppose the particle momentum moving from x_f to x_s is e_i

and the reversed momentum from x_s to x_f is $e_{-i} = -e_i$. After the collision process, $f_i^+(x_f)$ at the fluid region is known, but $f_i^+(x_s, t)$ from the solid nodes is unknown to us. To finish the streaming process:

$$f_{-i}(x_f = x_s + e_{-i}\delta t, t + \delta t) = f_{-i}^+(x_s, t) \qquad 5.1$$

It is obvious that $f_{-i}^+(x_s, t)$ is unknown to us due to the impermeability of the solid boundary wall. Thus, our task becomes to construct $f_{-i}(x_f, t + \delta t)$.
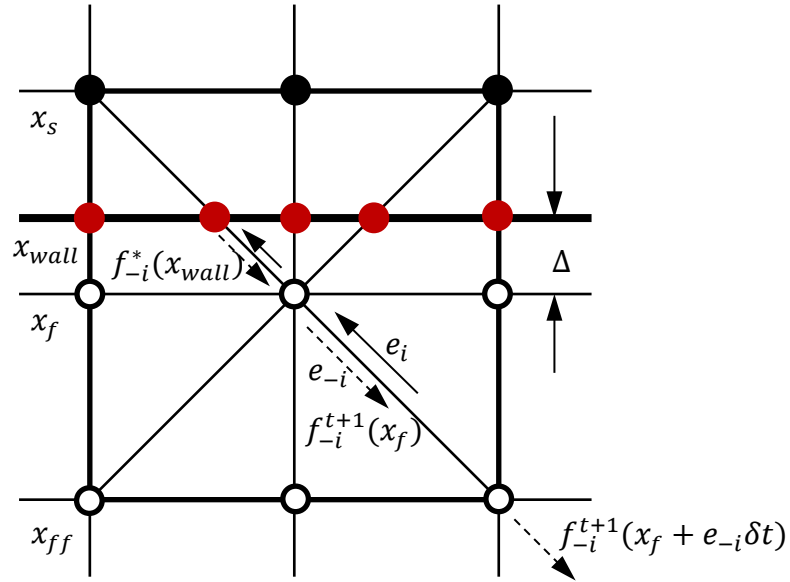
Figure 5-1: Layout of a flat surface mapped on the regular lattices in 2-D space. The open circles denote the fluid nodes. The black solid circles denote the solid nodes with connections to the fluid nodes. The red solid circles denote the boundary nodes between the solid nodes and fluid nodes.

In the FH boundary scheme, this unknown PDF was constructed based on the linear interpolation of the known PDF at neighboring lattice node, a fictitious equilibrium PDF and a momentum term [32], while a modified FH boundary scheme was developed to avoid the instability caused by the existence of $(\tau - 1)$ as the denominator in the FH boundary scheme

[32, 64]. However, a more accurate and stable boundary treatment is still needed to eliminate the approximations, and to capture the exact boundaries for solid-fluid flows.

In this section, the theoretical foundation of the unknown PDF is based on the Chapman-Enskog expansion as introduced in [12, 51]. The PDFs at all of the lattice nodes after one time step δt can be expressed as:

$$f_i(x + \xi_i \Delta t, t + \Delta t) = \sum_{n=0}^{\infty} \frac{\epsilon^n}{n!} D_t^n f_i(x, t) \qquad 5.2$$

$$f_i(x, t) = \sum_{n=0}^{\infty} \epsilon^n f_i^{(n)}(x, t) \qquad 5.3$$

where the Knudsen number $\epsilon = \delta t = 1.0$, $D_t = (\partial_t + e_i \cdot \nabla)$, and $\partial_t = \sum_{n=0}^{\infty} \epsilon^n \partial t_n$.

We can rewrite the discretized lattice Boltzman-BGK equation as shown in equation 2.9 in the following expression:

$$f_i(x + \xi_i \Delta t, t + \Delta t) - f_i(x, t) = -\frac{1}{\tau} \left[f_i(x, t) - f_i^{eq}(x, t) \right] \qquad 5.4$$

Substituting the expansions of $f_i(x + \xi_i \Delta t, t + \Delta t)$ and $f_i(x, t)$ as shown in 5.2 and 5.3 into the lattice Boltzmann-BGK equation 5.4, we can obtain:

$$\left[\frac{\epsilon^0}{0!} D_t^0 f_i(x, t) + \frac{\epsilon^1}{1!} D_t^0 f_i(x, t) + \frac{\epsilon^2}{2!} D_t^0 f_i(x, t) + \sum_{n=2}^{\infty} \frac{\epsilon^n}{n!} D_t^n f_i(x, t) \right] - f_i(x, t)$$

$$5.5$$

$$= -\frac{1}{\tau} \left[\epsilon^0 f_i^{(0)}(x, t) + \epsilon^1 f_i^{(1)}(x, t) + \epsilon^2 f_i^{(2)}(x, t) + \sum_{n=2}^{\infty} \epsilon^n f_i^{(n)}(x, t) - f_i^{eq}(x, t) \right]$$

Based on the expansion of the operator of $\partial_t = \sum_{n=0}^{\infty} \epsilon^n \partial t_n$ and $D_t = (\partial_t + e_i \cdot \nabla)$, we have:

$$\left[1 + \epsilon(\partial t_0 + \epsilon^1 \partial t_1 + \epsilon^2 \partial t_2 + e_i \cdot \nabla) f_i(x, t) + \frac{\epsilon^2}{2} (\partial t_0 + e_i \cdot \nabla)^2 f_i(x, t) \right] - f_i(x, t)$$

$$5.6$$

$$= -\frac{1}{\tau} \left[\epsilon^0 f_i^{(0)}(x, t) + \epsilon^1 f_i^{(1)}(x, t) + \epsilon^2 f_i^{(2)}(x, t) - f_i^{eq}(x, t) \right] + O(\epsilon^3)$$

60

Then, we can derive the following equation after substituting the expansion of $f_i(x, t)$ into 5.6:

$$\left[\epsilon(\partial t_0 + \epsilon^1 \partial t_1 + \epsilon^2 \partial t_2 + e_i \cdot \nabla)\left(\epsilon^0 f_i^{(0)}(x,t) + \epsilon^1 f_i^{(1)}(x,t) + \epsilon^2 f_i^{(2)}(x,t)\right)\right.$$
$$\left. + \frac{\epsilon^2}{2}(\partial t_0 + e_i \cdot \nabla)^2 \left(\epsilon^0 f_i^{(0)}(x,t) + \epsilon^1 f_i^{(1)}(x,t) + \epsilon^2 f_i^{(2)}(x,t)\right)\right] \qquad 5.7$$
$$= -\frac{1}{\tau}\left[\epsilon^0 f_i^{(0)}(x,t) + \epsilon^1 f_i^{(1)}(x,t) + \epsilon^2 f_i^{(2)}(x,t) - f_i^{eq}(x,t)\right] + \mathcal{O}(\epsilon^3).$$

Up to the order of $\mathcal{O}(\epsilon^0)$, collecting the terms of ϵ^0 on both sides of the equation 5.7, we have:

$$0 = -\frac{1}{\tau}\left[\epsilon^0 f_i^{(0)}(x,t) - f_i^{eq}(x,t)\right] \qquad 5.8$$

and the following expression can be obtained as shown in [51]:

$$\mathcal{O}(\epsilon^0): f_i^{(0)}(x,t) = f_i^{eq}(x,t) \qquad 5.9$$

Up to the order of $\mathcal{O}(\epsilon^1)$, collecting the terms of ϵ^1 on both sides of the equation 5.7:

$$\left[\epsilon(\partial t_0 + e_i \cdot \nabla)\left(\epsilon^0 f_i^{(0)}(x,t)\right)\right] = -\frac{1}{\tau}\left[\epsilon^0 f_i^{(0)}(x,t) + \epsilon^1 f_i^{(1)}(x,t) - f_i^{eq}(x,t)\right] \qquad 5.10$$

Then, rearranging and noting that $D_{t_0} = (\partial t_0 + e_i \cdot \nabla)$, we have:

$$\mathcal{O}(\epsilon^1): D_{t_0} f_i^{(0)}(x,t) = -\frac{1}{\tau} f_i^{(1)}(x,t) \qquad 5.11$$

Next, going up to the order of $\mathcal{O}(\epsilon^2)$, collecting all the terms of ϵ^2 on both sides of the equation 5.7:

$$\left[\epsilon^2(\partial t_0 + e_i \cdot \nabla)f_i^{(1)}(x,t) + \epsilon^2 \partial t_1 f_i^{(0)}(x,t) + \frac{\epsilon^2}{2}(\partial t_0 + e_i \cdot \nabla)^2\left(f_i^{(0)}(x,t)\right)\right] \qquad 5.12$$
$$= -\frac{1}{\tau}\left[\epsilon^2 f_i^{(2)}(x,t)\right] + \mathcal{O}(\epsilon^3)$$

Remembering that $\epsilon = 1$, and $D_{t_0} f_i^{(0)}(x,t) = -\frac{1}{\tau} f_i^{(1)}(x,t)$, produces the following equation:

$$\left[(\partial t_0 + e_i \cdot \nabla)f_i^{(1)}(x,t) + \partial t_1 f_i^{(0)}(x,t) - \frac{1}{2\tau}(\partial t_0 + e_i \cdot \nabla)\left(f_i^{(1)}(x,t)\right)\right] \qquad 5.13$$
$$= -\frac{1}{\tau}\left[\epsilon^2 f_i^{(2)}(x,t)\right] + \mathcal{O}(\epsilon^3)$$

61

Thus, the equation up to the order of ϵ^2 can be obtained as:

$$\mathcal{O}(\epsilon^2){:}\partial_{t_1} f_i^{(0)} + \left(\tfrac{2\tau-1}{2\tau}\right) D_{t_0} f_i^{(1)} = -\tfrac{1}{\tau} f_i^{(2)} \qquad 5.14$$

Finally, up to the order of $\mathcal{O}(\epsilon^3)$, all the PDFs on the lattice nodes can be expressed as:

$$f_i(x,t) = \sum_{n=0}^{\infty} \epsilon^n f_i^{(n)} = f_i^{(0)} + \epsilon f_i^{(1)} + \epsilon^2 f_i^{(2)} + \mathcal{O}(\epsilon^3). \qquad 5.15$$

Based on the above derivation, we can propose to construct the fictitious PDFs at the boundary nodes located at x_{wall} after the collision process like all the lattice nodes mapped on the Cartesian coordinates as:

$$f_i^*(x_{wall}) = f_i^{(0)} + f_i^{(1)} + \mathcal{O}(\epsilon^2), \qquad 5.16$$

where $f_i^{(0)}$ is the PDF at the equilibrium state. From equation 5.11, we know that $f_i^{(1)} = -\tau D_{t_0} f_i^{(0)}$, and thus the fictitious PDFs at the boundary surface can be obtained through equations 5.9, 5.11, and 5.16 as:

$$f_i^*(x_{wall}) = f_i^{(0)} - \tau D_{t_0} f_i^{(0)} = f_i^{(0)} - \tau(\partial_t + e_i \cdot \nabla)\, f_i^{(0)}, \qquad 5.17$$

and the equilibrium PDF at the boundary wall $f_i^{(0)}$ can be obtained by equation 2.10:

$$f_i^{(0)}(x_{wall},\, t) = \rho\omega_i \left[1 + \tfrac{3}{c_s^2}(e_i \cdot u_w) + \tfrac{9}{2c_s^4}(e_i \cdot u_w)^2 - \tfrac{3}{2c_s^2} u_w \cdot u_w \right]. \qquad 5.18$$

When at the equilibrium state, we know that $\partial_t f_i^{(0)} = 0$; thus, the fictitious PDFs at the wall boundary nodes can be expressed as:

$$f_i^*(x_{wall}) = f_i^{(0)} - \tau D_{t_0} f_i^{(0)} = f_i^{(0)} - \tau(e_i \cdot \nabla) f_i^{(0)}, \qquad 5.19$$

where the first term can be obtained by equation 5.18 and the second term can be solved by space discretization schemes.

With it known that the fictitious PDFs at the boundary nodes lie exactly at the wall, the unknown PDFs at the fluid nodes attached to the boundary nodes can be obtained by linear or quadratic interpolations. The linear and quadratic interpolations can be obtained as:

$$f_{-i}(x_f, t + \delta t) = \frac{1}{(1+\Delta)} f_{-i}^*(x_{wall}) + \frac{\Delta}{(1+\Delta)} f_{-i}^+(x_f, t), \qquad 5.20$$

$$f_{-i}(x_f, t + \delta t) = \frac{2}{(2+\Delta)(1+\Delta)} f_{-i}^*(x_{wall}) + \frac{2\Delta}{(1+\Delta)} f_{-i}^+(x_f, t) - \frac{\Delta}{(2+\Delta)} f_{-i}^+(x_{ff}, t). \qquad 5.21$$

Because the location of the lattice nodes x_f in Figure 5-1 in the fluid region always lie between the x_{wall} and x_{ff}, thus, the PDFs at the fluid nodes x_f attached to the boundary wall can always be obtained by an interpolation scheme based on the known PDFs at x_{wall} and x_{ff}. Moreover, all of the denominators in the above interpolation scheme are absolutely positive, and thus, this boundary scheme can be applied without considering the values of the intersection fraction Δ, where as in other boundary schemes, divisions are necessary in the application of the intersection fraction, for example for $0 \leq \Delta < 1/2$ and $1/2 \leq \Delta \leq 1$, respectively, in [31, 32, 64].

The most important idea in this new moving boundary condition is that the fictitious PDFs at the boundary nodes can be constructed based on the Chapman-Enskog expansion as all of the lattice nodes located in the Cartesian coordinates in the computational domain, which is the most important rigorous theoretical framework for the LBM. Rather than just simply substituting with equilibrium PDFs, a correction term $(-\tau D_{t_0} f_i^{(0)})$ in equation 5.19 is included when constructing the unknown PDF for the lattice nodes in the fluid region. The velocity u_w used for the calculation for the $f_i^{(0)}(x_{wall}, t)$ is exactly the velocity of the moving wall, which ensures the consistency of the location of the boundary wall and the velocity of the wall without approximation. Moreover, the unified linear or quadratic interpolation schemes, as shown in 5.20

and 5.21, make the new boundary condition much easier to be implemented without, again, separate consideration of the value of Δ as in [32, 63].

5.2 NUMERICAL EXPERIMENTS WITH THE NOVEL MOVING BOUNDARY CONDITION FOR FLAT BOUNDARIES

5.2.1 Couette flow

In order to validate the new moving boundary condition and test the accuracy of the proposed boundary scheme, the velocity profile of a Couette flow with two moving plates is studied, as shown in Figure 5-2, and the velocity profiles obtained by the new boundary scheme are compared with the results obtained in analytical solutions. For a Couette flow, the *x*-component velocity should be distributed as a linear relationship with the location of y. In this case, the channel width is $N_y - 1 + 2\Delta$ and the analytic solution of the Couette flow can be expressed as:

$$u_x(y) = \left(u_{top} - u_{bottom}\right) \frac{y - 1 + \Delta}{N_y - 1 + 2\Delta} + u_{bottom}. \qquad 5.22$$
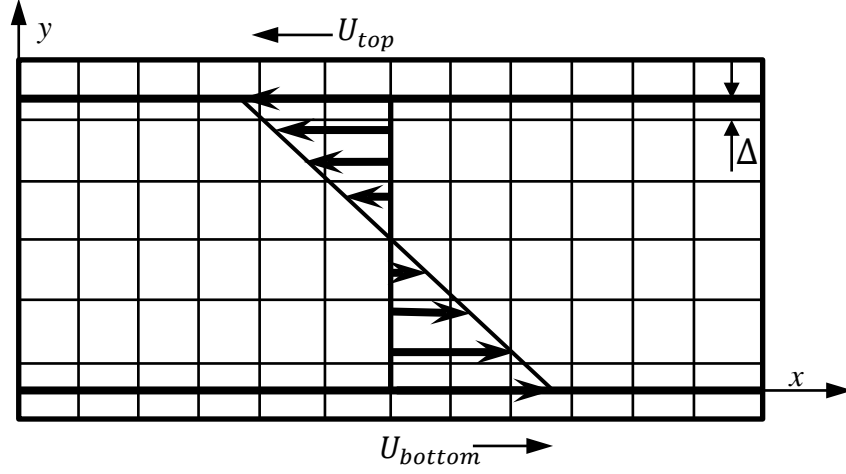
Figure 5-2: Velocity distribution of the Couette flow in a two-dimensional channel.

In the numerical tests, the spacing of the lattice nodes is set to be only $N_y = 20$ lattice units, the velocity of the top plate is $u_{top} = -1/40$ while the velocity of the bottom plate is $u_{bottom} = 1/40$, and the relaxation time parameter τ in the calculation is set to be 0.8. Equations 5.18, 5.19, and 5.20 are applied for the y-direction boundary condition and the periodic boundary condition is applied for the x-direction boundary condition, which is:

$$f_i(x = 1, t) = f_i(x = N_x - 1, t),$$ 5.23

$$f_i(x = N_x, t) = f_i(x = 2, t)$$ 5.24

In order to test the new boundary scheme's ability to capture the accurate location of the boundary wall, different values of the intersection fraction $\Delta = 0.1, 0.2, \dots, 0.9$ are chosen for the numerical tests. The initial density of the fluid ρ is set to be 1.0, and the velocities u at each lattice node are set to be zero for the calculation of the equilibrium f_i^{eq} as the initial condition. Based on the analytical solution, we know that by increasing the value of the intersection fraction Δ, the distance between the fluid nodes and the boundary nodes are also increasing, and thus the velocity of the fluid nodes attached to the boundary wall should be decreasing. Figure 5-3 (a) and

(b) show the velocity profiles obtained by the new boundary scheme and the analytic solution for

Δ= 0.1 and Δ= 0.8. From the velocity profiles shown in Figure 5-3, we can see the excellent

agreement
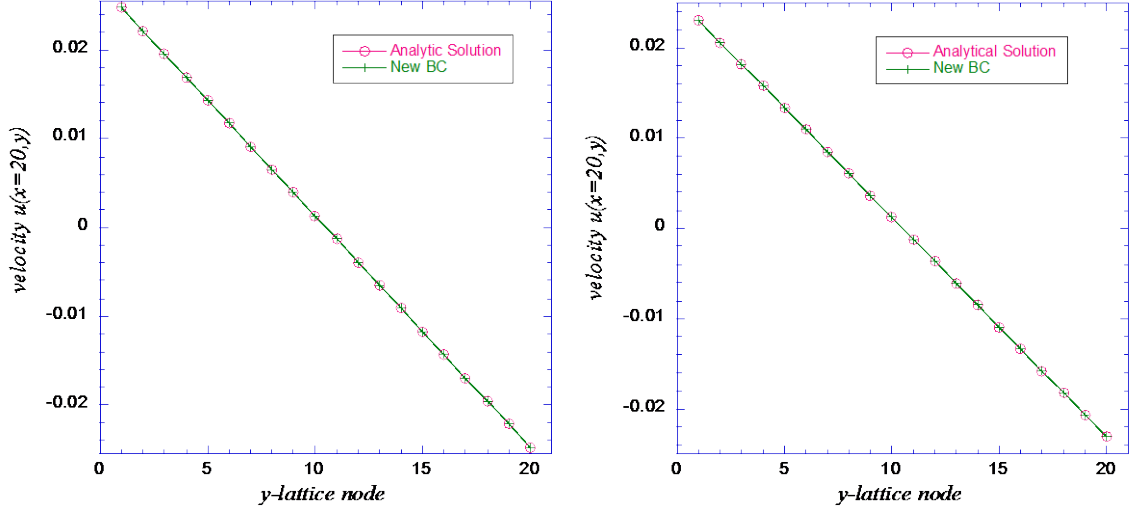
Figure 5-3: Velocity profiles of the Couette flow when intersection fraction is (a) Δ= 0.1 and

(b) Δ= 0.8.

between the results obtained by the analytical solution and the LBM with the new moving

boundary condition.

To further assess the computational accuracy of the LBM solution of the velocity of the

new boundary condition, the relative L_2- norm error, as defined in [32], is calculated for

comparison:

$$E_2 = \frac{\left\{\int_0^H [u_{analytic} - u_{LBM}]^2 dy\right\}^{1/2}}{\left\{\int_0^H u_{analytic}{}^2 dy\right\}^{1/2}}. \qquad 5.25$$

The global relative L_2-norm errors calculated for the new proposed moving boundary condition,

for Ladd's boundary condition [29], and for Mei et al.'s modification of the Filippova and Hänel

boundary condition for a curved moving boundary in [32, 64] are shown in Figure 5-4. For an intersection fraction $\Delta = 0.1 - 0.9$, the global relative errors of the new boundary scheme are always around the order of $10^{-13} - 10^{-14}$. On the other hand, from the global L_2-norm errors in Figure 5-4, the modified FH boundary conditions in [32, 64] exhibit as high of a level of accuracy as the new boundary condition only when $\Delta \geq 0.5$. When the intersection fraction Δ is less than 0.5, even with a separate boundary scheme, the errors are increased to the order of 10^{-2}, which is only a small improvement over Ladd's mid-link boundary condition. The differences between the two modified FH boundary condition schemes only include a few parameters adjustment for the interpolation scheme when $\Delta \geq 0.5$, and thus, the error results of the two modified FH schemes are almost the same.
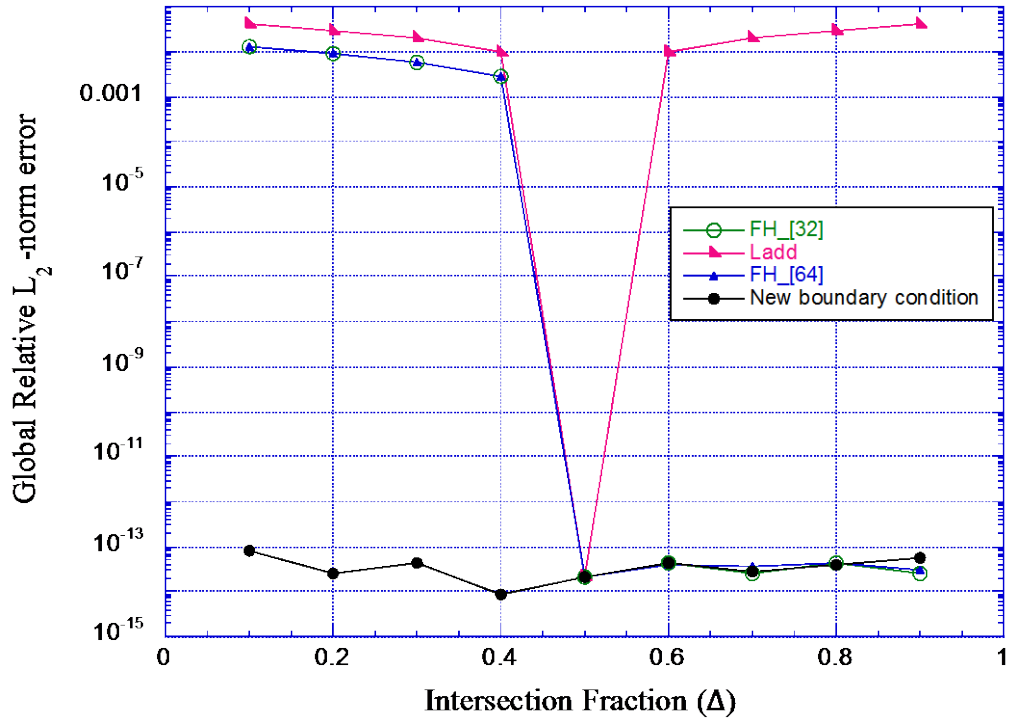
Figure 5-4: The global relative L_2-norm error for different intersection fraction values.

Moreover, for the same Couette tests described above, Ladd's mid-link based moving boundary condition will always locate the wall in the middle of the link connecting the fluid nodes and the wall nodes, where the intersection fractions Δ for all of the cases are 0.5, no matter the actual values of the intersection fraction. With the same values of Δ for all of the test cases, it is obvious that the velocity profiles obtained by Ladd's boundary scheme would be the same as when Δ is varying from 0.1 to 0.9. Thus, Ladd's moving boundary condition can only work well for Δ= 0.5. From the error comparison between the new moving boundary condition with the existing boundary conditions in Figure 5-4, we can see that the new moving boundary condition can capture the exact location of the moving surface, and thus the numerical accuracy of the LBM for simulating the moving surface can be highly improved.

5.2.2 Poiseuille flow

To further investigate the novel moving boundary condition, a Poiseuille flow is studied to validate the improvement of the numerical accuracy and stability with comparison to the analytical solution and the existing boundary conditions [32]. The simulation sketch is shown in Figure 5-5. We know that the pressure gradient applied to drive the channel flow can be treated as a body force, which can be incorporated into the PDFs [82] after the collision process. Thus, all of the PDFs after collision have the form of $f_i^+(x,t) = f_i^+(x,t) - \omega_i \frac{3}{c^2} \frac{dp}{dx} \vec{e_i} \cdot \vec{x}$.
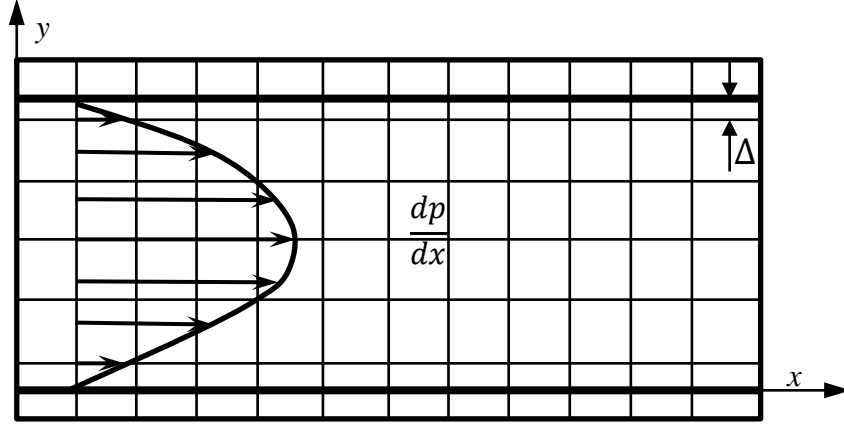
Figure 5-5: Fully developed Poiseuille flow in a 2-dimensional channel.

In the Poiseuille flow test, the relaxation parameter τ is chosen to be 0.8, and the other parameters are listed in Table 5-1. In order to validate the numerical accuracy of the new boundary condition, tests for intersection fractions of $\Delta=$ 0.1, 0.3, 0.5, and 0.8 are carried out. For each case, the actual channel width is $H_{lb} = 11 + 2\Delta$. It is known that the analytical solution for a Poiseuille flow is $u_x = \frac{-g_x}{2v_p}(y^2 - yH)$, and thus, the velocity profiles obtained by the LBM and the analytical solution, which are normalized by $u_{x\_max} = u_x\left(y = \frac{H}{2}\right)$ and presented in Figure 5-6, can be compared and then used to validate the new boundary condition's numerical accuracy.

Table 5-1: Unit transformations for a Poiseuille flow.

Physical system	Lattice Boltzmann system
Width: $H = 1.1 \times 10^{-4} \ (m)$,	$Y = 11 \ lu$, $$\Delta x = \Delta y = 1(lu) = \frac{H}{Y}(m) = 1 \times 10^{-5}(m),$$
Water's kinetic viscosity: $v_p = 10^{-6}(m^2/s)$,	$v_{lb} = \frac{2\tau - 1}{6} = \frac{2 \times 0.8 - 1}{6} = v_p \times \frac{\Delta t}{(\Delta x)^2}$, since Δx is known, we can calculate $\Delta t = 1.0 \times 10^{-5}s$,
Water's density : $\rho = 1 \times 10^3 (kg/m^3)$,	$\rho_{lb} = 1.0$,
Gravity: $g_x = 9.8(m/s^2)$,	$\frac{dp}{dx} = g_x \times \frac{(\Delta t)^3}{\Delta x} = 9.8 \times 10^{-5}$.
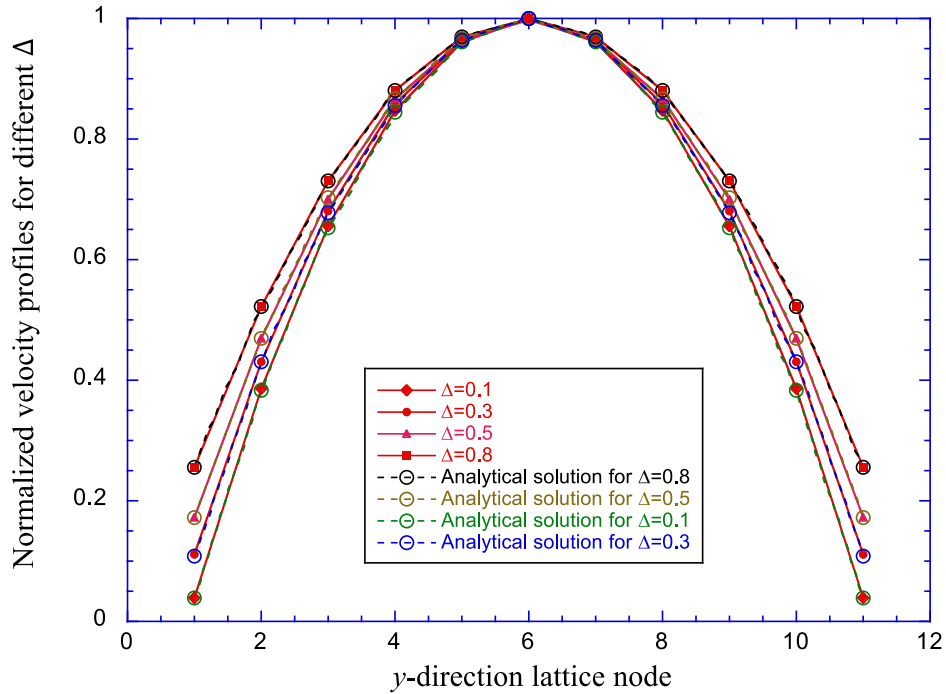
Figure 5-6: Velocity profiles of a Poiseuille flow when the intersection fraction Δ= 0.1, 0.3, 0.5, and 0.8.

From Figure 5-6, we can see perfect agreement between the velocity profiles simulated by LBM with the new boundary condition and the analytical solution, with only 11 lattice nodes in the y direction. Thus the ability of the new boundary condition to capture the exact location of the boundaries is further validated.

In order to investigate the numerical stability of the new boundary condition, a chart is made to compare the stability behavior to the existing modified FH boundary condition. Simulation parameters are chosen to be the same as presented in [32] in order to compare the simulation results under the same flow conditions, where $\frac{dp}{dx} = -1.0 \times 10^{-6}$, $N_x = 65$, and $N_y = 35$. In order to produce the stability chart, the relaxation time τ varies from 0.5 to 2.0, and the intersection fraction Δ is varying from 0.1 to 0.9. Equations 5.18-5.20 are applied for the y-direction boundary condition and the periodic boundary condition, as presented in equations 5.23 and 5.24, is applied for the x-direction boundary condition.

By applying the new proposed boundary condition, the stability region chart of a fully developed Poiseuille flow is shown in Figure 5-7. From the stability region chart of the same simulation test presented by Mei et al. with the modified FH boundary condition in [32], by increasing the relaxation parameter τ from 0.5 to 2.0, there is always a region of instability when the intersection fraction Δ is less than 0.5, even with a separate boundary treatment. However, by applying the new boundary scheme, there are no instability regions when the intersection fraction is higher than 0.2 under the same calculation conditions. From the stability chart, we can see that Mei's boundary condition is more vulnerable to the intersection fraction Δ, and thus, the new proposed boundary condition exhibits better performance in capturing the exact boundaries.

With the expanded stability region for $\Delta \geq 0.2$ presented in Figure 5-7, we will have more freedom in choosing the relaxation parameter τ, which is directly related to the fluid viscosity

$v = \left(\tau - \frac{1}{2}\right) c_s^2 \delta t$, or the Reynolds number $Re = \frac{uD}{v}$, ensuring a broader application of the LBM

for the simulation of more complex fluid flows.
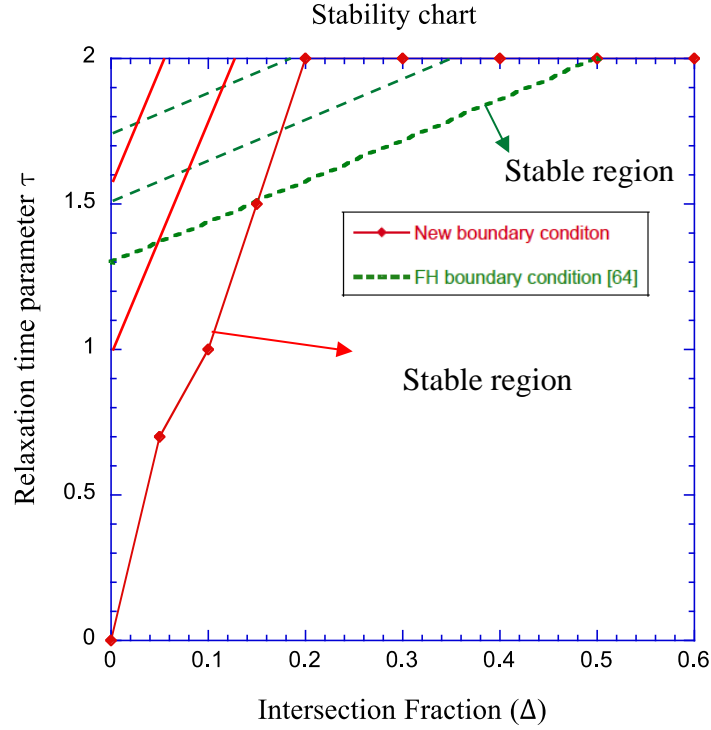
Stability chart

Figure 5-7: Stability region chart for a fully developed 2-D Poiseuille flow with the proposed boundary condition, compared to the modified FH boundary condition.

Based on the above two numerical experiments on the basic fluid flows, we can clearly see the highly improved numerical accuracy and stability by applying the new moving boundary condition. From the simulation results of the velocity profile, the results obtained by the new boundary condition can agree well with the analytical solution when the intersection fraction is varying, and show great capability to capture the actual wall boundary. From the relative error comparison, the new boundary condition shows great improvement over the most applied Ladd's boundary condition and FH boundary condition. Based on further investigation of the new

boundary condition on the flat boundaries, the stability chart of the Poiseuille flow is studied, based on which we can see the expansion of the stability region. In order to expand the application of the new moving boundary condition for the LBM algorithm, numerical tests on complex surfaces will be studied in the next sections.

5.3   NUMERICAL EXPERIMENTS WITH THE NOVEL MOVING BOUNDARY CONDITION FOR COMPLEX BOUNDARIES

In order to exhibit the capability of the new boundary condition to capture a complex surface, a uniform flow with velocity U_0 flowing over a column cylinder of radius a as shown in Figure 5-8 at a finite Reynolds number, which is defined by $Re = \frac{\rho U_0(2a)}{\mu} = \frac{U_0(2a)}{\nu}$, is investigated. The computational domain size is the same as introduced in Section 4.2, the transformations between the lattice system and real physical system follows the rules as shown in Table 4-1, and $Re = 10$.

One parameter that needs to be addressed is the number of iteration steps in each simulation experiment with varying relaxation time τ. For all of the cases of $Re = \frac{\rho U_0(2a)}{\mu} = \frac{U_0(2a)}{\nu} = 10$, where $\nu = \frac{2\tau-1}{6}$, we know that with the variation of the relaxation time τ, the viscosity ν in the lattice Boltzmann system will change as well.
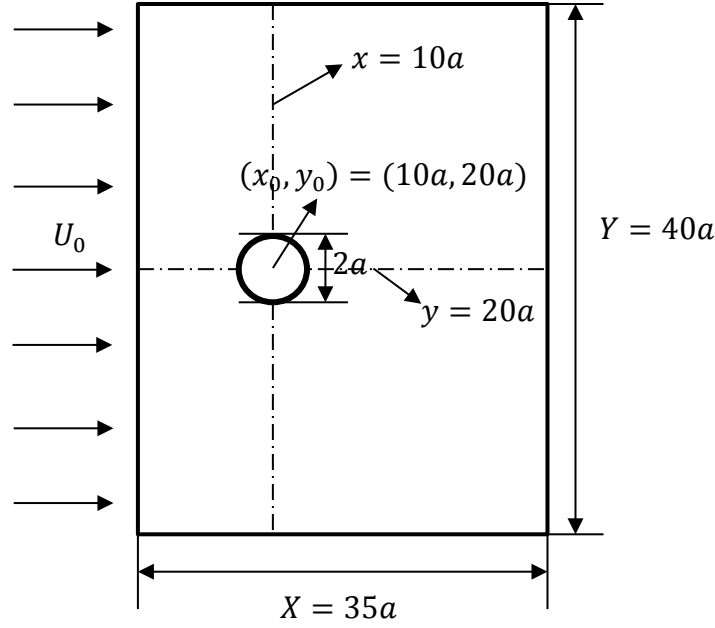
Figure 5-8: Sketch of the flow over a static 2D cylinder.

From the transformations between the lattice Boltzmann system and the physical system, we know that:

$$\nu_{lb} = \nu_p \times \frac{\Delta t}{(\Delta x)^2},$$ 5.26

Rewriting the above relation in a more straightforward way:

$$\Delta t = \frac{(\Delta x)^2}{\nu_p} \cdot \frac{2\tau - 1}{6}.$$ 5.27

Thus, in order to maintain the consistency of the viscosity of water between the lattice Boltzmann system (ν_{lb}) and the physical system (ν_p), the time step Δt needs to be modified once the relaxation time changes. In all of these cases for $Re = 10$, the time steps in the lattice Boltzmann system and number of iteration steps are listed in Table 5-2 for different relaxation time parameters τ.

Table 5-2: Time step Δt and total iteration steps N with varying τ.

Time relaxation time τ	Time step Δt $\Delta t = \dfrac{(\Delta x)^2}{v_p} \cdot \dfrac{2\tau - 1}{6}$	Total time steps for calculation N $N = \dfrac{2.0}{\Delta t}$
$\tau = 0.505$	$\Delta t = 1.667 \times 10^{-5}$	$N = 1.2 \times 10^5$
$\tau = 0.55$	$\Delta t = 1.667 \times 10^{-4}$	$N = 1.2 \times 10^4$
$\tau = 0.60$	$\Delta t = 3.333 \times 10^{-4}$	$N = 6.0 \times 10^3$
$\tau = 0.65$	$\Delta t = 5.000 \times 10^{-4}$	$N = 4.0 \times 10^3$
$\tau = 0.70$	$\Delta t = 6.667 \times 10^{-4}$	$N = 3.0 \times 10^3$
$\tau = 0.75$	$\Delta t = 8.333 \times 10^{-4}$	$N = 2.4 \times 10^3$
$\tau = 0.80$	$\Delta t = 1.000 \times 10^{-3}$	$N = 2.0 \times 10^3$

To validate the accuracy of the new moving boundary condition, a series of numerical tests under the same Reynolds number $Re = 10$ are carried out for relaxation parameter values shown in Table 5-2. After the same flow time $t = 2.0$ seconds, the normalized velocity profiles u/U_0 along the x-direction centerline ($y = 20a$) are shown in Figure 5-9 and the normalized velocity profiles u/U_0 along the y-direction centerline ($x = 10a$) are shown in Figure 5-10. Under the same Reynolds number, which can be used to help predict similar flow patterns for different fluid flow situations, we know that the flow pattern should be the same; thus, the velocity profiles for different relaxation parameter tests should also be the same. From the normalized upstream and downstream velocity profiles for different relaxation parameters in Figure 5-9, the velocity profiles
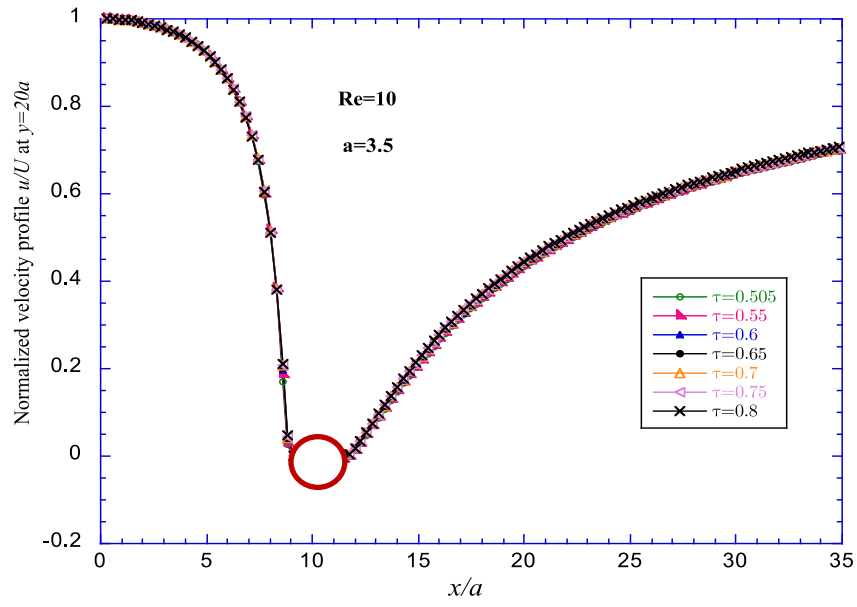
Figure 5-9: The upstream and downstream velocity profiles along the x-direction centerline $y = 20a$.
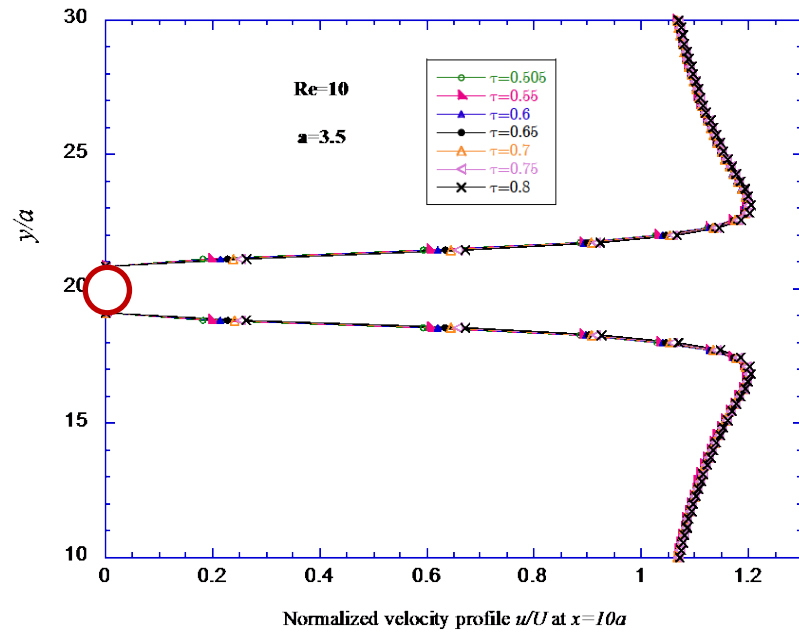
Figure 5-10: The normalized velocity profiles along the y-direction centerline $x = 10a$.

76

are identical for all of the studied tests. Similarly, the velocity profiles along the y-direction centerline for all of the studied cases are also in prefect agreement with each other, as can be seen from Figure 5-10. Thus, based on the results shown in Figure 5-9 and Figure 5-10 for the same Reynolds number flow, we can see that the new moving boundary condition works well for complex surfaces and shows numerical stability for different relaxation parameters.

To exhibit the capability of the new moving boundary condition to preserve the geometric integrity, a series of computational tests are carried out for a cylinder of radius $r = 3.0, 3.2, 3.4, 3.5, 3.6, 3.8$, and $r = 4.0$. In all of these tests, the Reynolds number is still set to 10, and the relaxation parameter is chosen to be $\tau = 0.505$. The results for the tests are shown in Figure 5-11 to Figure 5-15. For the same Reynolds number flow, with a different cylinder radius for each of the numerical tests, the flow patterns for all of the tests should be the same. Thus, the velocity profile with normalization to the cylinder radius r for each of the test should also be the same. In Figure 5-11, the normalized velocity profiles along the x-direction centerline $y = 20a$ for different cylinder radii $r = 3.0, 3.2, 3.4, 3.5, 3.6, 3.8$, and $r = 4.0$ are presented. In that figure, we can see strong agreement among all of the normalized velocity profiles for the same Reynolds number flow. More details of the velocity profiles in the upstream and downstream region are presented in Figure 5-12 and Figure 5-13. Similarly, the normalized velocity profiles along the y-direction centerline $x = 10r$ for different cylinder radii $r = 3.0, 3.2, 3.4, 3.5, 3.6, 3.8$, and $r = 4.0$ are presented in Figure 5-14, where we can again see agreement among all of the normalized velocity profiles for the same Reynolds number flow. More details of the velocity profiles in the half symmetry domain are presented in Figure 5-15.

A group of comparison figures between the normalized velocity profiles along the x-direction centerline for $Re = 10$ and $Re = 40$ are presented from Figure 5-16 to Figure 5-18.

77
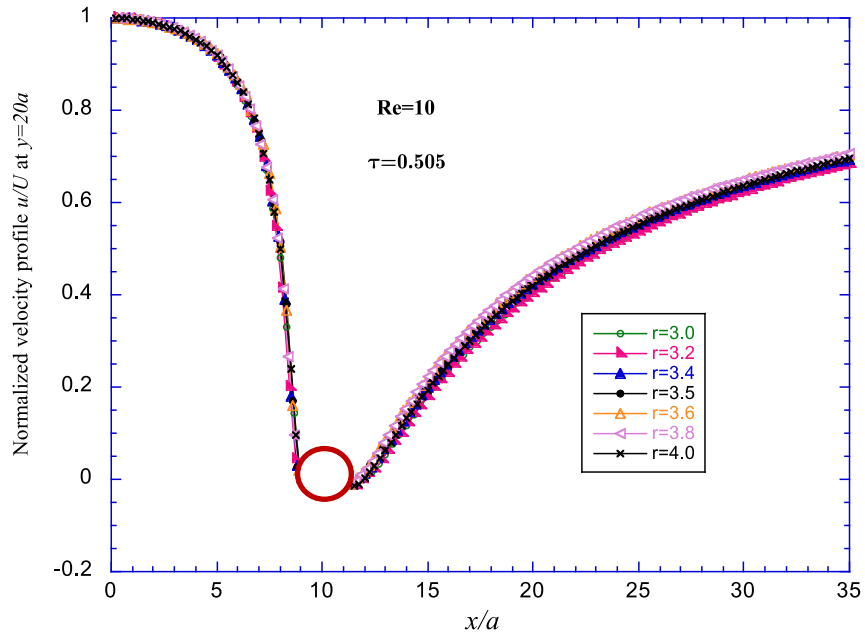
Figure 5-11: Normalized velocity profiles along the x-direction centerline $y = 20a$ for different cylinder radii for Reynolds number $Re = 10$.
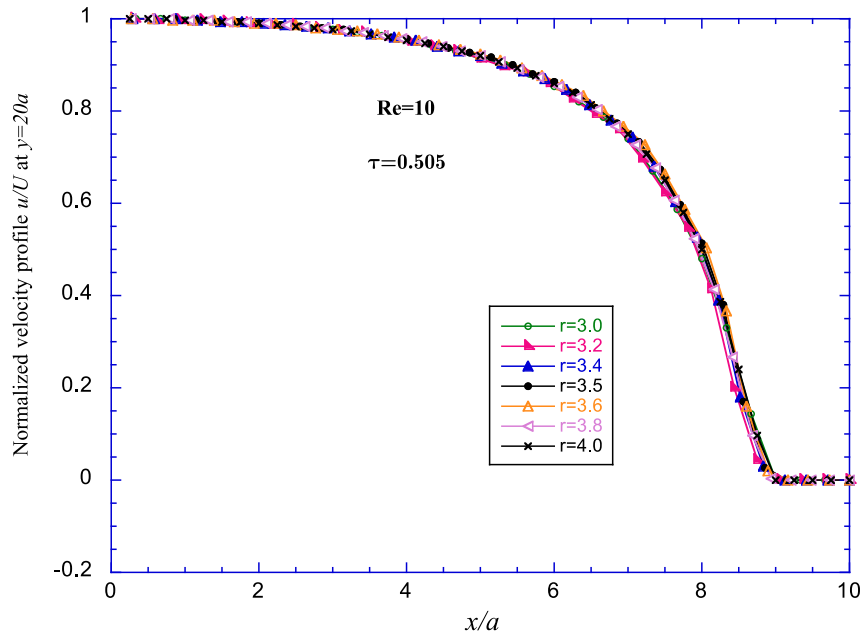
Figure 5-12: Normalized upstream velocity profiles along the x-direction centerline $y = 20a$ for different cylinder radii for Reynolds number $Re = 10$.
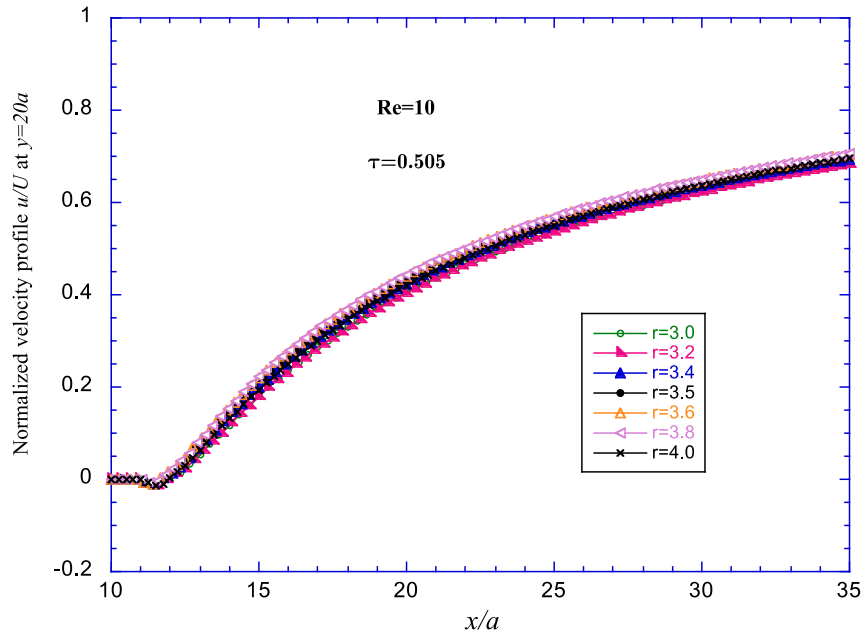
Figure 5-13: Normalized downstream velocity profiles along the x-direction centerline $y = 20a$ for different cylinder radii for Reynolds number $Re = 10$.
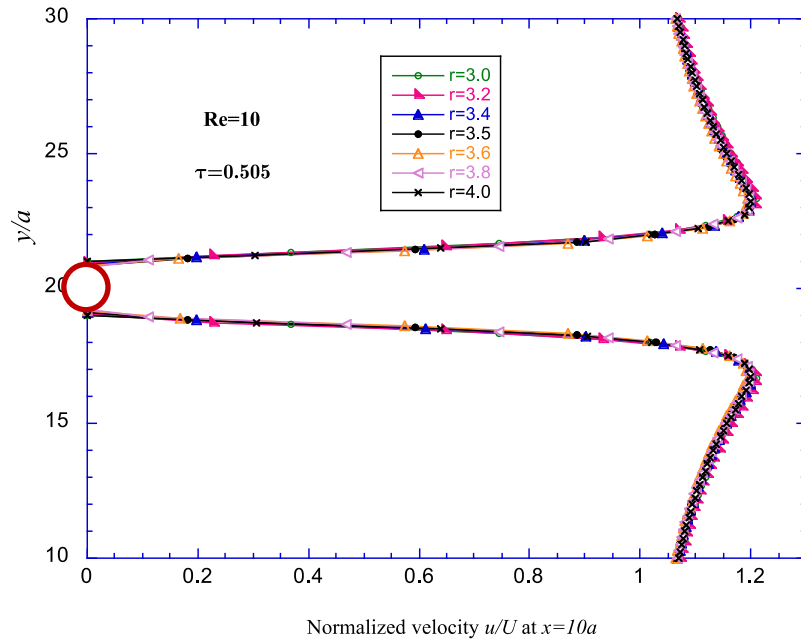
Figure 5-14: Normalized velocity profiles along the y-direction centerline $x = 10a$ for different cylinder radii for Reynolds number $Re = 10$.
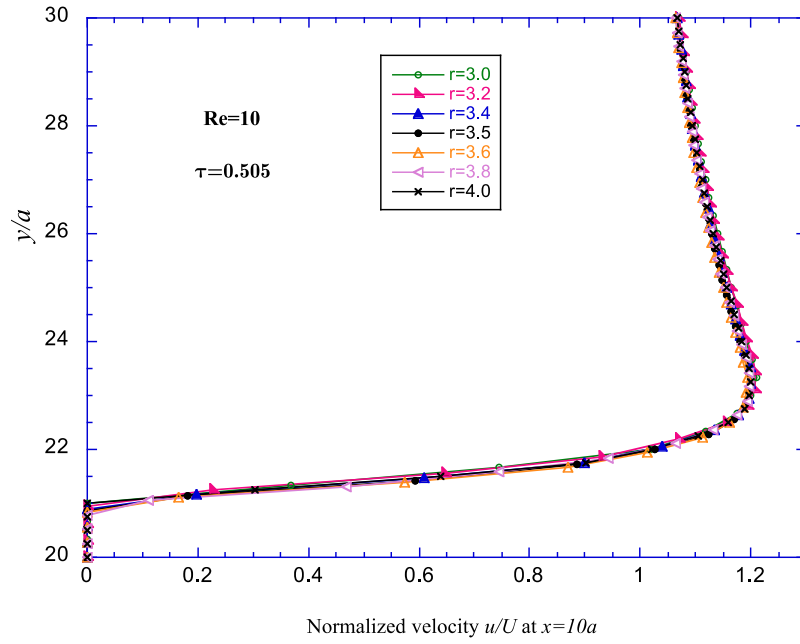
Figure 5-15: Normalized velocity profiles along the y-direction centerline $x = 10a$ for different cylinder radii for Reynolds number $Re = 10$.
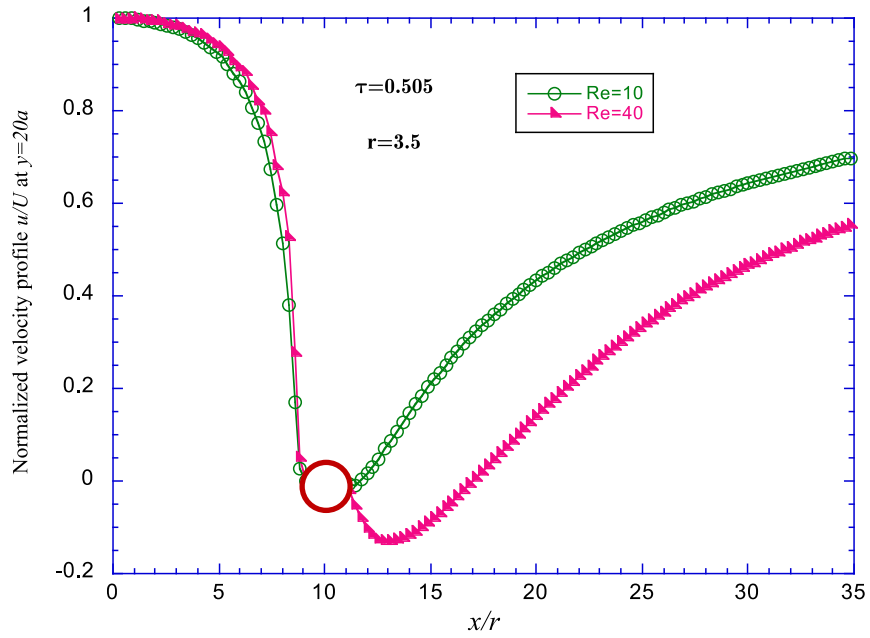
Figure 5-16: Normalized velocity profiles along the x-direction centerline $x = 20a$ for $Re = 10$ and $Re = 40$.
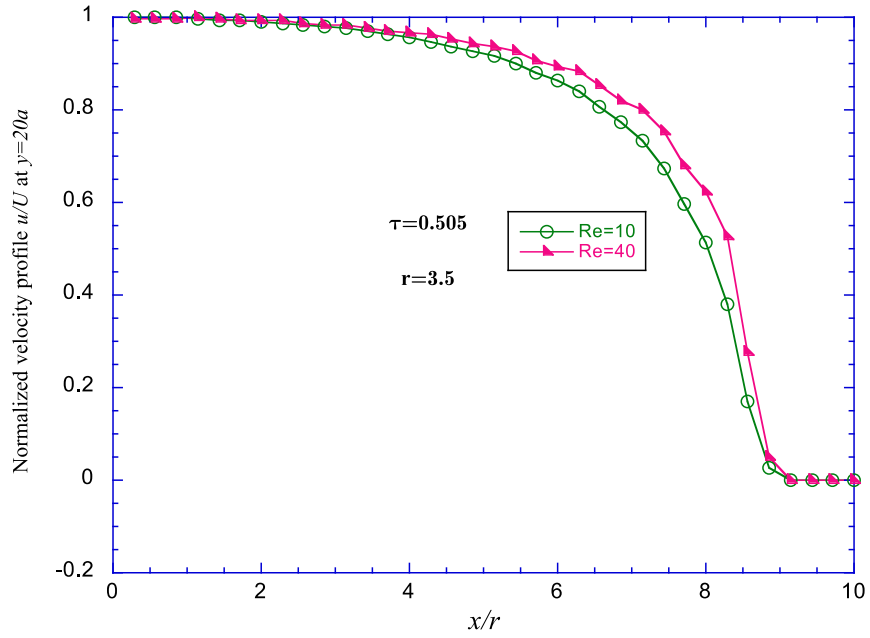
Figure 5-17: Upstream normalized velocity profiles along the x-direction centerline $x = 20a$ for $Re = 10$ and $Re = 40$.
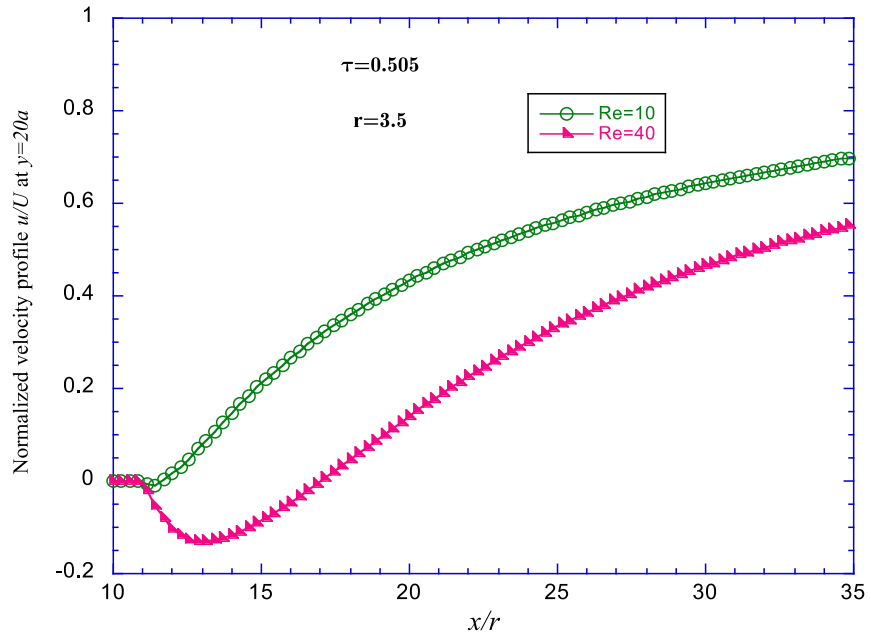
Figure 5-18: Downstream normalized velocity profiles along the x-direction centerline $x = 20a$ for $Re = 10$ and $Re = 40$.

81

We can see from Figure 5-16 and Figure 5-18 that there is a sharp gradient near the front stagnation point, which is because of the separation bubbles when $Re = 40$. Moreover, from Figure 5-18, we can see the maximum of the bubble velocity is around -0.15 and the separation bubble length is $x/r \approx 5.0$. The same results can be found by applying the modified FH boundary condition for the same simulation tests in [32].

Form the investigation on the velocity profiles under the same Reynolds number Re with different relaxation parameters τ and cylinder radii r, the numerical stability and capability to capture the exact boundary surfaces of the new moving boundary condition can be validated. It is known that for the same Reynolds number flows, the flow patterns should be the same. From Figure 5-9 and Figure 5-10, great agreement for all of the velocity profiles for different relaxation parameters τ can be seen, which means the flow patterns for all of the tests of $Re = 10$ are the same, and thus, and the numerical accuracy of the new moving boundary condition can be validated. Moreover, based on the agreement for all of the normalized velocity profiles for different cylinder radii from Figure 5-11 to Figure 5-15, we can conclude that the exact locations of the cylinder's surfaces are identified, and thus, the new moving boundary condition's capability to preserve the boundaries' geometric integrity can be validated. Moreover, the new moving boundary condition is easy to be implemented with a unified interpolation boundary scheme, without additional consideration for the intersection fraction Δ.

5.4 FORCE EVALUATION FOR A CYLINDER WITH THE NOVEL MOVING BOUNDARY CONDITION

To further develop the numerical model of a particle-fluid system, the force exerted on an asymmetrically placed cylinder is inspected in this section with the new moving boundary condition. The sketch of the benchmark test is shown in Figure 4-9. After the unit transformations, all of the simulation parameters are listed in Table 5-3. From Table 4-2 and Table 5-3, we can see the resolution of the numerical test in this section is $\Delta x = 1 \times 10^{-2}$, which is twice as coarse as the resolution for the test with FH modified boundary condition.

Numerical results for the unsteady flow at $Re = 100$ are presented from Figure 5-19 to Figure 5-23. The non-dimensional drag coefficient, lift coefficient, and Strouhal number are presented as results to compare with the results in [31, 76, 83, 84], and are defined as:

$$C_D = \frac{|F_x|}{\rho \bar{U}^2 a},$$

5.28

$$C_L = \frac{F_y}{\rho \bar{U}^2 a},$$

5.29

$$St = \frac{2a}{\bar{U}T},$$

5.30

where F_x and F_y can be obtained by the momentum exchange method in equations 3.30 and 3.31, as introduced in Section 3.5.

83

Table 5-3: Unit transformations for force validation.

Physical system	Lattice Boltzmann system
Length: $L = 2.2\ (m)$, Width: $H = 0.41\ (m)$, Radius of the cylinder: $R = 0.05\ (m)$.	$X = 220\ lu$, $Y = 41\ lu$, $r = 5\ lu$, $\Delta x = \Delta y = 1(lu) = \frac{L}{X}(m) = 1 \times 10^{-2}(m)$,
Kinetic viscosity: $\nu_p = 10^{-3}(m^2/s)$,	$\nu_{lb} = \frac{2\tau - 1}{6} = \frac{2 \times 0.55 - 1}{6} = \nu_p \times \frac{\Delta t}{(\Delta x)^2}$, since Δx is known, we can calculate $\Delta t = 1.667 \times 10^{-1}s$,
Reynolds number: $Re = 100$,	$Re = \frac{\overline{U}D_{lb}}{\nu_{lb}} = \frac{\overline{U} \times 10}{\frac{2 \times 0.55 - 1}{6}} = 100$,
Velocity: $U_{max} = 1.5\ (\frac{m}{s})$, $U_{average} = \overline{U} = \frac{2}{3} \times U_{max} = 1.0\ (\frac{m}{s})$.	With the above expression for Reynolds number, the velocity can be obtained as: $\overline{U} = 1.667 \times 10^{-1}$.

When $Re = 100$, the flow will become unsteady and periodic vortex shedding will be observed at the downstream region of the cylinder. Results for C_D, C_L, and St in the references are listed in Table 5-4.

Table 5-4: Numerical results for the drag coefficient, lift coefficient, and Strouhal number for the

unsteady flow when $Re = 100$.

$Re = 100$	$C_{D\,max} = \dfrac{|F_x|}{\rho \bar{U}^2 a}$	$C_{L\,max} = \dfrac{F_y}{\rho \bar{U}^2 a}$	$St = \dfrac{2a}{\bar{\bar{U}}T}$
The new moving BC	3.2964	1.0124	0.2970
Schäfer, M., et al. [76]	[3.22, 3.24]	[0.99, 1.01]	[0.2950, 0.3050]
Mei, R. et al. [64]	3.2358	1.0045	0.3033
Chang, C. et al. [84]	3.292	0.974	0.302
Chen, D. et al. [83]	3.333	1.0511	0.3003
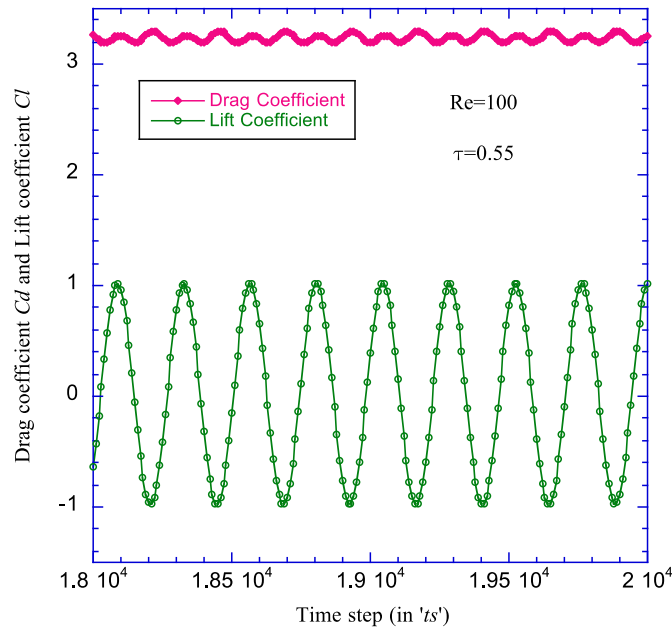
Figure 5-19: The variation of the drag and lift coefficients for $Re = 100$.
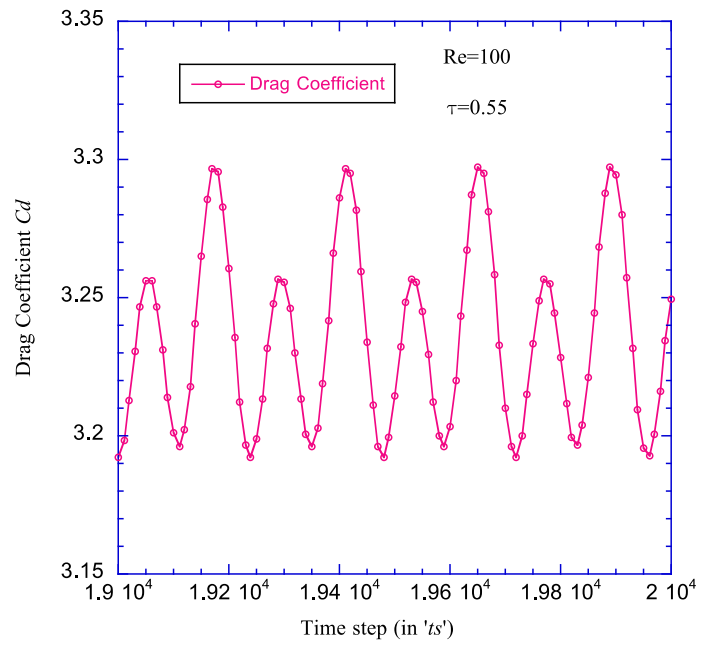
Figure 5-20: The variation of the drag coefficients for $Re = 100$.
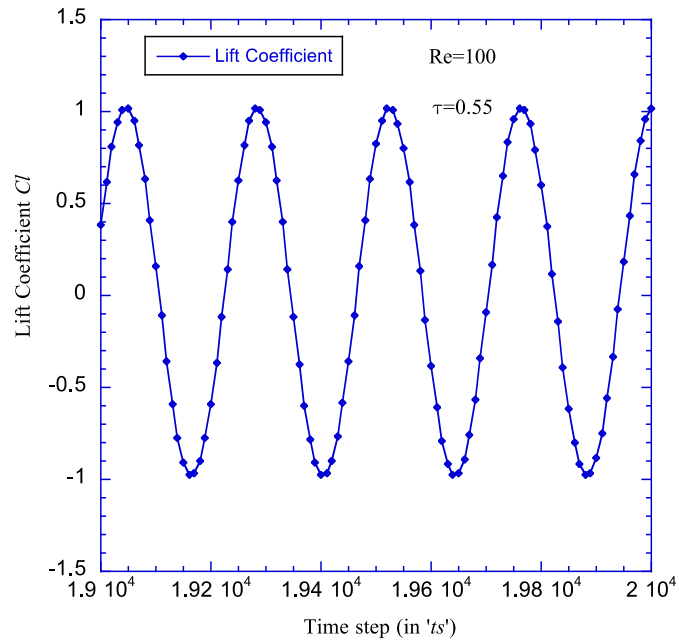
Figure 5-21: The variation of the lift coefficients for $Re = 100$.

By applying the new moving boundary condition, the simulation results in a $C_{D_{max}}$ of 3.2964, and a $C_{L_{max}}$ of 1.0124, which agree well with the results presented in the above references. From Figure 5-19, we can see the periodic fluctuations clearly with the evolution of time. For the variation in the drag coefficient shown in Figure 5-20 and coefficient shown in Figure 5-21, the period is $T \approx 202\ ts$. Thus, the Strouhal number is $St = \frac{2a}{\overline{U}T} = \approx 0.2970$, which also falls into the range $[0.2950, 0.3050]$ given in [76].

Moreover, two peaks are observed in the drag coefficient during a period, as presented in Figure 5-20, which correspond to the same two peaks observed in [64]. This observation is explained [64] as the existence of a weaker vortex and a stronger vortex alternately shed at the downstream region of the cylinder.

Based on the above simulation results of Cd, Cl and St, the instantaneous isolines of the x-direction velocity and y-direction velocity are presented in Figure 5-22 and Figure 5-23. The vortex in the downstream region of the cylinder shown in Figure 5-23 agrees well with the observation of the periodic vortex shedding.
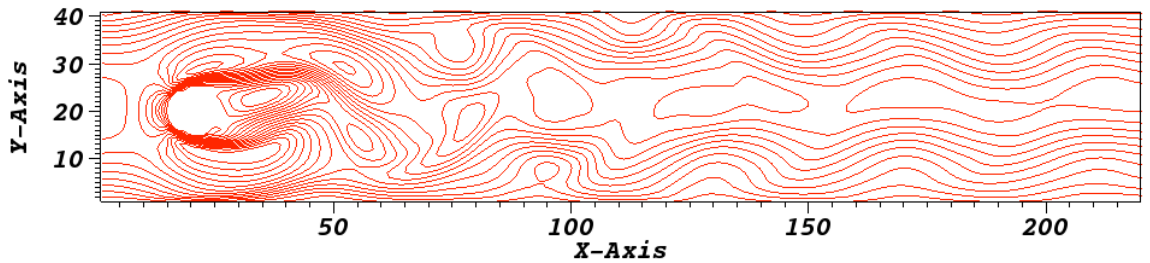
Figure 5-22: Instantaneous isolines of x-direction velocity at $Re = 100$.
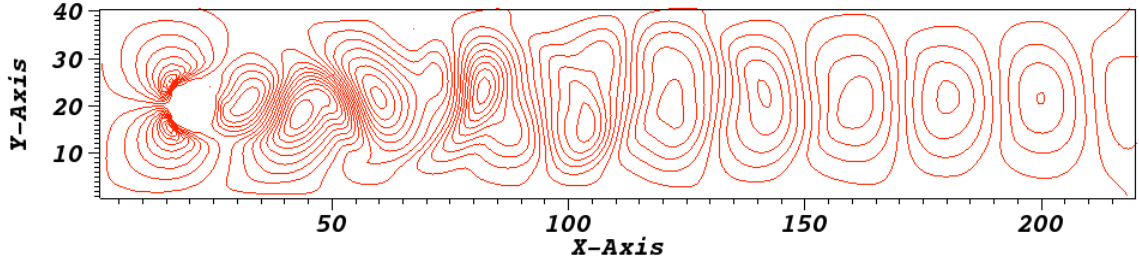
Figure 5-23: Instantaneous isolines of y-direction velocity at $Re = 100$.

In summary, by investigating the force exerted on an asymmetrically placed cylinder in the unsteady flow, the drag coefficient, lift coefficient, and Strouhal number can be calculated and compared with the existing numerical results. Excellent agreement can be seen between the results obtained with the new moving boundary condition and other boundary conditions, even with a coarser resolution. Thus, the new moving boundary condition can preserve the geometric integrity of complex surfaces, and exhibits great numerical accuracy and stability when applied to complex boundary surfaces, with a coarser resolution and a unified simpler boundary scheme, where potential computational resources can be saved for further large scale simulation.

5.5 NUMERICAL EXPERIMENTS TO VALIDATE THE GALILEAN INVARIANCE OF THE NOVEL MOVING BOUNDARY CONDITION

The Navier-Stokes equations, which are of Galilean invariance, can be recovered from the mesoscopic lattice Boltzmann equation. Thus, the Galilean invariance characteristic should be maintained for the LBM. In order to demonstrate the Galilean invariance of the new boundary scheme, a circular cylinder moving along the centerline of a channel with velocity U is simulated in different frames of reference [34]. In the first case, the position of the cylinder is fixed, with the two parallel walls moving with velocity U, such that the boundary of the cylinder is also

88

fixed, as shown in Figure 5-24. In the second case, the cylinder is moving with velocity U and the wall is fixed, such that the boundary of the cylinder is also moving, as shown in Figure 5-25. However, the relative motion between the cylinder and the wall is the same. Thus, the simulation results under the two different frames of reference can not only test the accuracy of the proposed moving boundary conditions, but also the Galilean invariance of the LBE method [85].

For the first frame of reference in Figure 5-24, a cylinder of diameter $d = 10$ lattice units is placed in the center $(x_0 = 50, y_0 = 32)$ of a channel of width $W = 64$ and length $L = 100$. The velocity of the wall is $U = -0.01$, and the particle Reynolds number is set to be 1.0 based on the definition $Re = \frac{Ud}{v}$, where the viscosity $v = \frac{(2\tau-1)}{6}$. Under the second frame of reference in Figure 5-25, the initial location of the cylinder is set to be at $(x_0 = 0, y_0 = 32)$ and the velocity of the cylinder is $U = 0.01$. Then after 5000 time steps, the location of the cylinder moves to $(x = 50, y = 32)$.
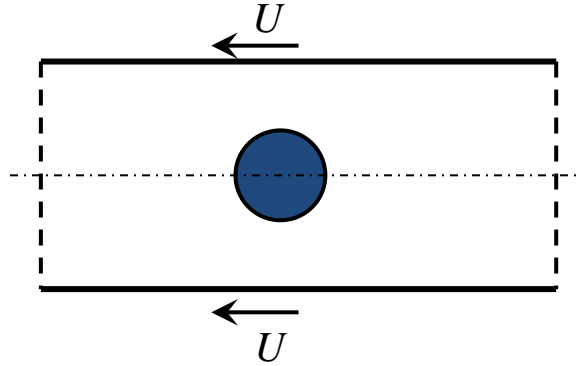
Figure 5-24: The frame of reference 1, when the location of the cylinder is fixed and the boundary walls are moving.
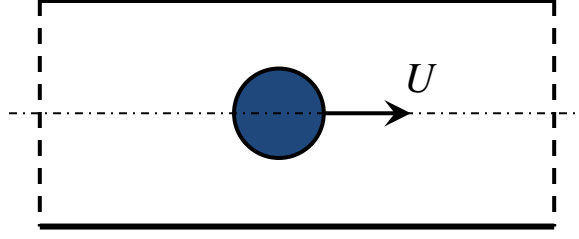
Figure 5-25: The frame of reference 2, when the cylinder is moving and boundary walls are at rest.

In order to verify the character of Galilean invariance for the new proposed boundary scheme, the normalized velocity profiles under each frame of reference after 5000 time steps are presented in Figure 5-26 and Figure 5-27. As has been done for the velocity comparison under two different frames of reference shown in [34], we also compare the results of the velocity profiles along several horizontal lines obtained by the fixed cylinder boundary (the first frame of reference) and by the moving cylinder boundary (the second frame of reference), both from applying the new proposed boundary condition. In Figure 5-26, the normalized x-component velocities along six different horizontal lines, which are $u\left(x,\frac{y}{W}=0.5\right)$, $u\left(x,\frac{y}{W}=0.422\right)$, $u\left(x,\frac{y}{W}=0.375\right)$, $u\left(x,\frac{y}{W}=0.313\right)$, $u\left(x,\frac{y}{W}=0.156\right)$, and $u\left(x,\frac{y}{W}=0.078\right)$, agree well with each other under the two different frames of reference. Similarly, the x-component velocities along the vertical line crossing the center of the cylinder, $u(x=50,y)$, under the two different frames of reference also agree perfectly with each other, as shown in Figure 5-27. Based on the agreement between the velocity profiles under the two different frames of reference, as shown in Figure 5-26 to Figure 5-27, we can see that the characteristic of Galilean invariance is maintained by applying the new moving boundary condition.
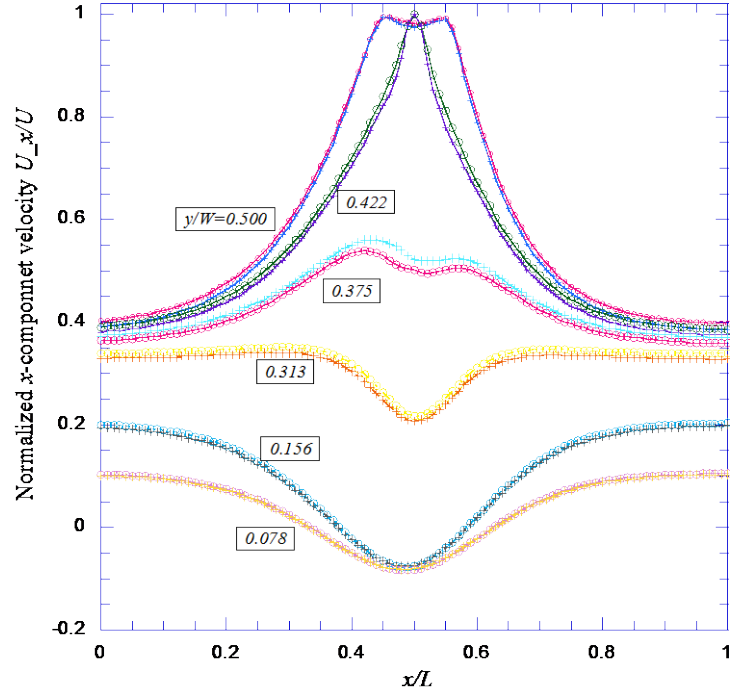
Figure 5-26: *X*-component of the velocity field along horizontal lines at $t = 5000$. The open circles and crosses are the results obtained by the fixed cylinder boundary and by the moving cylinder, respectively.

Velcoity along the cylinder center $u(x{=}50,y)$
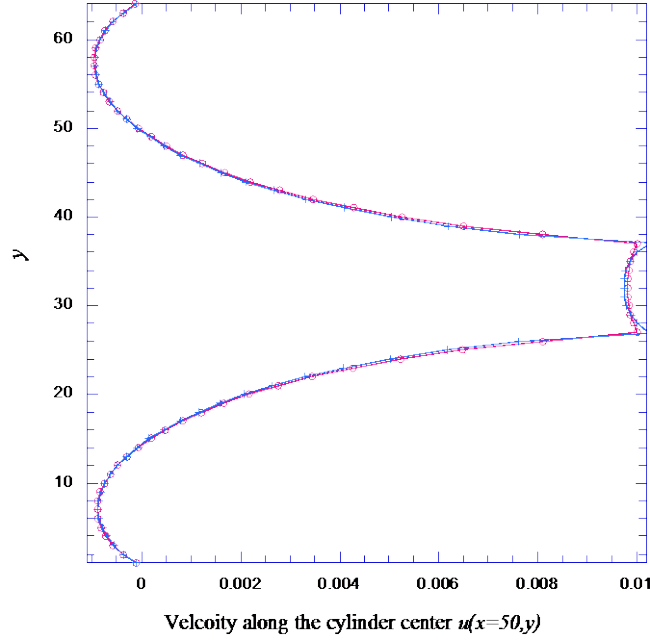
Figure 5-27: *X*-component of the velocity field along the vertical line ($u(x = 50, y)$) crossing the center of the cylinder at $t = 5000$. The open circles and crosses are the results obtained by the fixed cylinder boundary and by the moving cylinder boundary, respectively.

To assess the accuracy of the new boundary condition for moving boundaries, the relative L$_2$-norm error as defined by $E_2 = \dfrac{\left\{\int_0^L [u_{Ref1} - u_{Ref2}]^2\, dx\right\}^{1/2}}{\left\{\int_0^L u_{Ref1}^2\, dx\right\}^{1/2}}$ along the six different horizontal lines is presented in Figure 5-28, where the u_{Ref1} denotes the velocity obtained under the first frame of reference and u_{Ref2} denotes the velocity obtained under the second frame of reference. For comparison, Ladd's moving boundary condition as introduced in Section 3.4 is applied for the same numerical experiments.

The relative L$_2$-norm errors along the six horizontal lines under the two different frames of reference for both Ladd's moving boundary condition and the new proposed boundary

92

condition are shown in Figure 5-28. From Figure 5-28, the relative L_2-norm error shows that the difference between the two frames of reference is quite small and the relative motion is the same under these two different frames of reference. Moreover, the numerical errors of the new proposed boundary scheme are smaller than Ladd's moving boundary condition, and thus the Galilean invariance character of the new boundary condition can be better maintained. One reason for the improvement of the characteristic of Galilean invariance can be also explained by the stronger capability to locate the moving boundaries for the new moving boundary condition.
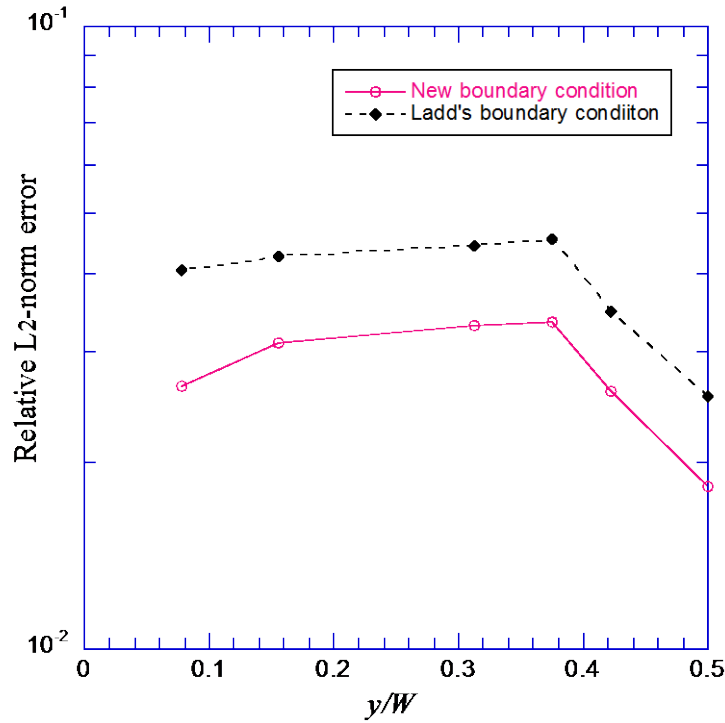
Figure 5-28: Relative L_2-norm error along the six different horizontal lines, which are $y/W = 0.5$, $y/W = 0.422$, $y/W = 0.375$, $y/W = 0.313$, $y/W = 0.156$, and $y/W = 0.078$. The open circles and the solid squares are the errors obtained by the new proposed boundary condition and Ladd's boundary condition, respectively.

In this chapter, a rigorous mathematical derivation of the new moving boundary condition was introduced in detail, and numerical experiments were carried out by applying the new moving boundary condition for flat moving surfaces, static complex surfaces, and moving complex surfaces. Improvements in both numerical accuracy and numerical stability can be observed by applying the new moving boundary condition for flat surfaces in the numerical tests. A strong capacity to preserve the geometric integrity of complex surfaces also can be proven by an investigation of the normalized velocity profiles in the upstream and downstream regions for static cylinders of different radii. Furthermore, from the benchmark study on the force exerted on an asymmetrically placed cylinder in an unsteady flow, great ability to preserve the geometric integrity can also be seen to reduce the necessary mesh resolution. The maintained and improved characteristic of Galilean invariance of the new moving boundary condition is confirmed by probing the velocity profiles under two different frames of reference. Based on all of these numerical experiments for modelling a particle-fluid system in this chapter, it can be concluded that the new moving boundary condition is a universal improvement over the existing boundary conditions used in the field of LBM.

6.0   CONCLUSIONS AND FUTURE WORK

6.1   MAJOR CONTRIBUTIONS

In this dissertation, several original contributions have been made for the investigation of particle-fluid systems by applying the LBM approach. The following is a summary of the accomplishments of this work.

6.1.1   Development of rigorous unit transformations between a physical system and the lattice Boltzmann system

For the numerical modeling process, the values of certain parameters are very important for any meaningful simulation results. In most previous work, only the values of simulation parameters, such as relaxation parameters τ, dimensionless lattice velocities u, etc., are given, without any explanations of the physical meanings or the relationships to the real physical world. In this work, rigorous unit transformations between the real physical world system and the lattice Boltzmann system are given. The transformation between these two systems are built on the equality of the non-dimensional numbers, such as the Reynolds number Re, and Mach number Ma. Based on this, the values of the parameters for the LB systems can be obtained by simple calculations, and thus, the physical meanings of the parameters chosen for the LBM numerical tests are clear and

reasonable. The transformation table, as shown in Table 2-1, provides a reference for choosing parameters for the LBM numerical experiments, for both this work and future researchers, so that meaningful simulation results can be obtained and explained.

6.1.2   Comprehensive investigation of the boundary conditions for particle-fluid systems

The most popular boundary conditions for modeling particle-fluid systems with the LBM are introduced and investigated comprehensively, such as the bounce-back boundary condition, the bounce-back on the link boundary condition, the interpolation based boundary condition, the FH boundary condition, and Ladd's boundary condition. Each of the above boundary conditions is explained in detail, and a thorough analysis of the advantages and disadvantages of each boundary condition is given.

In order to further investigate existing boundary conditions for particle-fluid systems, a simple flow case, Couette flow, was first developed. The results from the LBM simulation were shown to be in agreement with the analytical solution. Next, we further investigated the velocity profiles in the upstream and downstream regions of a cylinder at rest in a channel to check the ability to capture a complex boundary by applying a given boundary condition. Following that investigation, the force exerted on an asymmetrically placed cylinder was evaluated. The momentum exchange method, as introduced in Section 3.5, was used to calculate the drag coefficient and lift coefficient obtained by the LBM and compare them to other CFD approaches. Finally, simulations of the movement of a cylinder in Couette flow and Poiseuille flow were carried out, and the trajectories of the cylinder under different Reynolds numbers plotted and explained.

6.1.3 Development of a new moving boundary condition based on the Chapman-Enskog expansion

In the investigation of previous boundary conditions and the development of a particle-fluid system for the LBM, it was found there were important deficiencies in the existing methodologies. To that end, we proposed a moving boundary condition based on a rigorous mathematical derivation from the Chapman-Enskog expansion, which is the theoretical foundation for the recovery from the lattice Boltzmann equation to the Navier-Stokes equations. The process of constructing the new moving boundary condition is explained in detail and numerical experiments are carried out by applying the new moving boundary condition for flat moving surfaces, static complex surfaces, and moving complex surfaces. Improvements in numerical accuracy and numerical stability can be observed by applying the new moving boundary condition for flat surfaces. Additionally, a strong capability to preserve the geometric integrity of complex surfaces can be proven by investigation of the normalized velocity profiles in the upstream and downstream regions of a static cylinder, and by the force evaluation on an asymmetrically placed cylinder by reduced mesh resolution. The new boundary condition was also shown to maintain and improve the characteristic of Galilean invariance by probing the velocity profiles under two different frames of reference. Moreover, the new moving boundary condition has a simpler scheme, which can be implemented without consideration of instability issues. Finally, the way to build the new moving boundary condition provides a novel concept to construct the boundary condition for the LBM without the limitation of being based on the information from the already existing lattice nodes.

In conclusion, then, the particle-fluid boundary interaction of particulate suspension systems is successfully modeled by the LBM approach with appropriate boundary schemes. The

new moving boundary condition, based on a more rigorous theoretical foundation, highly improves the numerical accuracy for flat wall boundaries, preserves numerical accuracy and stability with a coarser mesh resolution for complex boundaries, exhibits a stronger capability to preserve geometric integrity, and maintains a better Galilean invariance characteristic for modeling such particulate suspension systems.

6.2   FUTURE WORK

The field of LBM fluid simulation is very versatile and promising, with many potential advantages over conventional CFD approaches. As a result, there are a number of exciting potential avenues for its future development. A few of the areas specifically related to the work presented here are listed below.

6.2.1   Multiple-particle particulate suspension systems

The new boundary condition proposed in this work is validated through numerical experiments mainly focused on a single particle fluid system. For most of particulate suspension systems in real applications, multiple particles will be involved for the numerical modeling, where the interaction forces, such as particle-particle and particle-wall, need to be considered in addition to the particle-fluid interaction. For most of the previous studies on multi-particle systems, the simple bounce-back [86] or bounce-back on the link [87] boundary condition is applied for the numerical tests; thus, further applications of the new boundary condition to multi-particle systems need to be investigated and validated. Additionally, for multi-phase microchannel flow

[88], especially for the most interesting Taylor slug flows, the large area of interfacial interaction between the fluid is of the most interest. The formation of Taylor slug flow has already been successfully simulated by applying the LBM [89], and with a more accurate boundary condition for the multi-phase microchannel flow, the formation mechanism can be further investigated.

Moreover, when dealing with the inside lattice nodes of the boundary surface in this work, in order to keep the computational domain consistent, the lattice nodes inside and outside of the boundary surface are treated as fluid nodes, which is known as Ladd's shell model. Therefore, the density ratio in the numerical experiments is chosen based on the constraint $\frac{\rho_s}{\rho_f} > 1 + \frac{10}{r}$, which is used as a stability criterion for the shell model, and then this constraint limits the expansion application of Ladd's shell model [72]. Therefore, research on the effect of treating the lattice nodes inside the boundary surfaces as fluid needs to be furthered and the limitation of the density ratio improved.

6.2.2   Parallel computation

One of the important features of the LBM is that it is very suitable for parallel computation. The collision process is exactly local and the streaming process is almost local, and only needs information from the neighboring lattice nodes. Parallel computation with the LBM has been successfully applied to simulate multi-particle particulate suspension systems [87, 90]. In the process of constructing the new moving boundary condition, only interpolation schemes based on already known information from the neighboring lattice nodes need to be implemented, which will not affect the applicability of parallel computation. Due to the stronger capability of the new moving boundary condition to capture the solid boundary surfaces, the resolution of the mesh

can be reduced for the simulation processes. Therefore, parallel computation is also suitable for investigation of particulate suspension systems by applying our new moving boundary condition, and a great reduction in computational time and resources can be expected.

BIBLIOGRAPHY

1. Dünweg, B. and A.J.C. Ladd, *Lattice Boltzmann Simulations of Soft Matter Systems*. 2008, Springer Berlin Heidelberg. p. 1-78.

2. Zhang, J., *Lattice Boltzmann method for microfluidics: models and applications.* Microfluidics and Nanofluidics, 2011. **10**(1): p. 1-28.

3. Ahuja, A.S., *Augmentation of heat transport in laminar flow of polystyrene suspensions. I. Experiments and results.* Journal of Applied Physics, 1975. **46**(8): p. 3408-3416.

4. Choi, S.U.S. and J.A. Eastman, *Enhancing thermal conductivity of fluids with nanoparticles*. 1995. Medium: ED; Size: 8 p.

5. Lee, S., et al., *Measuring thermal conductivity of fluids containing oxide nanoparticles.* Journal Name: Journal of Heat Transfer; Journal Volume: 121; Journal Issue: 2; Other Information: PBD: May 1999, 1999: p. Medium: X; Size: pp. 280-289.

6. Das, S.K., et al., *Temperature Dependence of Thermal Conductivity Enhancement for Nanofluids.* Journal of Heat Transfer, 2003. **125**(4): p. 567.

7. Lee, B.J., et al., *Radiative heat transfer analysis in plasmonic nanofluids for direct solar thermal absorption.* Journal of Solar Energy Engineering, 2012. **134**(2): p. 021009.

8. Keblinski, P., et al., *Mechanisms of heat flow in suspensions of nano-sized particles (nanofluids).* International Journal of Heat and Mass Transfer, 2002. **45**(4): p. 855-863.

9. Bird, G.A., *Direct Simulation and the Boltzmann Equation.* Physics of Fluids (1958-1988), 1970. **13**(11): p. 2676-2681.

10. Soddemann, T., B. Dünweg, and K. Kremer, *Dissipative particle dynamics: A useful thermostat for equilibrium and nonequilibrium molecular dynamics simulations.* physical review e, 2003. **68**(4): p. 046702.

11. Hoogerbrugge, P. and J. Koelman, *Simulating microscopic hydrodynamic phenomena with dissipative particle dynamics.* EPL (Europhysics Letters), 1992. **19**(3): p. 155.

12.   Yuan, P., *Thermal lattice Boltzmann two-phase flow model for fluid dynamics*, 2006, University of Pittsburgh.

13.   Ikeda, M., *A novel multiple-phase, multiple-component, thermal lattice Boltzmann model*, 2013, UNIVERSITY OF PITTSBURGH.

14.   U. Frisch, D.d.H., B. Hasslacher, P. Lallemand, Y. Pomeau, and J.-P. Rivet, *Lattice gas hydrodynamics in two and three dimensions.* Complex systems 1987. **1**: p. 649-707.

15.   Chen, S. and G.D. Doolen, *Lattice Boltzmann method for fluid flows.* Annual review of fluid mechanics, 1998. **30**(1): p. 329-364.

16.   Succi, S., *The Lattice Boltzmann Equation: For Fluid Dynamics and Beyond.* 2001: Oxford University Press, Incorporated.

17.   Orszag, S.A. and V. Yakhot, *Reynolds Number Scaling of Cellular-Automaton Hydrodynamics.* Physical Review Letters, 1986. **56**(16): p. 1691-1693.

18.   Succi, S., P. Santangelo, and R. Benzi, *High-Resolution Lattice-Gas Simulation of Two-Dimensional Turbulence.* Physical Review Letters, 1988. **60**(26): p. 2738-2740.

19.   McNamara, G.R. and G. Zanetti, *Use of the Boltzmann Equation to Simulate Lattice-Gas Automata.* Physical Review Letters, 1988. **61**(20): p. 2332-2335.

20.   Jafari, S., R. Yamamoto, and M. Rahnama, *Lattice-Boltzmann method combined with smoothed-profile method for particulate suspensions.* physical review e, 2011. **83**(2): p. 026702.

21.   Huang, H., et al., *Rotation of spheroidal particles in Couette flows.* Journal of Fluid Mechanics, 2012. **692**: p. 369-394.

22.   Qi, D. and L.-S. Luo, *Rotational and orientational behaviour of three-dimensional spheroidal particles in Couette flows.* Journal of Fluid Mechanics, 2003. **477**.

23.   Behrend, O., *Solid-fluid boundaries in particle suspension simulations via the lattice Boltzmann method.* physical review e, 1995. **52**(1): p. 1164-1175.

24.   Xia, Z., et al., *Flow patterns in the sedimentation of an elliptical particle.* Journal of Fluid Mechanics, 2009. **625**: p. 249.

25.   Jäsberg, A., et al., *Hydrodynamical forces acting on particles in a two-dimensional flow near a solid wall.* Computer Physics Communications, 2000. **129**(1–3): p. 196-206.

26.   Cornubert, R., D. d'Humières, and D. Levermore, *A Knudsen layer theory for lattice gases.* Physica D: Nonlinear Phenomena, 1991. **47**(1–2): p. 241-259.

27.   Ginzbourg, I. and P.M. Adler, *Boundary flow condition analysis for the three-dimensional lattice Boltzmann model.* J. Phys. II France, 1994. **4**(2): p. 191-214.

28.   Ladd, A.J.C., *Numerical simulations of particulate suspensions via a discretized Boltzmann equation, Part 1. Theoretical foundation.* Journal of Fluid Mechanics, 1994. **271**: p. 285.

29.   Ladd, A.J.C., *Numerical simulations of particulate suspensions via a discretized Boltzmann equation. Part 2. Numerical results.* Journal of Fluid Mechanics, 1994. **271**: p. 311-339.

30.   A. J. C. Ladd, a.R.V., *Lattice-Boltzmann simulations of particlefluid suspensions.* Journal of statistical physics, 2001. **104**.

31.   Filippova, O. and D. Hänel, *Grid Refinement for Lattice-BGK Models.* Journal of Computational Physics, 1998. **147**(1): p. 219-228.

32.   Mei, R., L.-S. Luo, and W. Shyy, *An Accurate Curved Boundary Treatment in the Lattice Boltzmann Method.* Journal of Computational Physics, 1999. **155**(2): p. 307-330.

33.   Mei, R., et al., *Lattice Boltzmann Method for 3-D Flows with Curved Boundary.* Journal of Computational Physics, 2000. **161**(2): p. 680-699.

34.   Aidun, C.K., Y. Lu, and E.-J. Ding, *Direct analysis of particulate suspensions with inertia using the discrete Boltzmann equation.* Journal of Fluid Mechanics, 1998. **373**(1): p. 287-311.

35.   Aidun, C.K. and Y. Lu, *Lattice Boltzmann simulation of solid particles suspended in fluid.* Journal of statistical physics, 1995. **81**(1-2): p. 49-61.

36.   Grad, H., *Note on the N-dimensional Hermite polynomials.* Commun. Pure Appl. Maths, 1949. **9**: p. 331.

37.   Grad, H., *On the Kinetic theory of rarefied gases.* Commun. Pure Appl. Maths, 1949. **9**: p. 331.

38.   Chapman, S. and T.G. Cowling, *The mathematical theory of non-uniform gases: an account of the kinetic theory of viscosity, thermal conduction and diffusion in gases*. 1991: Cambridge university press.

39.   Latt, J., *Hydrodynamic limit of lattice Boltzmann equations.* 2007.

40.   Schiller, U.D., *Thermal fluctuations and boundary conditions in the lattice Boltzmann method*, 2008, Thèse de doctorat, Johannes Gutenberg University Mainz.

41.   Golse, F., *The Boltzmann equation and its hydrodunamic limits.* Handbook of differential equations, Evolutionary equations, 2005. **2**.

42.   HUANG, K., *STATISTICAL MECHANICS ssconn EDITION.* 1987.

43.	S. Succi, L.V.K., and H. Chen, *Role of the H theorem in lattice Boltzmann hydrodynamic simulations.* Reviews of Modern physics, 2002. **74**: p. 1203.

44.	Higuera, F. and J. Jimenez, *Boltzmann approach to lattice gas simulations.* EPL (Europhysics Letters), 1989. **9**(7): p. 663.

45.	Higuera, F., S. Succi, and R. Benzi, *Lattice gas dynamics with enhanced collisions.* EPL (Europhysics Letters), 1989. **9**(4): p. 345.

46.	Bhatnagar, P.L., E.P. Gross, and M. Krook, *A model for collision processes in gases. I. Small amplitude processes in charged and neutral one-component systems.* Physical review, 1954. **94**(3): p. 511.

47.	He, X. and L.-S. Luo, *Theory of the lattice Boltzmann method: From the Boltzmann equation to the lattice Boltzmann equation.* Physical Review E, 1997. **56**(6): p. 6811-6817.

48.	Y. H. Qian, D.d.H., and P. Lallemand, *Lattice BGK models for Navier-Stokes equation.* Europhysics Letters, 1992. **16**: p. 479-484.

49.	Abe, T., *Derivation of the Lattice Boltzmann Method by Means of the Discrete Ordinate Method for the Boltzmann Equation.* Journal of Computational Physics, 1997. **131**(1): p. 241-246.

50.	Aidun, C.K. and J.R. Clausen, *Lattice-Boltzmann method for complex flows.* Annual Review of Fluid Mechanics, 2010. **42**: p. 439-472.

51.	He, X. and L.-S. Luo, *Lattice Boltzmann model for the incompressible Navier–Stokes equation.* Journal of Statistical Physics, 1997. **88**(3-4): p. 927-944.

52.	He, X., et al., *Analytic solutions of simple flows and analysis of nonslip boundary conditions for the lattice Boltzmann BGK model.* Journal of Statistical Physics, 1997. **87**(1-2): p. 115-136.

53.	Ziegler, D., *Boundary conditions for lattice Boltzmann simulations.* Journal of Statistical Physics, 1993. **71**(5-6): p. 1171-1177.

54.	Zou, Q. and X. He, *On pressure and velocity boundary conditions for the lattice Boltzmann BGK model.* Physics of Fluids, 1997. **9**: p. 1591.

55.	Inamuro, T., M. Yoshino, and F. Ogino, *A non-slip boundary condition for lattice Boltzmann simulations.* arXiv preprint comp-gas/9508002, 1995.

56.	Bouzidi, M.h., M. Firdaouss, and P. Lallemand, *Momentum transfer of a Boltzmann-lattice fluid with boundaries.* Physics of Fluids, 2001. **13**: p. 3452.

57.	Luo, L.-S., *Analytic solutions of linearized lattice Boltzmann equation for simple flows.* Journal of statistical physics, 1997. **88**(3-4): p. 913-926.

58. Noble, D.R., et al., *A consistent hydrodynamic boundary condition for the lattice Boltzmann method.* Physics of Fluids, 1995. **7**: p. 203.

59. Chen, S., D. Martinez, and R. Mei, *On boundary conditions in lattice Boltzmann methods.* Physics of fluids, 1996. **8**: p. 2527.

60. Ginzbourg, I. and D. d'Humières, *Local second-order boundary methods for lattice Boltzmann models.* Journal of statistical physics, 1996. **84**(5-6): p. 927-971.

61. Mei, R. and W. Shyy, *On the finite difference-based lattice Boltzmann method in curvilinear coordinates.* Journal of Computational Physics, 1998. **143**(2): p. 426-448.

62. He, X. and G. Doolen, *Lattice Boltzmann method on curvilinear coordinates system: flow around a circular cylinder.* Journal of Computational Physics, 1997. **134**(2): p. 306-315.

63. Filippova, O. and D. Hänel, *Lattice-Boltzmann simulation of gas-particle flow in filters.* Computers & Fluids, 1997. **26**(7): p. 697-712.

64. Mei, R., et al., *Force evaluation in the lattice Boltzmann method involving curved geometry.* Physical Review E, 2002. **65**(4): p. 041203.

65. Lorenz, E., A. Caiazzo, and A.G. Hoekstra, *Corrected momentum exchange method for lattice Boltzmann simulations of suspension flow.* Physical Review E, 2009. **79**(3): p. 036705.

66. Caiazzo, A. and M. Junk, *Boundary forces in lattice Boltzmann: Analysis of momentum exchange algorithm.* Computers & Mathematics with Applications, 2008. **55**(7): p. 1415-1423.

67. Feng, Z.-G. and E.E. Michaelides, *Hydrodynamic force on spheres in cylindrical and prismatic enclosures.* International Journal of Multiphase Flow, 2002. **28**(3): p. 479-496.

68. Feng, Z.-G. and E.E. Michaelides, *The immersed boundary-lattice Boltzmann method for solving fluid–particles interaction problems.* Journal of Computational Physics, 2004. **195**(2): p. 602-628.

69. Wu, J. and C. Shu, *Particulate flow simulation via a boundary condition-enforced immersed boundary-lattice Boltzmann scheme.* Communications in Computational Physics, 2010. **7**(4): p. 793.

70. Han, Y. and P.A. Cundall, *Resolution sensitivity of momentum‐exchange and immersed boundary methods for solid‐fluid interaction in the lattice Boltzmann method.* International Journal for Numerical Methods in Fluids, 2011. **67**(3): p. 314-327.

71. Peskin, C.S., *Numerical analysis of blood flow in the heart.* Journal of Computational Physics, 1977. **25**(3): p. 220-252.

72.   Chen, Y., et al., *Momentum-exchange method in lattice Boltzmann simulations of particle-fluid interactions.* Physical Review E, 2013. **88**(1): p. 013303.

73.   He, X., L.-S. Luo, and M. Dembo, *Some progress in lattice Boltzmann method. Part I. Nonuniform mesh grids.* Journal of Computational Physics, 1996. **129**(2): p. 357-363.

74.   Ding, E.-J. and C.K. Aidun, *Extension of the lattice-Boltzmann method for direct simulation of suspended particles near contact.* Journal of statistical physics, 2003. **112**(3-4): p. 685-708.

75.   Munson, B.R., D.F. Young, and T.H. Okiishi, *Fundamentals of fluid mechanics.* 4th ed. 2002: Wiley.

76.   Schäfer, M., et al., *Benchmark computations of laminar flow around a cylinder.* Notes on numerical fluid mechanics, 1996. **52**: p. 547-566.

77.   Niu, X., et al., *A momentum exchange-based immersed boundary-lattice Boltzmann method for simulating incompressible viscous flows.* Physics Letters A, 2006. **354**(3): p. 173-182.

78.   Feng, J., H. Hu, and D. Joseph, *Direct simulation of initial value problems for the motion of solid bodies in a Newtonian fluid. Part 2. Couette and Poiseuille flows.* Journal of fluid mechanics, 1994. **277**(271): p. 271-301.

79.   Feng, J., H.H. Hu, and D.D. Joseph, *Direct simulation of initial value problems for the motion of solid bodies in a Newtonian fluid. Part 1. Sedimentation.* Journal of Fluid Mechanics, 1994. **261**: p. 95-134.

80.   OHTSUKI, S. and T. MATSUOKA, *Numerical simulation of solid particle behaviors in fluid flow by using a numerical method coupling technique.* International Journal of the JCRM, 2009. **4**(2): p. 61-67.

81.   Wen, B., et al., *Lattice-type-dependent momentum-exchange method for moving boundaries.* Physical Review E, 2012. **85**(1): p. 016704.

82.   Luo, L.-S., *Unified theory of lattice Boltzmann models for nonideal gases.* Physical review letters, 1998. **81**(8): p. 1618-1621.

83.   CHEN, D.-J., K.-H. LIN, and C.-A. LIN, *IMMERSED BOUNDARY METHOD BASED LATTICE BOLTZMANN METHOD TO SIMULATE 2D AND 3D COMPLEX GEOMETRY FLOWS.* International Journal of Modern Physics C, 2007. **18**(04): p. 585-594.

84.   Chang, C., C.-H. Liu, and C.-A. Lin, *Boundary conditions for lattice Boltzmann simulations with complex geometry flows.* Computers & Mathematics with Applications, 2009. **58**(5): p. 940-949.

85.   Lallemand, P. and L.-S. Luo, *Lattice Boltzmann method for moving boundaries.* Journal of Computational Physics, 2003. **184**(2): p. 406-421.

86.   Wang, L., et al., *Lattice Boltzmann based discrete simulation for gas–solid fluidization.* Chemical Engineering Science, 2013. **101**: p. 228-239.

87.   Stratford, K. and I. Pagonabarraga, *Parallel simulation of particle suspensions with the lattice Boltzmann method.* Computers & Mathematics with Applications, 2008. **55**(7): p. 1585-1593.

88.   Günther, A. and M.T. Kreutzer, *Multiphase Flow*, in *Micro Process Engineering*. 2009, Wiley-VCH Verlag GmbH & Co. KGaA. p. 1-40.

89.   Yu, Z., O. Hemminger, and L.-S. Fan, *Experiment and lattice Boltzmann simulation of two-phase gas–liquid flows in microchannels.* Chemical Engineering Science, 2007. **62**(24): p. 7172-7183.

90.   Xiong, Q., E. Madadi-Kandjani, and G. Lorenzini, *A LBM–DEM solver for fast discrete particle simulation of particle–fluid flows.* Continuum Mechanics and Thermodynamics, 2014: p. 1-11.